THE RELATIONSHIP BETWEEN THE MORPHOLOGY AND KINEMATICS OF GALAXIES AND ITS DEPENDENCE ON DARK MATTER HALO STRUCTURE IN SIMULATED GALAXIES

Adrien Christian René THOB

A thesis submitted in partial fulfilment of the requirements of

Liverpool John Moores University

for the degree of

Doctor of Philosophy.

26 April 2019

To my grand-parents, René Roumeaux, Christian Thob, Yvette Roumeaux (née Bajaud) and Anne-Marie Thob (née Léglise).

Abstract

Galaxies are among nature's most majestic and diverse structures. They can play host to as few as several thousands of stars, or as many as hundreds of billions. They exhibit a broad range of shapes, sizes, colours, and they can inhabit vastly differing cosmic environments. The physics of galaxy formation is highly non-linear and involves a variety of physical mechanisms, precluding the development of entirely analytic descriptions, thus requiring that theoretical ideas concerning the origin of this diversity are tested via the confrontation of numerical models (or "simulations") with observational measurements. The EAGLE project (which stands for Evolution and Assembly of GaLaxies and their Environments) is a state-of-the-art suite of such cosmological hydrodynamical simulations of the Universe. EAGLE is unique in that the ill-understood efficiencies of feedback mechanisms implemented in the model were calibrated to ensure that the observed stellar masses and sizes of present-day galaxies were reproduced. We investigate the connection between the morphology and internal kinematics of the stellar component of central galaxies with mass $M_\star > 10^{9.5} \ \mathrm{M_\odot}$ in the EAGLE simulations. We compare several kinematic diagnostics commonly used to describe simulated galaxies, and find good consistency between them. We model the structure of galaxies as ellipsoids and quantify their morphology via the ratios of their principal axes. We show that the differentiation of blue star-forming and red quiescent galaxies using morphological diagnostics can be achieved with similar efficacy to the use of kinematical diagnostics, but only if one is able to measure both the flattening and the triaxiality of the galaxy. Flattened oblate galaxies exhibit greater rotational support than their spheroidal counterparts, but there is significant scatter in the relationship between morphological and kinematical diagnostics, such that kinematically-similar

galaxies can exhibit a broad range of morphologies. The scatter in the relationship between the flattening and the ratio of the rotation and dispersion velocities (v/σ) correlates strongly with the anisotropy of the stellar velocity dispersion: at fixed v/σ, flatter galaxies exhibit greater dispersion in the plane defined by the intermediate and major axes than along the minor axis, indicating that the morphology of simulated galaxies is influenced significantly by the structure of their velocity dispersion. The simulations reveal that this anisotropy correlates with the intrinsic morphology of the galaxy's inner dark matter halo, i.e. the halo's morphology that emerges in the absence of dissipative baryonic physics. This implies the existence of a causal relationship between the morphologies of galaxies and that of their host dark matter haloes. Using these tools, we also investigate the morphology and kinematics of central galaxies with mass $M_\star > 10^{9.5}$ M$_\odot$ and their globular cluster (GC) populations in the EAGLE spin-off project E-MOSAICS that incorporates the MOSAICS model of stellar cluster formation and evolution. We find that metal-poor and metal-rich GC populations (split by a threshold at $[\mathrm{Fe/H}] = -1$) exhibit differing characteristic morpho-kinematic properties. The former are significantly more elliptical and dispersion-supported than the latter. In detail, the relations connecting the kinematic properties of the populations with those of their host galaxy exhibit good agreement with available observations, with the velocity dispersions of both metal-poor and metal-rich GC populations correlating positively with that of the host galaxy. The rotational velocity of the metal-rich globular cluster population also correlates positively with that of the host galaxy. The relationship between the morpho-kinematics of the metal-rich globular clusters and the host galaxy's field stars exhibits a scatter that is sensitive to the relative ages of the two populations: for fixed globular cluster kinematics, the field star population is more disky/rotation-supported if they are younger. We confirm that the connection between the morpho-kinematics of galaxies and their velocity dispersion anisotropy revealed in EAGLE is also exhibit in the higher-resolution E-MOSAICS simulation. However, the same behaviour is not seen in the metal-rich globular clusters, which we speculate is a consequence of them not representing a self-gravitating system.

ADRIEN CHRISTIAN RENÉ THOB   JULY 9, 2019

Contents

Bibliography   **123**

Figures

Declaration

The work presented in this thesis was carried out at the Astrophysics Research Institute, Liverpool John Moores University. Unless otherwise stated, it is the original work of the author.

While registered as a candidate for the degree of Doctor of Philosophy, for which submission is now made, the author has not been registered as a candidate for any other award. This thesis has not been submitted in whole, or in part, for any other degree.

Adrien Christian René THOB

Astrophysics Research Institute

Liverpool John Moores University

IC2, Liverpool Science Park

146 Brownlow Hill

Liverpool

L3 5RF

UK

JULY 9, 2019

Credits

All figures were produced by the author, except the following:

- Figure 1.1: Adapted by the author from online material by M. Whittle

- Figure 1.2: Adapted by the author from Figure 4 of Schawinski et al. (2014)

- Figure 1.3: Produced by Wechsler and Tinker (2018, Figure 2) from data compiled by Behroozi et al. (2018)

- Figure 1.4: Adapted by the author from Wikimedia Commons content

- Figure 2.1: Taken from a movie produced by the Lynx X-Ray Observatory team for which the author provided the original simulation renderings

All the analysis which this work is based on has been conducted and illustrated using the language `Python2.7` and its packages `NumPy`, `Scipy`, `Matplotlib`, `H5py`, `scikit-learn` and `Py-SPHViewer`.

ADRIEN CHRISTIAN RENÉ THOB   JULY 9, 2019

Publications

Elements of the work presented in this thesis have appeared in the following refereed articles:

- *"The relationship between the morphology and kinematics of galaxies and its dependence on dark matter halo structure in EAGLE"* - **Thob, Adrien C. R.**; Crain, Robert A.; McCarthy, Ian G.; Schaller, Matthieu; Lagos, Claudia D. P.; Schaye, Joop; Talens, Geert Jan J.; James, Philip A.; Theuns, Tom; Bower, Richard G.; - published in the Monthly Notices of the Royal Astronomical Society, Volume 485, Issue 1, in May 2019

- *"The relation between galaxy morphology and colour in the EAGLE simulation"* - Correa, Camila A.; Schaye, Joop; Clauwens, Bart; Bower, Richard G.; Crain, Robert A.; Schaller, Matthieu; Theuns, Tom; **Thob, Adrien C. R.**; - published in the Monthly Notices of the Royal Astronomical Society: Letters, Volume 472, Issue 1, in November 2017

Acknowledgements

people. Without their friendship and encouragement, this thesis would not have been possible:

- Special thanks to my "Casa del pueblo" houseshare and affiliated friends:

    – To my eternal housemate and soul brother Michele Scotto Di Mase without whom my life in Liverpool would have probably sucked

    – To Marc Izaguerra Serano for all the crazy partying which he knows how to do best

    – To Ryan Joe Martindale for always finding a way to make me jam when I'm too lazy

    – To Lorenzo Ramos-Mucci for he-knows-what

    – To all the board game crew, Andrea, Roberto, Angie, Eleonora, ...

    – To Tea, Giulia, Barbara, Fra, Ifi, Emmanuel, ...

- Special thanks to many Liverpool-based French friends:

    – To Thibaut Hebinger who introduced me to Liverpool's life

    – To Nawal Belkalem and Héloise Debelle, who would disintegrate me if I don't mention them together

    – To Gaelle Legrand for being my best French pal through Liverpool's music life

    – To Jacques, Antho, Hugo, Victor, Thomas, Clem, Amélie, Anaëlle, Céleste, Delphine, ...

- Special thanks to the phenomenal Galactic Funk Militia for taking me on their mothership and giving me the funk throughout this journey, namely Mook, Andy, Max, Malou, Nick, T-Sesh, Liam, Lel, Amber, Graham

- Special thanks to the Liverpool music community as a whole, Sam, Pablo, Alex, Becky, Luke, Amy, Ritchie, Juliana, the Frederiks jazz nights, ...

- Special thanks to the Liverpool Couchsurfing community, Liz, Kev, Martin, Eddy, Esteban, Filip, Alan, Clay, Cristina, Elliot, Charlie, Karolina, Anna, Emre, Yuv, ...

- Special thanks to the International Student Society of LJMU, Summer, Julia, Adi, Nez, Fleur, ...

- Special thanks to Inco and Marcel for their board game evenings and afternoons

- And a last special thanks to some of my fellows from my former engineering school Télecom Bretagne for visiting Liverpool, Marvin, Tom, Gosselin, Sarah, Flo16 and Loïc

While I spent most of my time in Liverpool, being French also made me come back to my home to regroup with family and friends. Among the latter, many were always present and thoughtful towards my well-being. I would like to thank for that in no particular order:

- Guillaume, Céline, Guigui, Arnaud, Vincent, Alex for the Normandie New Year's eve trips and occasional afternoons spent together

- some of my fellows from Télecom Bretagne, namely Guénolé, Loris, Chollet, Antonin to name a few

- folks from my former band CUC, namely Couscous, TG, Phiniwn, Chapon, Rufa, Maitresse to name a few

- Martin, Clém and Hugo for the nights at the Bouillon Belge and more

- as well as Jérémy and Nico (Gislais)

Although the core work of this project has been conducted through the last 4 years, it would be deceitful to think that only those who supported me through this period had

a significant impact. Throughout my life, I had the chance to meet a countless number of individuals who, one way or another, affected my career in a positive way and ultimately contributed in leading it to this thesis. A vast majority strongly supported me all along, believing continuously in my ambitions; others were more interested in voicing unjustified hatred and disbelief. I would like to express my extreme and sincere gratitude to the former majority: your support strengthen my will through the brightest and darkest hours. That said, I am composedly thankful to the latter group: your incredulity fueled my spite to prove you wrong. Among those who believed in me, few also were direct actors in the chain of deciding opportunities that lead me to starting this PhD project. I would like to give a shout out below to a non-exhaustive list of those I haven't mentioned already and whose past support and trust I consider a contribution to this thesis.

To Christophe Sauty, Andreas Zech, Marie-Christine Angonin and Hervé Rétif for making possible, as part of my studies at Télecom Bretagne, the validation of a Master degree at the Observatoire de Paris-Meudon and a necessary step for me to pursue with a PhD thesis.

To Julio Navarro for introducing me to computational cosmology and triggering my interest to this field through my 2nd internship in the University of Victoria.

To those in Victoria whose friendship had leaded me to understand that I needed to come back, partially driving my motivation in doing this 2nd internship, namely Chris, Jason, Azi, Zoe, Masen, Charli, Hannah.

To Sara Ellison for allowing me to discover the world of academic research in astrophysics through my 1st internship in the University of Victoria.

To Christian Roux, Bruno Fracasso and Alain Peden from Télecom Bretagne, Alain Mallet from the CNES, and successively Pierre Pellat-Finet, Valerie Barthe and Michel Lefebvre, who put their trust into me and through a chain of contact or through their refereeing made this 1st internship in the University of Victoria possible.

To Stéphane Komilikis, Christian Leboeuf, Anne-Sophie Geney, Francois-Xavier Boité and Dominique Leclerc who forged my passion for astronomy, physics and math-

ematics through their courses in prépa, high school and middle school.

To so many friends who encouraged me: to Paris housemates Nono and Ale; to Master classes comrades Christophe and Étienne; to friends from Victoria Seb, Zack, Trystyn, Chelsea, Kyle and Holly ; to friends from Toulouse Romain, Nat, Anthéa, the Trous Balourds and the Gimmick 5 Syndicate; to friends from Télecom Bretagne Irène, Céline, Dédé, MiniMoi, Rémy, Julie, PBouli, Mylou, Pucci, Simon, Torres, Antoine, Flo19, Diane, Chaterton, Gautier, Beno, LeNain, Ilker, P-J, Meyer, Aurel to name a few; to friends from prépa Nicolas (Striebig), Laurent, Florence, Elsa, Dustin, Hadrien, JC, Soso and Cassagne; to many other friends, Joseph, Nicolas (Maia), Marie-Lys, Christopher, Clara, Xuan, Odile, Sylvie, Steph, Bertrand, Tiffanie, Florian, Milton, and those that I forget.

To Anne-Marie Chapelier, my schoolteacher who originally made me discover astronomy as a young pupil through an elementary school essay, and to Jérome Beaufumé and Antoine Giard with whom I prepared this essay.

To my family as a whole, especially to my auntie Christiane Vulvert and her daughter, my cousin Laurence Vulvert-Haury, who, with my mother, were the first to set off and nourish my interest for science through our regular holiday museum visits.

To my second half, my partner in life, Daniela Tejada Martinez, who I would have mentioned at each line of this already-too-long acknowledgement if I could, for how much she means to me. The comfort you brought me all along, especially in those last weeks through our life in Valdivia, has been a priceless moral support.

Lastly, I am deeply grateful to my close family, to my brother Emmanuel Thob, my father Francois-Xavier Thob and my mother Anne-Valérie Thob (née Roumeaux): despite me never being around, they have persistently supported all of my ambitions, persistently given me all the help I could need, persistently offered me the best of themselves so I could succeed. I owe my entire life to them, and that includes this thesis.

ADRIEN CHRISTIAN RENÉ THOB   JULY 9, 2019

"Je suis dans l'espace, avec un vieux... Je vous raconte pas ça au hasard! Quand je me suis réveillé j'ai tout de suite pensé à vous! L'espace... Ça a toujours été votre truc ça, l'espace."

- Arthur Pendragon - Kaamelott Livre VI Tome 9 «Dies Irae»

"Remember to look up at the stars and not down at your feet. Try to make sense of what you see and wonder about what makes the universe exist. Be curious. And however difficult life may seem, there is always something you can do and succeed at. It matters that you don't just give up."

- Stephen Hawking

Chapter 1

General introduction

Our world sits about halfway from the centre of a flat disky structure of stars that most astronomers, over a 100 years ago, could barely conceive the nature of. And the evidence was glaring: every human civilization has observed this bright band of light stretching over the night sky, feeding their various mythologies. However, the Milky Way, as we name it, is only one of a myriad of such galaxies and it was only recently that we differentiated them from other nebulae - recognising them as so-called "island universes". After the start of the 20$^{\text{th}}$ century, great breakthroughs bolstered this understanding, jointly with the debate over the expanding nature of the Universe.

Astronomers then had a vastly different perception of the cosmos: it consisted of a single structure of stars that is the Milky Way, and what we observed as other galaxies were interpreted as nebulae contained within it. But after Slipher (1913, 1915, 1917) performed measurements of peculiarly high radial velocities for some so-called "spiral nebulae", the theory[1] according to which they were not part of the Milky Way strengthened. While Curtis (1917) argued that the "island universe" hypothesis was supported by contemporary detections of novae in some of these spiral nebulae, Shapley (1919) argued against it, showing that, inter alia, objects of the Milky Way had similar velocities[2]. The "island universe" hypothesis eventually settled after distance measurements

---

[1]already suggested centuries before (Wright, 1750; Kant, 1755)

[2]this disagreement leaded eventually to the "Great Debate" on April 26, 1920 between the 2 astronomers at the National Academy of Science (Shapley and Curtis, 1921)

of various "nebulae" were achieved (Opik, 1922; Hubble, 1925, 1926a, 1929b), estimating the Barnard's, Triangulum and Andromeda galaxies to be respectively at 214, 263 and $275\,\mathrm{kpc}$ from us, beyond the Small Magellanic Cloud, revealing them to be other galaxies and unveiling also the first evidence for an expanding Universe through the Hubble (1929a) law.

Indeed, cosmology has always been a field of study closely linked to galaxy formation, and the former also was shaken up with the discoveries of Hubble (1929a). By revealing that, the further away that they are, the faster galaxies move away from the Milky Way, Hubble provided the observational foundation to the idea that the Universe was expanding. However this challenged the prevailing idea of a steady-state cosmos in theoretical cosmology that many defended. For instance, after he published his theory of general relativity (Einstein, 1916), Einstein (1917) added a constant λ - famously known today as the cosmological constant Λ - to his equations to keep its uniformly matter-filled cosmological solution steady and finite. Similarly, while questioning this constant, de Sitter (1917a,b) had proposed a solution for a matter-free Universe, but intentionally using coordinates that kept it stationary. Nevertheless, a number of astronomers grasped the potentially evolving aspect of the cosmos when solving these equations: that was the case of Friedmann (1922) and Lemaître (1925). Both independently proposed this theoretical expanding nature, the former directly reducing the equations of general relativity, the latter when modifying the de Sitter (1917a,b) solution into an exponentially expanding one[3]: these led to the Friedmann equations and Friedmann-Lemaître-Robertson-Walker (FLRW) metric used today. Later, Lemaître (1927) would precede Hubble (1929a) by giving the first estimation of what would be later known as the Hubble constant H_0: the rate of change of the rate at which galaxies recede faster the further they are from each other. Lemaître (1931) then proposed this expansion to take its origin in a singularity, which he would call the "Primeval Atom", forming the cornerstone for the Big Bang theory which would later establish itself against the Steady State model of a non-evolving cosmos.

The Big Bang theory is an essential foundation for the understanding of galaxy evolu-

---

[3]that became known as the de Sitter Universe

tion in that the implied beginning for the Universe requires galaxies must have had a formation process. The following decades of the 20th century saw a wave of developments supporting this model, most importantly the theory of big bang nucleosynthesis explaining the cosmic element abundances (Alpher et al., 1948) and the first detection of the cosmic microwave background (CMB - Penzias and Wilson, 1965). This would bring a physical framework to the study of the formation of large scale structures, arising from the collapse of primordial density fluctuations seen in the anisotropies within the CMB. This ended up being tightly linked to another major modern astrophysical field of research that had its impact in the study of galaxy formation: the hypothetical missing gravitational mass also known as dark matter. During the second half of the 20th century, the work of Rubin and Ford (1970) and Rubin et al. (1980) motivated the apparent existence of this hypothetical form of matter[4]. When looking at the velocity curves of various spiral galaxies, they appeared to rotate too fast with respect to the gravitational influence of the visible luminous matter, suggesting that a significant amount of mass might not be seen. Several observational works would later corroborate this hypothesis and generalize it to the entire Universe (Ostriker and Peebles, 1973; Einasto et al., 1974; Ostriker et al., 1974; Mathews, 1978; Faber and Gallagher, 1979). Contemporaneously, cosmologists found an independent contradiction when, assuming the cosmos was made of ordinary baryonic matter, models of galaxy formation via gravitational processes were ruled out by the contemporary upper limits of the CMB anisotropies (Sachs and Wolfe, 1967; Silk, 1967, 1968; Peebles and Yu, 1970; Doroshkevich et al., 1978; Wilson and Silk, 1981; Uson and Wilkinson, 1984). However, various works demonstrated that by splitting the content of matter between baryonic and a dominant form of dark matter - more likely of the cold type - predictions could eventually match those measurements and today's large scale structures (White and Rees, 1978; Peebles, 1982; White et al., 1983; Blumenthal et al., 1984; Davis et al., 1985; Frenk et al., 1990). This discovery was a first step towards what is today accepted as the standard model for cosmology: the ΛCDM model.

---

[4]already previously hypothesized by Poincaré (1906), Kapteyn (1922) and Zwicky (1933)

1.1 A consensus around the ΛCDM paradigm

The ΛCDM model abbreviates 2 concepts: CDM stands for Cold Dark Matter and Λ stands for the cosmological constant of Einstein (1917). It describes the Universe as a geometrically flat[5] expanding one, starting from a space-time singularity immediately followed by a brief exponential expansion known as cosmic inflation[6], after which it follows the Friedmann equations within a FLRW metric. In its composition, the Universe is made of various contributions to the energy-matter density:

- the first (Ω_b) and least abundant matter contribution is the ordinary matter that we are constituted of, often termed baryonic matter,

- the second contribution (Ω_c), and most abundant form of matter, is a cold type of dark matter, non-relativistic (moves slowly with respect to the speed of light), dissipationless (cannot diffuse its thermal agitation via electromagnetic radiation) and collisionless (only interacts gravitationally with itself or baryons),

- the third and today's dominant contribution (Ω_Λ) is a form of energy called dark energy, represented by Λ for its theoretical similarity with the cosmological constant of Einstein (1917) within the equations of general relativity (it has negative pressure and accelerates the late-time expansion of the Universe),

- and lastly, the cosmic microwave and neutrino backgrounds form a radiation contribution, negligible today but dominant in the early Universe.

Latest CMB best-fit measurements from the Planck satellite (Planck Collaboration, 2018, Table 6) imply present-day estimates of each contribution at $\Omega_b \sim 4.9\%$, $\Omega_c \sim 26.5\%$ and $\Omega_\Lambda \sim 68.4\%$, for a Universe that is 13.8 billion years old with a Hubble constant today at $67.32 \, \mathrm{km \, s^{-1} \, Mpc^{-1}}$. Although it leaves fundamental open questions in the description of our Universe (the fundamental nature of dark matter and dark

---

[5]a flat geometry is mathematically represented by a metric with zero curvature, which, for any 3 distinct points in space, the 3 angles that separate the 3 associated segments will always sum up to exactly $180°$.

[6]although the cosmic inflation is not "part" of the ΛCDM model, it is today considered standard

energy, the origin of the cosmic inflation, etc), the ΛCDM model has progressively become established since the 1980s to become today's paradigm for our cosmogony.

1.1.1 The cold dark matter structure formation

Despite the fact that among all hypothesized particle candidates for the composition of dark matter, no detection of these has been reported to this day, the existence of dark matter is strongly supported by the amount of phenomenologically-independent observational problems it resolves in a compelling fashion. It helps to explain the dynamics of galaxies in various observed clusters (Zwicky, 1933, 1937), and the high radial profiles of rotational velocities in the outskirts of galaxies which should otherwise be lower and radially decreasing (Rubin and Ford, 1970; Rubin et al., 1980). It fixes the necessary missing mass for causing the strong gravitational lensing seen around large clusters (Tyson et al., 1990). It acts as a convenient gravitational catalyst for the collapse of baryonic matter in the early-Universe which otherwise would be too efficiently supported by dominant radiation to form the seeds of the structures we see today (Ma and Bertschinger, 1995). That said, another possibility could be that no missing matter exist and our current paradigm for gravitation - general relativity - is incomplete[7](Milgrom, 1983), but most alternatives appear undermined by the study of structures with dark matter that is either spatially displaced (Clowe et al., 2006) or seemingly absent (van Dokkum et al., 2018).

As mentioned earlier, cosmologists in the 1980s understood the potential of a dark matter dominated Universe to reproduce the observed CMB fluctuations. In this effort, some first hypothesized that dark matter could be comprised of neutrinos because of its weak interaction with luminous matter: an example of "hot" dark matter (HDM) with ultra-relativistic velocities. Because of its high free streaming length, structures would form first in a Zel'dovich (1970) "pancakes" scenario, followed by the fragmentation into smaller clumps that form the galaxies (Bond et al., 1980; Doroshkevich

---

[7]which is very likely for different reasons that go beyond the scope of this thesis (need for a theory of quantum gravity), but for the case of modified gravity models, those are not compelling enough due to their ad-hoc executions or calibrations that require physical explanation.

et al., 1981; Zeldovich et al., 1982; Bond and Szalay, 1983). Concurrently, others proposed non-baryonic dark matter models behaving less relativistically: "warm" (WDM - Blumenthal et al., 1982; Bond et al., 1982) and "cold" dark matter models (CDM - Peebles, 1982). In these models, the formation of structures proceeds in a bottom up fashion, with smaller structures forming first and merging together in a hierarchical way. Shortly after, White et al. (1983) ruled out HDM by revealing simulations of a neutrino-dominated Universe could not retrieve the observed clustering scale of galaxies while Blumenthal et al. (1984) showed their model of structure formation with CDM have great predictive power in fitting the observed Universe.

1.1.2 Freezing quantum fluctuations through cosmic inflation

Simultaneously with the debate over the presence of dark matter in the Universe, and its cold/warm/hot nature for the growth of observed structures, other cosmological questions demanded solutions. First, because information cannot move faster than the speed of light, distant positions in space should have had strong variations in density at decoupling, but the CMB's temperature appears paradoxically homogeneous - this is the "horizon" problem. Secondly, within the framework of the Friedmann equations, the evolution of the Universe with marginally non-zero initial curvatures should lead to an extreme curvature at the present time (a re-collapse if positively curved or a stronger expansion if negatively curved), implying that the initial Universe would have needed to have a fine-tuned flat curvature - this is the "flatness problem". To solve both of these problems, a trick was proposed in the late 70s & early 80s: a brief temporary phase of exponential expansion in the very early Universe, the cosmic inflation.

While various authors independently worked on inflationary-like solutions (Starobinsky, 1980; Kazanas, 1980; Sato, 1981), it is accepted that Guth (1981) was the first to use the term of "inflation", proposing a scenario attempting to solve both of these problems. His model was later modified by Linde (1982, 1983) and Albrecht and Steinhardt (1982) to correct some of the issues Guth (1981) pointed at. Through inflation, the homogeneity of the Universe at decoupling is explained by the fact that, pre-inflation,

all locations in today's observable space were contained within a volume that made them sufficiently causally connected to alleviate irregularities. Also, because of the subsequent inflationary phase, any pre-inflation initial curvature is flattened, making the post-inflation Universe flat enough to avoid curvature divergence during its lifetime, thereby resolving the flatness problem. A consequence of this is the freezing of pre-inflation quantum fluctuations, inflating microscopic quantum fluctuations into the macroscopic regime, which we now see in the CMB: the seeds that would later collapse to form the present structures.

1.1.3 The accelerating expansion via dark energy

The Guth (1981) cosmic inflation phase is similar to a phase under the influence of a cosmological constant as the result of the energy released by vacuum decay. Also, cosmogonies with a cosmological constant Λ had been re-considered decades before due to the observations of quasi-stellar objects with brightness to redshift relations that could be explained with a positive Λ (Petrosian et al., 1967; Shklovsky, 1967; Kardashev, 1967). This had also led Zel'dovich (1968) to suggest that a quantum vacuum state itself could hypothetically exhibit a non-null energy density similar to a cosmological constant - although his estimate differed from those of cosmologists by 45 orders of magnitude. Therefore, when evidence supported a total matter density parameter Ω_m near 0.1, despite the flatness of the Universe ($\Omega = 1$), this led some to propose Λ as a solution (Turner et al., 1984). After cosmological simulations which included this constant proved to be more consistent with the observed large scale structures than those without a constant (Davis et al., 1985; Efstathiou et al., 1990), the ΛCDM cosmogony was on its way to becoming the new paradigm.

The 90s would then bring further evidence supporting a non-null cosmological constant value. With the Cosmic Microwave Background Explorer (COBE) satellite discovery of anisotropy in the CMB (Smoot et al., 1992), Wright et al. (1992), Efstathiou et al. (1992) and Kofman et al. (1993) showed that a CDM model of structure formation including a non-zero cosmological constant normalized on the COBE detection

may be consistent with large scale observational data. By the mid 90s, a set of strong observational constraints made such a model more and more favorable (Ostriker and Steinhardt, 1995). A conclusive direct detection was brought with the discovery of the acceleration of the Universe's expansion when Riess et al. (1998) and Perlmutter et al. (1999) used type Ia supernovae as standard candles in distant galaxies for measuring their distance independently of their redshift. Since then the ΛCDM theory has become the current paradigm, and would later be corroborated by various observational campaigns such as the 2nd generation CMB measurement satellite Wilkinson Microwave Anisotropy Probe (WMAP; Spergel et al., 2003, 2007).

1.2 Galaxy formation and diversity

A first attempt in investigating the diversity of galaxies can be found in the work of Hubble (1926b) with its renowned morphology classification. It opened an entirely new field of study to astronomers: the following decades to this day flourished with further deepening and development of our understanding of how galaxies are distributed and how they evolved into their present state over cosmic time. Today the leading description for their formation uses the ΛCDM paradigm as its main foundation with a gravitational clustering of matter over time in a hierarchical bottom-up fashion. Matter at the start of this process existed mostly in its cold dark form or in its baryonic form as a diffuse gas. With the compression of gas as a result of this clustering, various regions would become denser and turn into stars within protogalaxies. Those structures would then merge later on into bigger ones, following the gravitational potential of a multi-scale web of matter with filaments connecting into high density nodes where can be found the largest clusters of galaxies.

All of this hierarchical merging happened in parallel with their baryonic processes, such as supernovae, black hole formation and growth, or the formation of more stellar content. Today, these processes are suspected to have been affecting galaxies during their formation, and are known as feedback processes. The effects of such processes were revealed when N-body simulations of large-scale structures based on collisionless

non-baryonic dark matter could not reproduce distinct observed scaling or statistic laws as we will detail it in Section 1.2.1. Galaxies are then sculpted by an intricate synthesis of environmental processes, such as their merging history, and internal processes, such as their star formation history, that need to be considered together without neglect of one over another.

1.2.1 Hierarchical formation

As mentioned earlier, the hierarchical model of the formation of structures was pioneered during the 1970s and 1980s (Press and Schechter, 1974; White and Rees, 1978; Fall and Efstathiou, 1980; Blumenthal et al., 1982; Bond et al., 1982; Peebles, 1982; Davis et al., 1985). In this scenario, overdensities that are dense enough are not erased by the cosmological expansion and are gravitationally bound to collapse on themselves. This occurs first for the cold dark matter overdensities, unaffected by radiation, unlike baryonic matter prior to recombination. After this recombination initiated the "dark ages", an epoch named as such because of the absence of radiation emitting sources like stars and the opacity of the neutral gas. The potential wells produced by the dark matter from earlier collapse become strong enough to attract the baryons, now in a neutral atomic state. This initiates the formation of protogalaxies and of the first stars, leading to the reionization of their diffuse gas environment, giving its name to the reionization epoch during which it happened. From then to this day, the rest of the evolution results in a bottom-up merging of the past smaller haloes/galaxies into bigger ones today. The way this process shaped the distribution of haloes can be found in the mass function: the distribution of haloes/galaxies accordingly to their mass, illustrated in Figure 1.1.

Specifically, the mass function shows at a specific epoch the number density of galaxies of a given mass, with, in a hierarchical merging context, more massive structures being less common than their lower mass counterparts. Over the years, a vast number of galaxy surveys have been conducted and have yielded measurements of this function at different lookback times using stellar masses of galaxies inferred over a wide range
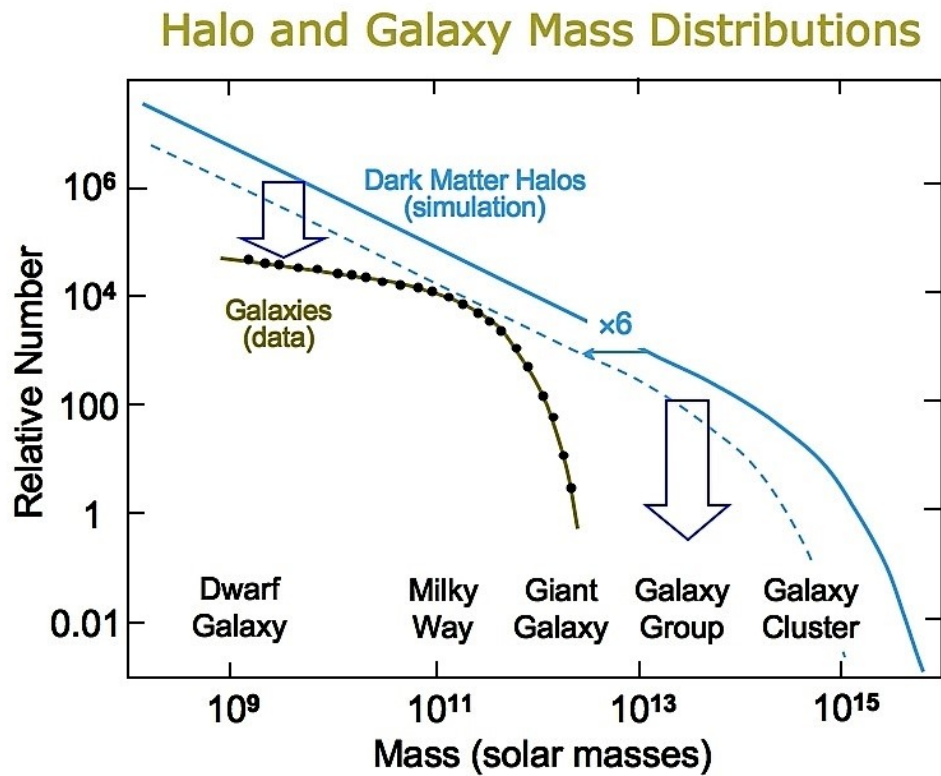
Figure 1.1: The difference between the halo mass function and the stellar mass function as adapted from online material by M. Whittle. The blue line corresponds to the mass function obtained from N-body simulations, its dashed counterpart represents the expected baryonic mass function if all galaxies have an equal ratio of baryons, the black curve with dots sketches the actual observed galaxy stellar mass function. The y-axis encodes the relative population number per bin of mass in logarithmic scale. The x-axis encodes the stellar mass of the galaxy in a logarithmic scale.

of redshifts (Cole et al., 2001; Norberg et al., 2002; Bell et al., 2003; Baldry et al., 2008; Li and White, 2009; Ilbert et al., 2010; Baldry et al., 2012; Tomczak et al., 2014). However, comparing those with mass functions generated from simple N-body simulations reveals discrepancies as seen in Figure 1.1, specifically in the profile of this function. While simulated mass functions show consistently decreasing profiles, observed stellar mass functions exhibit a two-regime profile with the decrease being much steeper at higher mass, and more gradual at lower mass (Jenkins et al., 2001; Yang et al., 2003). The corollary is thus that galaxies must form in a markedly different fashion to the dark haloes that form in N-body simulations and do not represent true observed galaxies, and a naive 1:1 mass correspondence fails at matching both mass functions. Clearly then, additional physics governing the evolution of the baryons must be considered.

1.2.2   Star formation and colour bimodality

A galaxy will continuously change its gas content into stars, but this process can have varying efficiency, which can be studied through the star formation history. Galaxies can go through short periods of intense star formation, also known as "starbursts", and contrastingly, they can decline in star formation activity. The latter can happen when a galaxy exhausts its gas content after forming stars, or gets depleted of it through phenomena such as ram pressure stripping during merging, or when the gas state of pressure and temperature is suddenly changed to conditions unsuitable for collapsing into stars. In particular, when such phenomenon causes that decline in star formation to develop quickly, it is commonly described as "quenching". With recent surveys, it has been shown that instead of being uniformly distributed among all colours, galaxies tend to be found in 2 populations with blue or red colours (Strateva et al., 2001; Blanton et al., 2003; Baldry et al., 2004; Salim et al., 2007; Baldry et al., 2012; Schawinski et al., 2014) as illustrated in Figure 1.2, that have subsequently been called the "blue cloud" and "red sequence", with a minority of galaxies showing intermediate colours, forming a "green valley". This suggests that slow quenching, with the galaxy transitioning from the blue cloud to the red sequence through the green valley, is a rare case,
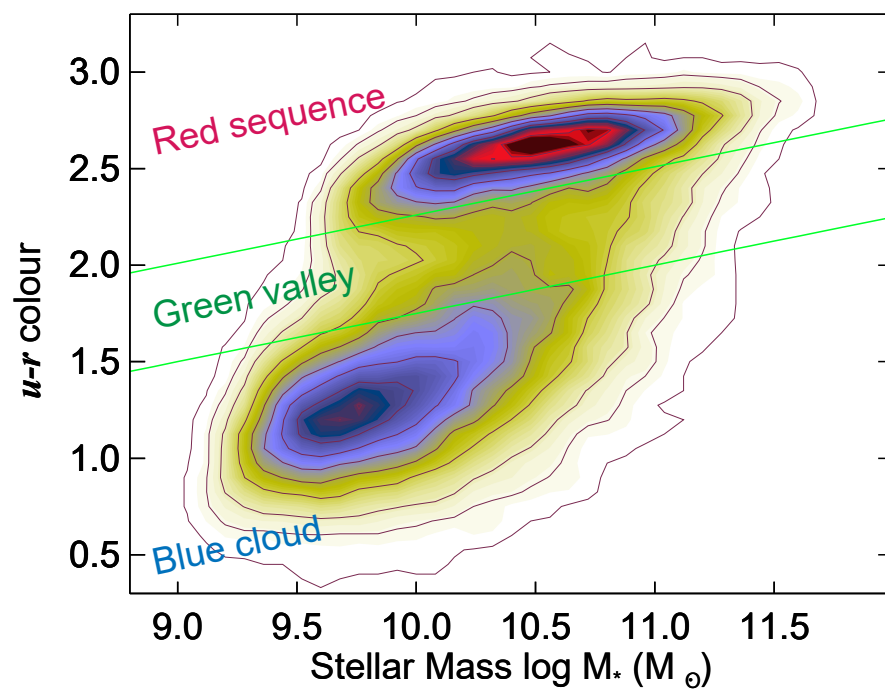
Figure 1.2: Colour-stellar mass diagram as adapted from Schawinski et al. (2014) via the 2D density function of observed galaxies. The y-axis encodes the colour $(u - r)$ of a galaxy with higher values representing redder colours and lower values representing bluer colours. The x-axis encodes the stellar mass of the galaxy in a logarithmic scale.
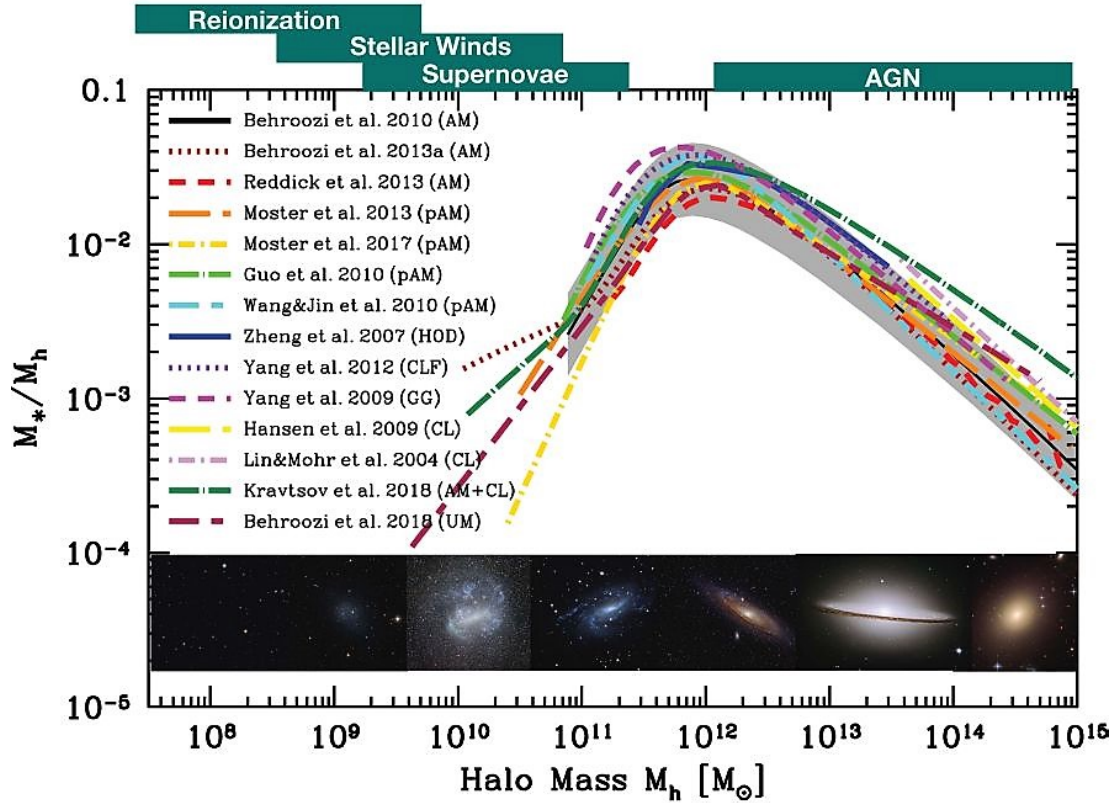
Figure 1.3: The galaxy stellar-to-halo mass ratio of central galaxies as represented by Wechsler and Tinker (2018) from a compilation of data shown in Behroozi et al. (2018). The y-axis encodes stellar-to-halo mass ratio of the galaxy in a logarithmic scale. The x-axis encodes the halo mass of the galaxy in logarithmic scale. At the top are added labels that identify the potential significant feedback processes that quench galaxies in the indicated mass range while the bottom part illustrates each mass by a relevant existing observed galaxy.

with quenching being more often due to rapid events.

1.2.3   Galaxy feedback processes

The discrepancy previously mentioned between collision-less simulations' mass functions and observed stellar mass functions can be equivalently examined via the stellar-to-halo mass ratio relationship with halo mass (Figure 1.3). Instead of having a uniformly constant profile, which would reflect the idea that a galaxy's stellar mass is a fixed fraction of its halo mass, the profile increases with halo mass until a turning point after which it decreases. This echoes with the observed two-regime profile of the stellar mass functions, and indicates that some feedback processes act against a possi-

ble harmonized co-evolution of a halo and its galaxy, depending on how massive it is. Those feedback processes have been suspected to be physical phenomena that regulate or even quench the galaxy's capacity to form stars, altering the stellar mass function of galaxies with respect to that of hierarchically-accumulated halo mass.

Several physical processes have been suggested to have such an influence, impacting the stellar formation of molecular clouds in a violent way thermally and/or kinematically, and the contribution of these to the stellar-to-halo mass ratio profile can be predicted. Populations of massive stars can regulate their neighboring interstellar medium, typically through supernovae that can dramatically heat up and blow away nearby diffuse gas (Dekel and Silk, 1986; Katz et al., 1996; Springel and Hernquist, 2003). Galaxies hosting a supermassive black hole in their centre can develop an active galactic nucleus: when enough gas accumulates in the vicinity of the black hole, a compact accretion disk forms in such conditions that intense quenching radiation is emitted (Silk and Rees, 1998; Kauffmann and Haehnelt, 2000; Di Matteo et al., 2005; Croton et al., 2006; Bower et al., 2006). It has been accepted that stellar mass regulation in low mass halos may be the work of supernova (SN) feedback during the course of the galaxy's life, while the higher mass galaxies may have undergone feedback from active galactic nucleus (AGN) phases (see for observational review Fabian, 2012).

Nonetheless, other physical phenomena have been considered for their contribution to the regulation of stellar formation in galaxies. As previously mentioned, after the formation of the first stars came a period of reionization due to their emitted ionizing UV radiation. When a gas cloud is ionized, the resultant high temperature and increased pressure prevent it from collapsing, and its efficiency at forming stars is reduced. It has been shown that the reionization of the first stars may have prevented the smallest halos from producing more stellar mass, expelling by thermal pressure their gas leaving them dark matter dominated (Bullock et al., 2000). In addition, as such pervading radiation kept inter-galatic diffuse gas at a temperature of 10000 K, it also halted their collapse into new proto-galaxies. Similarly, stellar wind influences are not only limited to the reionization epoch, but continue through the lifetime of the Universe with the most luminous stars. Lastly, merging itself can have a substantial role in the quenching
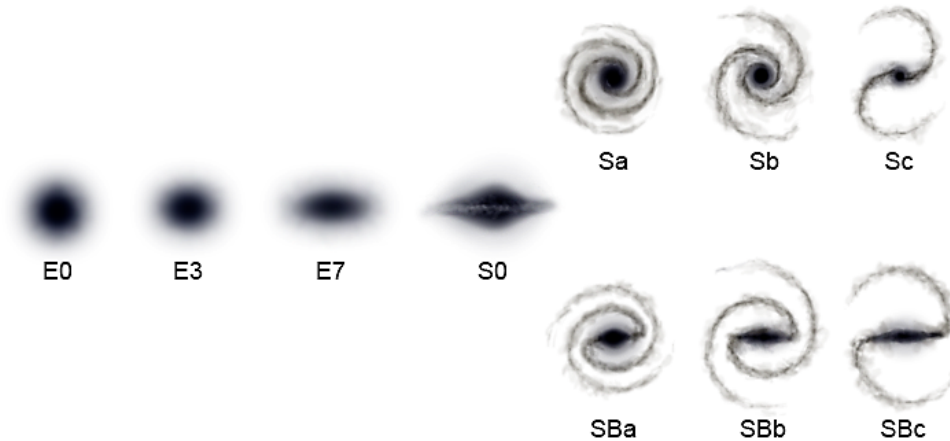
Figure 1.4: The Hubble (1926b) tuning fork classification of galaxies as adapted from Wikimedia Commons, with Hubble's naming system. The left side represents elliptical/early-type galaxies while the right side classifies spiral/late-type galaxies between 2 branches according to whether they have a barred nucleus or not.

of a galaxy, whether by stripping away its gas content or by triggering a starburst that quickly depletes it (Mihos and Hernquist, 1996).

1.3 Morpho-kinematics in galaxies

Galaxies are fascinating through the immense diversity of shapes they can display. As previously mentioned, one of the foundational works in studying galaxies was the classification of morphology of Hubble (1926b) that is still used today as a reference (improved by de Vaucouleurs, 1959). Despite the complexity of the galaxies he observed, he found underlying similarities to build a forked classification which is illustrated in Figure 1.4. This separated ellipticals, ranging them on the single end of that fork, from spirals, segregated according to whether or not they feature a central bar. Galaxies that could not fit this classification would be then denominated as of the irregular type, although many may have had their shapes disturbed by on-going merging interactions. Theorists understood that, within the hierarchical scenario, spirals must be the result of a slow and unperturbed angular momentum build up with a quiet merging history,

while ellipticals might have undergone major mergers. On the other hand, observers examined ways to quantify morphologies and studied their relation with other galaxy properties, such as their colour/star formation (Strateva et al., 2001; Schawinski et al., 2014), finding spirals and ellipticals to be respectively blue or red. Morphological properties fall within the fundamental concepts of galaxy formation in which different shapes can be the result of what stage galaxies are in their evolution.

1.3.1   Late and early type galaxies

Low redshift galaxies of distinct morphologies can not only look drastically different, but they also diverge in a range of other properties. The stellar mass spectrum can show strong variances in morphologies, with late-type galaxies primarily populating the low and intermediary masses, while most galaxies found at higher masses are of the early-type. This variety intertwines considerably with their star formation behaviours: we mentioned that late-type galaxies tend to have bluer colours than their early-type counterparts, suggesting that late-type galaxies undergo more recent star formation. On the other hand most early-type galaxies tend to often be gas depleted, consistent with their relatively low present-day star formation rates.

Massive early type galaxies may have resulted from the merging of the largest galaxies, making them subject to the gas depletion that occurs post-merging and blowing it out to leave it as a hot circumgalactic medium. They are composed of only old red stars and cannot form many new blue young ones. Late type galaxies such as our own have a more heterogeneous structure, between their bulge (barred or not), their disk and spiral arms. They continuously accrete cold gas from their neighbourhood, or strip it from lower mass satellite galaxies that interact with them through minor merging, giving them the necessary fuel for star formation (Sancisi et al., 2008). The substructures that compose them such as spiral arms produce the necessary gravitational instabilities to trigger their clumps of cold gas to form new young stars.

1.3.2 Diversity in kinematics

When we talk about morphologies, it makes sense also to consider stellar dynamics and the diversity of galaxies in this respect. After all, galaxy morphologies are mostly revealed by the luminosity of their stars, which possess individually their independent motion. The major form of dynamics that is seen in galaxies' stars are their overall rotational motion. If most of the stars are rotating around a single axis, we define the galaxy as rotation-supported. On the other hand, if all the orbits of the stars are in different orientations, we talk about dispersion-supported galaxies.

Those motions are greatly impacted by the gravitational interactions involved during the merging activity of a galaxy. Isolated evolution can also result in galaxies experiencing gravitational instabilities that result in the formation of substructures that perturb surrounding dynamics and scatter the stellar content. For such reasons, morphologies can be related to diverging forms of dominant dynamics. It has long been assumed that most early-type galaxies appear to have dispersion supported dynamics, while late-type galaxies exhibit more ordered, rotational motion. However, recent studies have revealed the need to revisit this correspondence, finding that observed galaxies can exhibit a greater variety of dynamics than often expected, especially with early-type galaxies, some of which having surprisingly high rotational support (Emsellem et al., 2007; Krajnović et al., 2013; Cortese et al., 2016; Graham et al., 2018).

1.3.3 Morphologies vs. kinematics: simulations as a laboratory

The recent observation of more heterogeneity in the relation between morphology and kinematics is the core subject of this work. We aim at getting a better understanding of why and how stellar motion varies between galaxies exhibiting similar morphologies. Despite the strong advances in observational techniques, there are still significant limitations to study in depth this matter, such as the incapacity to resolve individual stars and to measure 3-dimensional properties for these. On the other hand, recent development in simulations have resulted in significant progresses in computational

cosmology, and many simulations have become able to reproduce the most fundamental observed scaling and statistical relationships in galaxies (Dubois et al., 2014; Vogelsberger et al., 2014; Schaye et al., 2015; Khandai et al., 2015; Dolag et al., 2015; Hopkins et al., 2018).

Chapter 2

Simulating the Universe: computational cosmology

2.1 Introduction

In this chapter, after mentioning some general points on computational cosmology as a whole in Section 2.2, we cover in detail the model of the cosmological simulation we will use through this thesis in Section 2.3. As outlined in our introductory Chapter 1, the physics that drives galaxy formation is particularly intertwined and demands consideration of a variety of phenomena. Because such physics is strongly non-linear, and analytic approaches fail to produce the necessary predictive tools, simulations must be conducted to create a framework with which we can test existing theories. In this context, two main techniques have emerged in the few last decades to study galaxy formation in a cosmological context: semi-analytic models and hydrodynamical simulations. In the former technique, N-body collision-less simulations or Markov Chain Monte-Carlo generators are first used to produce a representative population of dark matter halos with their merging tree. Then, using the merging tree as a basis and assuming each halo hosts a galaxy, galactic baryonic properties are estimated through semi-analytic relationships i.e. phenomenological laws that have been obtained through either analytic approximations or empirical calibration. Despite successful predictions of vari-

ous recent semi-analytic models, their prescription of baryonic interactions can appear artificial of highly simplified in comparison with hydrodynamical simulations. This second technique finds its strength in the treatment it brings to baryons by computing both gravitational and hydrodynamical processes in a self-consistent way. Nevertheless, those also have a "semi-analytical flavour" as they need similar treatments to deal with, for example, the physical feedback processes that regulate galaxy evolution and which operate at scales below those resolved numerically: these are commonly known as "subgrid models". A crucial difference with respect to semi-analytical models is that the latter are forced to impose their phenomenological treatments on halo scales, whilst hydrodynamical simulations generally impose them on much smaller scales.

Recent years have been accompanied with a collection of groundbreaking cosmological simulations projects adopting different hydro+gravity solvers coupled with subgrid physics modules. We can notably quote the following projects for the breakthrough they represent in their capacity at reproducing key properties of the galaxy population: Horizon-AGN (Dubois et al., 2014), Illustris (Vogelsberger et al., 2014; Springel et al., 2018), FIRE (Feedback In Realistic Environments; Hopkins et al., 2014, 2018), EAGLE (Evolution and Assembly of GaLaxies and their Environments; Schaye et al., 2015; Crain et al., 2015), Massive Black II (Khandai et al., 2015) and Magneticum Pathfinder (Dolag et al., 2015). Among these, we will later focus on the project EAGLE: the large size and vast diversity of its galaxy population, with the fact its model enabled for the first time a cosmological hydrodynamic simulation to reproduce the galaxy stellar mass function with galaxies of realistic sizes, make this project an appropriate framework for studying the relationship between the morphologies and kinematics of galaxies. Owing to its success in yielding a realistic galaxy population, the EAGLE model has also served as a foundation on which several spin-off projects are built. We can notably cite the projects APOSTLE (A Project Of Simulations of The Local Environment; Sawala et al., 2015, 2016; Fattahi et al., 2016) that follows, in higher resolution zoom simulations, 6 Local Group-like regions of EAGLE, Hydrangea/C-EAGLE (Bahé et al., 2017; Barnes et al., 2017) that does the same for 30 EAGLE clusters with virial masses between 10^{14} and $10^{15.4} \, M_\odot$, Oppenheimer et al. (2016)

that produces zooms of 20 EAGLE Milky-Way-like halos implementing the tracing of 136 ions and their associated physics (such as non-equilibrium cooling rates), and E-MOSAICS (MOdelling Star cluster population Assembly In Cosmological Simulations within EAGLE; Pfeffer et al., 2018) that includes the formation and evolution of star clusters in zooms of 25 EAGLE Milky-Way-like halos. This legacy opens future applications for the methods and results that this thesis develops, as shown for the E-MOSAICS project in Chapter 5.

2.2 Cosmological hydrodynamics: generic structure

Hydrodynamical simulations can exhibit several differences from the choice of subgrid models, to the type of fluid dynamics solving algorithm. Nevertheless, despite these differences, most hydrodynamical simulations maintain a similar procedural structure, determining the matter configuration at each timestep from the previous one, starting with an initial configuration commonly referred as "initial condition" generated according to a chosen cosmology. This initial condition is usually the result of a 2 step process: a first step through which is generated an unperturbed matter distribution - one may choose between various existing kinds - and a second step where fluctuations corresponding to the chosen cosmology's power spectrum are simulated via pseudo-random displacements of the material support, to produce a realistic early Universe. The discretisation of time is chosen to satisfy precision requirements that vary from one simulation to another. At each timestep, 3 treatments are computed within a Cartesian space with periodic boundary conditions[1]:

- an algorithm that estimates the gravitational potential and accelerations induced by the matter configuration,

- a solver that computationally resolves self-consistently hydrodynamics forces[2],

---

[1]a space topology where all 3 directions are looping onto themselves also described as a three-torus topology

[2]in some cases developing it into a magneto-hydrodynamics solver

- and a combination of routines to simulate all subgrid processes which impact galaxy formation, such as the radiative cooling of gas, star formation, winds and mass loss due to stellar evolution, supernovae, black hole formation and growth, and AGN feedback.

In this section, we present some general details about each of these three aspects.

2.2.1 Gravity solver

General relativity is our most complete and verified modern theory of gravitation, but for purposes of cosmological galaxy formation, the Newtonian simplification can be used after some adaptation. Given the simulated scales and timesteps generally used, interactions can be well approximated within the Newtonian limit. Nonetheless, the cosmological expansion needs to be considered: every timestep generally includes calculations that depend on physical (rather than purely comoving) length scales through an evolving cosmic scale factor (which growth depends on the chosen cosmology) in a comoving/physical conversion framework.

Within this context, the gravitation solver estimates the gravitational potential produced by the simulated matter by solving Poisson's equation, to calculate the induced gravitational acceleration of the discretised mass elements sampling the matter distribution. The simplest way to perform such a simulation is through a direct N-body solving of a representative collection of known mass particles: the gravitational accelerations at each particle's position is computed directly by summing those of all other particles. Historically, early versions of it were inspired by simulations of electrostatic interactions due to the similarity between Coulomb's and Newton's law. However, while eletrostatic charges cancel each other at long distance allowing some performance driven approximations such as ignoring in the computation forces applied at long distance, masses do not and must be all considered no matter how far they are. In consequence, this method bears a $\mathcal{O}(N^2)$ computational scaling[3] which is prohibitive

---

[3]commonly referred as computational complexity: we use however the term "scaling" for clarity as the term "complexity" may alter the following message that reducing the computational complex-

for large cosmological calculations due to the large number of mass elements. Decades of research have focused on adequate approximations and optimizations to engineer efficient solvers, with a computational scaling of $\mathcal{O}(N \log N)$ while keeping a suitable precision. In most modern codes, the consensus appears to be found within the TreePM scheme, a "best-of-both-worlds" implementation between a Particle-Mesh (PM) algorithm to compute long-range forces and a hierarchical Tree assignation scheme at short-scale.

The speed-up that Particle-Mesh algorithms bring relies on a standard optimization in the computational field: the renowned fast Fourier transform scheme known to scale as $\mathcal{O}(N \log N)$. Poisson's equation is a spatial differential equation that consists of a Laplacian operator applied to the potential which needs to be found. As is commonly done in differential analysis, converting this equation into its spatial-frequency domain equivalent changes it into a simple linear equation. The potential can then be computed through the inverse Fourier transform of the solution of this spatial-frequency domain Poisson's equation given the Fourier transform of the spatial mass distribution. Therefore, by using fast Fourier schemes for each Fourier transform, the gravitational calculation can be greatly optimized. This requires though to map the mass distribution onto a mesh of cells (usually applying softening kernels to each particle), outputting a tridimensional regularly-sampled estimate of the gravitational potential. The level of sampling of this mesh then impacts greatly on the accuracy of the force estimate (computing the potential finite-difference), and the large meshes required for good spatial sampling can be very expensive in terms of the necessary memory footprint.

A trade-off is then necessary: it can be achieved by combining the PM scheme, for the contribution to the gravitational acceleration on large-scales, with a Tree implementation for the short-scale sources. The latter implementation assigns particles to a hierarchical octree structure: Cartesian space is recursively split into smaller cubes until each of them is occupied by a specified maximum number of particles. With the entire volume as a root and a recursion split dividing in 8 equal sized cubes, the particle distribution is organized as a multi-level tree of successively split cell-nodes,

---

ity/scaling can be achieved by using a more sophisticated algorithm.

with branches following those splits and reaching the smaller cubes, the cell-leaves. To compute the gravitational acceleration at the position of a particle, the closest particles are considered individually while more distant particles are grouped and represented by their centre of mass within cell-nodes of lower levels[4] yielding a similar force precision as a function of distance. To determine such configurations, we progress up the tree, starting from the root, by keeping the centre of mass of nodes that satisfy a given accuracy criterion, and opening the nodes that don't. This process reduces the computational scaling for all N particles to the $\mathcal{O}(N \log N)$ category.

2.2.2 Inclusion of gas dynamics

On a macroscopic scale, gas is commonly modelled using the continuum-fluid framework in which its properties are statistical measures from the local phase-space state of elements composing it on the microscocopic scale. Using this framework, gas behaves in accordance with the principles of fluid dynamics and satisfies the Euler equations. There are two philosophies regarding its computational modelling based on the Eulerian and Lagrangian specifications when looking at fluid motion. In the Eulerian specification, the fluid is discretized in space, fixing a constant volume for all fluid parcels. In the Lagrangian specification, all fluid parcels share the same constant mass, discretizing the fluid along centroids disseminated in such a way their density function follows the mass distribution. Both specifications exhibit strengths and weaknesses, and numerous cosmological simulation projects have used each. In the Eulerian case, most grid-based schemes have excellent accuracy for capturing shocks and instabilities but they often fail at conserving scalar properties. In the Lagrangian case, Smoothed Particle Hydrodynamics (SPH) has become the predominant choice and cannot suffer incorrect conservation by design, despite its capacity for adjusting its resolution with the flow, but it suppresses the development of shocks and instabilities. In this work, we will focus on the SPH scheme.

Within the SPH implementation, the fluid is modelled by smoothed particles, i.e. parti-

---

[4]closer to the root

cles in which the mass contribution is not "spatially contained" within their point-like position but distributed over a spherically symmetric radial density profile or "kernel". These kernels possess a characteristic radius called the "smoothing length" which varies from one particle to another and generally grows inversely to the density of the region where the particle sits. They must meet a condition of finite volume so that their profile must sum up to 1 when integrated over their spatial domain. Lastly, the resulting collection of smoothed particles trace all necessary continuum field intensive properties (e.g. pressure, temperature, flow-velocity, etc) so that, with this framework, their spatial profile can be retrieved by convolution with the particles' kernels. The equation of state of the simulated medium, named as such for that it relates its state variables such as pressure, density, temperature or internal energy, can be chosen accordingly to what fluid must be simulated.

The Euler equations are therefore conveniently changed from a spatial-differential set of equations to a set of linear equations: indeed all differential operators applied to such field properties can be linearly distributed to each term of the summed kernel-convolution; because these terms are product of the traced properties and the kernel, the former being constant with respect to position, these differential operators after their distribution are applied as gradients to the kernels. The kernels' gradients can be determined from the function which has been chosen for the kernel, leaving the traced properties as the ultimate variables of a system of equations. Consequently, by choosing the kernel to be null outside of its smoothing length and by adapting each particle's smoothing length so that the corresponding sphere contains a (nearly) fixed number of neighbouring particles, all kernel contributions for particles exterior to that sphere may be ignored in all calculations. The nearest neighbour search can be performed using the octree structure of the TreePM gravity solver (Section 2.2.1), which scales as $\mathcal{O}(N \log N)$, while the solution of the resulting set of Euler linear equations scales as $\mathcal{O}(N)$: this yields an overall scaling of $\mathcal{O}(N \log N)$.

For cosmological purposes, the SPH method is of great interest as it can be deployed very conveniently alongside the particle-based TreePM gravitation solver; in that con-

text, dark matter and baryons are represented by 2 different populations of particles[5], both participating in the gravity calculation, but in which only the baryonic particles participate in the SPH calculation. For this reason, significant effort has been devoted over the years to the SPH implementation in order to mitigate its weaknesses. For instance, it has been well established that SPH in its "standard" implementation fails at modelling fluid mixing processes at discontinuities such as instabilities and shocks (Morris, 1996; Dilts, 1999; Ritchie and Thomas, 2001; Marri and White, 2003; Okamoto et al., 2003; Agertz et al., 2007; Kitsionas et al., 2009; Price and Federrath, 2010; Bauer and Springel, 2012; Sijacki et al., 2012). This problem may be due to the explicit presence of the kernel-smoothed density in the SPH-version Euler equations ("density-entropy" formulation), which cannot be differentiated at discontinuities. This can be adjusted by deriving from these equations a revised implementation that depends on the pressure instead of the density ("pressure-entropy" formulation Hopkins, 2013). Finally, since SPH intends to solve the Euler equation which can be seen as a particular derivation for a non-viscous and non-thermally conducting fluid of the more general Navier-Stokes equations, which themselves do not reflect magneto-hydrodynamics, recent SPH implementations may include additional schemes to simulate relevant influences due to viscosity, thermal conduction and, very recently, idealised magneto-hydrodynamics.

2.2.3 Subgrid physics

It must be appreciated that simulations are limited by the models they employ and the scales over which they treat the included physics. For instance, in most implementations of the generic structure we just described, radiative processes are out of reach and must be incorporated via subgrid methods, especially for cosmological purposes in which isolated clouds of gas cannot cool another way. Similarly, since nuclear processes are not modelled and because these happen at scales well below those com-

---

[5]particles of the baryonic type can also be divided in more types to treat the subgrid physics we discuss in Section 2.2.3: in the case of the EAGLE model, those are the 3 types corresponding to gaseous, stellar and black hole particles as we discuss it in Section 2.3

monly used in cosmological simulations, aspects of stellar formation, evolution and death that depend on nuclear fusion cannot be simulated. Lastly, as we mentioned in Section 2.2.1, gravitation is legitimately approximated in the Newtonian limit, which proscribes all relativistic phenomena such as the formation and growth of black holes (BHs). Seeing that stellar and AGN feedback are vital for the formation of realistic galaxies (Section 1.2.3), stars and BHs must both have their respective prescription for their inclusion in the simulation.

Whether the fluid dynamics solver adopts a Eulerian or Lagrangian approach, stars and BHs are generally represented as particles: the SPH method holds an advantage in this regard since it already makes use of particles. As a result, on one hand, star formation can be integrated via the addition of a conditional treatment on gas particles for their conversion into stellar particles which represent stellar populations. On the other hand, BH creation treatment must be put in a cosmological context, where only supermassive BHs must be considered: because little is known about the formation of such BHs, these are usually integrated by the conditional addition of "sink" BH particles that serve as a basis for further supermassive BH evolution models. This ultimately creates a diversity of particles of 4 different types depending on whether they represent dark matter (DM), gas, stars or BHs, an implementation that is now widely used for SPH simulations (as shown in Figure 2.1). This framework lays the foundation for the modelling of the phenomenological impact caused by all relevant feedback processes through additional subgrid physics treatments.

From the population of stellar particles comes various feedback processes that must be considered, such as stellar winds and mass loss, supernovae, and the subsequent chemical enrichment of the interstellar medium (that becomes important for radiative transfer consideration). From the population of BH particles comes another set of feedback processes, notably an accretion treatment for nearby gas particles, a merging treatment for adjacent BH particles, and most importantly an AGN feedback implementation. Regarding the modelling of radiative processes, 2 major treatments must be considered, i.e. the radiative cooling and photoheating of gas which depends on its chemical enrichment, and a reionization UV background scheme. All these treatments
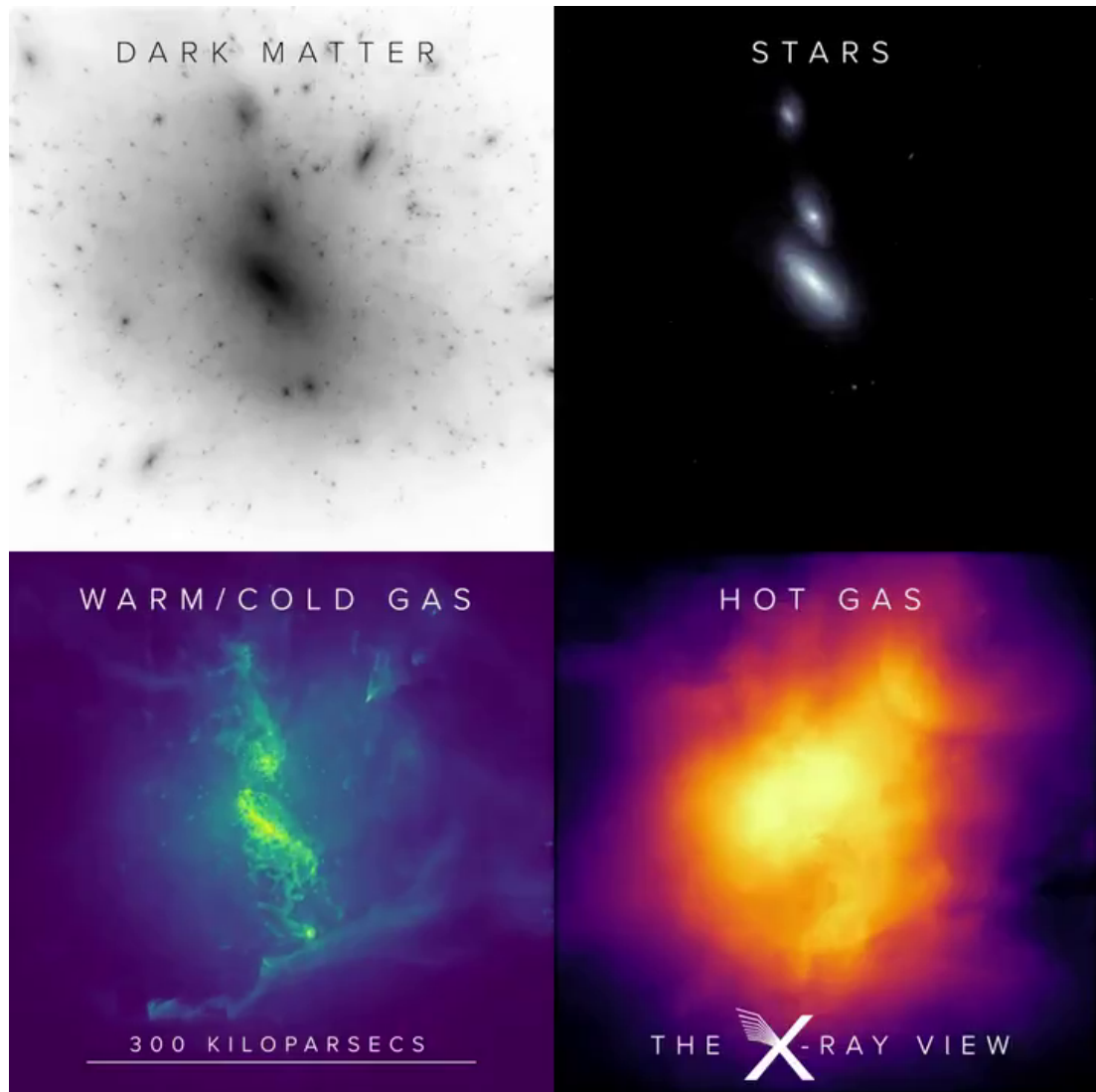
Figure 2.1: Example of the multi-component composition of a common cosmological hydrodynamical simulation. Each panel shows the same view of the simulation but displaying column densities of 4 populations of particles. The upper left shows the DM particles, the upper right shows the star particles, the lower left show the gas particles that are cold and warm, and the lower right shows the gas particles that are hot. Imagery taken from a rendering made with the software we presented in detail in Appendix A, and which was put together for the Lynx X-Ray Observatory for public outreach purpose (link in footnote of Section A.2.2).

(with the stellar formation and BH creation) result from both analytic and/or empirical relationships constructed with a set of free parameters. These must be calibrated from a restricted set of observed scaling and statistical relationships in order to make the simulation as realistic as possible and to enable its predictive power.

2.3 Simulations

This thesis has been conducted through the exploitation of 2 cosmological simulation projects: EAGLE (Evolution and Assembly of GaLaxies and their Environments; Schaye et al., 2015; Crain et al., 2015) through Chapters 3 and 4, and E-MOSAICS (MOdelling Star cluster population Assembly In Cosmological Simulations within EAGLE; Pfeffer et al., 2018) through Chapter 5. In this section we develop the detail about both simulations, starting with EAGLE in Section 2.3.1 and following with E-MOSAICS in Section 2.3.2. Lastly, we will describe in Section 2.3.3 how we identify a halo and a galaxy from the collection of particles that composes the simulations, as well as sampling criteria for the following studies.

2.3.1 The EAGLE model

EAGLE (Schaye et al., 2015; Crain et al., 2015) is a suite of hydrodynamical simulations of the formation, assembly and evolution of galaxies in the ΛCDM cosmogony, whose data have been publicly released (McAlpine et al., 2016). The EAGLE simulations are particularly attractive for our purposes, because the model was explicitly calibrated to reproduce the stellar masses and sizes of the present-day galaxy population. Comparison with multi-epoch observations highlights that the stellar masses (Furlong et al., 2015), sizes (Furlong et al., 2017), metallicities (De Rossi et al., 2017) and angular momenta (e.g. Swinbank et al., 2017) of EAGLE's galaxy population also evolve in a realistic fashion.

The EAGLE simulations adopt cosmological parameters from Planck Collaboration

(2014), namely $\Omega_0 = 0.307$, $\Omega_{\rm b} = 0.04825$, $\Omega_\Lambda = 0.693$, $\sigma_8 = 0.8288$, $n_{\rm s} = 0.9611$, $h = 0.6777$, $Y = 0.248$. They were evolved using a version of the N-body TreePM smoothed particle hydrodynamics (SPH) code GADGET3, last described by Springel (2005). This version incorporates modifications to the hydrodynamics algorithm and the time-stepping criteria, and includes a series of subgrid routines that govern, in a phenomenological fashion, physical processes that act on scales below the resolution limit of the simulations.

At 'standard resolution', the EAGLE simulations have particle masses corresponding to a volume of side $L = 100$ comoving Mpc (hereafter cMpc) realized with 2×1504^3 particles (an equal number of baryonic and dark matter particles), such that the initial gas particle mass is $m_{\rm g} = 1.81 \times 10^6\,{\rm M}_\odot$, and the mass of dark matter particles is $m_{\rm dm} = 9.70 \times 10^6\,{\rm M}_\odot$. The Plummer-equivalent gravitational softening length is fixed in comoving units to 1/25 of the mean interparticle separation (2.66 comoving kpc, hereafter ckpc) until $z = 2.8$, and in proper units (0.70 proper kpc, hereafter pkpc) thereafter. The standard-resolution simulations marginally resolve the Jeans scales at the density threshold for star formation in the warm and diffuse photoionised ISM. Higher-resolution EAGLE simulations adopt particle masses and softening lengths that are smaller by factors of 8 and 2, respectively.

The updates to the hydrodynamics algorithm, relative to traditional SPH implementations and which are detailed extensively in Appendix A of Schaye et al. (2015), comprise the pressure-entropy formulation of SPH of Hopkins (2013), the Cullen and Dehnen (2010) artificial viscosity switch, an artificial conduction switch similar to that proposed by Price (2008), the use of the Wendland (1995) C^2 smoothing kernel, and the Durier and Dalla Vecchia (2012) time-step limiter. The influence of these developments on the galaxy population realised by the simulations is explored in the study of Schaller et al. (2015b).

Gas particles denser than a metallicity-dependent density threshold for star formation (Schaye, 2004) become eligible for conversion into stellar particles. The probability of stochastic conversion is dependent on the gas particle's pressure (Schaye and Dalla Vecchia, 2008). Supermassive black holes (BHs) are seeded in haloes identified by

a friends-of-friends (FoF) algorithm run periodically during the simulation, and they grow by gas accretion and mergers with other BHs (Springel et al., 2005; Booth and Schaye, 2009; Schaye et al., 2015). The gas accretion rate onto BHs is influenced by the angular momentum of gas close to the BH (see Rosas-Guevara et al., 2015) and cannot exceed the Eddington limit.

Feedback associated with the evolution of massive stars ('stellar feedback') and the growth of BHs ('AGN feedback') is also implemented stochastically, using the particle heating scheme of Dalla Vecchia and Schaye (2012). This heating creates pressure gradients that drive outflows without the need to specify an initial wind mass loading or velocity, or to temporarily disable radiative cooling or hydrodynamic forces. The efficiency of stellar feedback is a function of the local density and metallicity of each newly-formed stellar particle. This dependence accounts, respectively, for residual spurious resolution-dependent radiative losses, and increased (physical) thermal losses in metal-rich gas. The dependence of the feedback efficiency on these properties was calibrated to ensure that the simulations reproduce the present-day galaxy stellar mass function, and produce disc galaxies with realistic sizes (Crain et al., 2015). The efficiency of AGN feedback was calibrated such that the simulations reproduce the relationship between the stellar masses of galaxies and the masses of their central BHs, at the present day.

The mass of stellar particles is $\sim 10^6 \, \mathrm{M_\odot}$, so each can be modelled as a simple stellar population (SSP). We assume an initial mass function (IMF) of stars of the form proposed by Chabrier (2003), with masses $0.1 - 100 \, \mathrm{M_\odot}$. The return of mass and nucleosynthesised metals from stars to the interstellar medium (ISM) is implemented as per Wiersma et al. (2009b); this scheme follows the abundances of the 11 elements most important for radiative cooling and photoheating (H, He, C, N, O, Ne, Mg, Si, S, Ca and Fe), using nucleosynthetic yields for massive stars, Type Ia SNe, Type II SNe and the AGB phase from Portinari et al. (1998) and Marigo (2001). The metallicity-dependent lifetimes of stars are taken from Portinari et al. (1998), whilst the 'lifetimes' of Type Ia SNe are described by an empirically-motivated exponential delay time distribution (Wiersma et al., 2009a). At each timestep, the mass and metals released

from evolving stellar populations are transferred from stellar particles to neighboring gas particles according to the SPH kernel, weighted by the initial, rather than current, mass of the particle (see Section 4.4 of Schaye et al., 2015). Following the implementation of Wiersma et al. (2009a), kernel-smoothed abundances are used to compute, element-by-element, the rates of radiative cooling and heating of gas in the presence of the cosmic microwave background and the metagalactic UV background due to the galaxies and quasars, as modelled by Haardt and Madau (2001). For the purposes of this calculation, the gas is assumed to be optically thin and in ionisation equilibrium. Stellar particles inherit the elemental abundances of their parent gas particle.

The simulations lack the resolution to model the cold, dense phase of the ISM explicitly. They thus impose a temperature floor, $T_{\mathrm{eos}}(\rho)$, which prevents the spurious fragmentation of star-forming gas. The floor takes the form of an equation of state $P_{\mathrm{eos}} \propto \rho^{4/3}$ normalised so $T_{\mathrm{eos}} = 8000\mathrm{K}$ at $n_{\mathrm{H}} = 0.1\mathrm{cm}^{-3}$. The temperature of star-forming gas therefore reflects the effective pressure of the ISM, rather than its actual temperature. Since the Jeans length of gas on the temperature floor is $\sim 1\,\mathrm{pkpc}$, a drawback of its use is that it suppresses the formation of gaseous discs with vertical scale heights much shorter than this scale. However, as recently shown by Benítez-Llambay et al. (2018), the primary cause of the thickening of non-self-gravitating discs in EAGLE is likely to be turbulent pressure support stemming from the gas accretion and energy injection from feedback, and the influence of the latter is likely to be artificially high. We comment further on the implications of this thickening for our study in Section 3.3.1.

2.3.2 The E-MOSAICS simulations

The E-MOSAICS project (Pfeffer et al., 2018; Kruijssen et al., 2019) is a suite of cosmological hydrodynamic simulations that also take account of the formation and evolution of stellar clusters. It achieves it by incorporating the semi-analytic model MOSAICS (MOdelling Star cluster population Assembly In Cosmological Simulations; Kruijssen et al., 2011) within the framework of the EAGLE model (described in

Section 2.3.1).

The implementation of the formation and evolution of stellar clusters is fully detailed in Pfeffer et al. (2018) introductory paper, but we present here a summarized overview. The formation is implemented so that stellar clusters are generated in a sub-grid fashion at each star formation event. Because many globular clusters are inferred to be very old ($> 6\,\mathrm{Gyr}$), observations of their formation are difficult to access, inhibiting the construction of authoritative formation models. Nonetheless, such models are developed in practice by assuming that the conditions in which they formed is analogous to those of the formation of young massive clusters (YMCs) seen in local galaxies, for which observations are accessible. The E-MOSAICS model also adopts this assumption.

Each time a gas particle is converted into a star particle as part of the star formation treatment of the EAGLE model, a fraction of its mass is assumed to be in clustered form. That fraction depends on the pressure of the parent star-forming gas particle, following a semi-analytic model calibrated on observations of the formation of YMCs in the Local Universe. Additionally, this treatment implements this mass "clustered fraction" as a population of globular clusters associated to the final stellar particle: the globular cluster masses are randomly drawn so that, in the limit of infinite sampling, they reproduce a Schechter (1976) initial mass function (with a slope of -2) for which a cut-off mass scale is considered, as a function of the pressure and gas dynamics from the parent gas particle.

Thereafter, those clusters lose mass via the usual stellar evolution treatment implemented within the EAGLE subgrid models, following the model of Wiersma et al. (2009b) using the stellar lifetimes from Portinari et al. (1998), as well as via 2 dynamical mass loss mechanisms that simulates the loss induced by local gravitational tides, the strength of which we calculate at each timestep. Both treatments depend on the local tidal field tensor and are implemented in such way that the lost mass is numerically removed from the clusters to be added to the field star fraction in each stellar particles. One of these dynamical mass loss treatments simulates the gradual cluster evaporation due to two-body relaxation in the local tidal field, which rate depends on the cluster mass and the local tidal field strength evaluated from the largest eigenvalue of the local

tidal field tensor. The second treatment emulates the cluster disruption due to shock heating, which rate depends on the cluster radius, the time since the previous shock and the tidal heating parameter evaluated from the integration of the tidal field tensor over the shock period.

The simulations are composed of the suite of 25 "zoomed-resimulations" mentioned in Pfeffer et al. (2018) referred as 'Halo_0XX' (XX identifying with a number from 0 to 24), as well as an additional simulation with full size volume of box length $L = 34\,\mathrm{Mpc}$ with identical resolution (1034^3 particles): we refer to the latter as Recal-L34N1024. All simulations adopt the Planck Collaboration et al. (2014) cosmological parameters, namely $\Omega_0 = 0.307$, $\Omega_\mathrm{b} = 0.04825$, $\Omega_\Lambda = 0.693$, $\sigma_8 = 0.8288$, $n_\mathrm{s} = 0.9611$, $h = 0.6777$, $Y = 0.248$. Resolutions are identical to that of the parent simulation of the Halo_0XX zooms (Recal-L025N0752 as named by Schaye et al., 2015), with gas particles being initiated at $m_\mathrm{g} = 2.25 \times 10^5\,\mathrm{M_\odot}$ and dark matter particles at $m_\mathrm{dm} = 1.2 \times 10^6\,\mathrm{M_\odot}$.

2.3.3 Identifying and characterizing galaxies

We consider galaxies as the stellar component of gravitationally self-bound structures. The latter are identified using the SUBFIND algorithm (Springel et al., 2001; Dolag et al., 2009), applied to haloes identified using the friends-of-friends algorithm (FoF). The substructure, or 'subhalo', hosting the particle with the lowest gravitational potential in each halo is defined as the 'central' subhalo, with all others considered as satellite subhaloes, which may host satellite galaxies. The coordinate of this particle defines the centre of the galaxy, about which is computed the spherical overdensity mass, M_{200}, for the adopted enclosed density contrast of 200 times the critical density. When aggregating the stellar properties of galaxies, we consider all stellar particles residing within a 3D spherical aperture of radius $30\,\mathrm{pkpc}$ centered on the galaxy's potential minimum; as shown by Schaye et al. (2015), this yields stellar masses comparable to those recovered within a projected circular aperture of the Petrosian radius.

We use the same sample of galaxies taken from the EAGLE volume Ref-L100N1504

through Chapters 3 and 4 in the study of their morpho-kinematic properties. To suppress environmental influences on the morphology and kinematics of galaxies, we focus exclusively on central galaxies. Since the characterisation of these properties also requires particularly good particle sampling, we require that galaxies have a present-day stellar mass $M_\star > 10^{9.5}$ $M_\odot$, which corresponds to a minimum of $\simeq 1700$ stellar particles. We further exclude from consideration galaxies with a resolved satellite subhalo (i.e. comprised of 20 or more particles of any type) whose mass is at least 1 percent of the central galaxy's total mass, and whose potential minimum resides within the $30\,\mathrm{pkpc}$ aperture. These selection criteria are satisfied by 4155 present-day central galaxies in Ref-L100N1504 which make our main sample through Chapters 3 and 4.

Through Chapter 5, we will be using instead galaxies from our suite of E-MOSAICS simulations, namely the full box Recal-L34N1024 and all 25 zooms Halo_000 to Halo_024. More details wil be given about specificities relative to particle populations representing globular clusters in Section 5.2.1, as well as that of the sample used in that Chapter.

2.4 Summary

We have presented throughout this Chapter the framework of study of this thesis by establishing the basics of computational cosmology and how to construct a simulation, and then describing those used in this work. We saw in Section 2.2 that modern cosmological simulations are mostly composed of 3 components: a gravitation solver, a gas dynamics solver and a set of subgrid physics routines. We described through Section 2.2.1 the TreePM scheme and explained the optimization reasoning behind its development. We followed with a presentation of the SPH implementation as one of the two main approaches for solving hydrodynamics in Section 2.2.2 as well as its latest improvements. We completed this structure by making a brief introductions to the variety of subgrid physics and their calibration in Section 2.2.3. Then, we presented in Section 2.3 the models of EAGLE and E-MOSAICS, the 2 simulation projects which are used in this thesis, respectively in Sections 2.3.1 and 2.3.2. We finally described

our definition of a galaxy with respect to those simulations in Section 2.3.3 with the criteria on which we define the samples in the following Chapters 3, 4 and 5.

Chapter 3

Morphologies, kinematics and galaxy colours

3.1 Introduction

The morphology and internal kinematics of galaxies are fundamental characteristics, both of which have an established tradition as a means to classify the galaxy population and infer aspects of its evolution over cosmic time. The two properties are closely related, with flattened, disky galaxies primarily supported by rotation, whilst spheroidal or elliptical galaxies exhibit greater dispersion support (for recent observational findings see van de Sande et al., 2017, 2018b; Graham et al., 2018). Moreover, it is well established that both quantities correlate broadly with other properties, for example mass (e.g. Dressler, 1980; Baldry et al., 2006; Kelvin et al., 2014), colour (e.g. Blanton et al., 2003; Driver et al., 2006) and star formation rate (Kennicutt, 1983; Kauffmann et al., 1993), indicating that they encode information relating to the formation history of galaxies. In particular, the recognition that the specific angular momentum of stars is markedly higher in late-type galaxies than in early-type counterparts (Fall and Frenk, 1983; Romanowsky and Fall, 2012; Fall and Romanowsky, 2018) led to the development of analytic galaxy evolution models in which the latter more readily dissipate their angular momentum throughout their assembly (e.g. Fall and Efstathiou,

1980; Mo et al., 1998), for example as a consequence of a more intense merger history.

As mentioned in Chapter 2, several families of cosmological simulations of galaxy formation have recently emerged that reproduce key characteristics and scaling relations exhibited by the observed galaxy population (see e.g. Vogelsberger et al., 2014; Schaye et al., 2015; Kaviraj et al., 2017; Pillepich et al., 2018). Such simulations evolve the dark matter and baryonic components self-consistently from cosmologically-motivated initial conditions, and the morphological and kinematical properties of galaxies emerge in response to this assembly. Crucially, the current generation of state-of-the-art cosmological simulations do not suffer from 'catastrophic overcooling' (Katz and Gunn, 1991; Navarro and Steinmetz, 1997; Crain et al., 2009), a failure to adequately regulate the inflow of gas onto galaxies, which results in the formation of a galaxy population that is generally too old, too massive, too compact, and too dispersion-supported. This success is in part due to improvements in the numerical treatment of hydrodynamical processes, but more importantly is due to the implementation of feedback treatments that effectively regulate and quench star formation (e.g. Okamoto et al., 2005; Scannapieco et al., 2008; Governato et al., 2009; Dalla Vecchia and Schaye, 2012; Scannapieco et al., 2012; Crain et al., 2015) and preferentially eject low angular momentum gas from the interstellar medium (e.g. Sommer-Larsen and Limousin, 2010; Brook et al., 2011; Agertz et al., 2011).

Numerical simulations of large cosmic volumes therefore afford the opportunity to examine the relationship between the morphological and kinematical properties of a well-sampled population of galaxies, the origin of scatter about such a relationship, and the connection between these properties and other observables such as mass, star formation rate and photometric colour. The markedly improved realism of the current generation of state-of-the-art simulations engenders greater confidence in conclusions drawn from their analysis.

In this Chapter, we examine the morphology and internal kinematic diversity of galaxies formed in the EAGLE simulations (Schaye et al., 2015; Crain et al., 2015), and their connection with photometric colour. This Chapter also prepares the next in which we will compare of the kinematic properties of EAGLE galaxies with quantitative mor-

phological diagnostics. We have added the morphological and kinematical diagnostics computed for this study to the public EAGLE database, enabling their use by the wider community. This work complements several related studies of the morphological and/or kinematical properties of EAGLE simulations, such as Correa et al. (2017), who show that the kinematic properties of EAGLE galaxies can be used as a qualitative proxy for their visual morphology and that this morphology correlates closely with a galaxy's location in the colour-stellar mass diagram; Lagos et al. (2018), who investigated the role of mass, environment and mergers in the formation of 'slow rotators'; Clauwens et al. (2018), who identified three phases of morphological evolution in galaxies, primarily as a function of their stellar mass; and Trayford et al. (2019), who explored the emergence of the Hubble 'tuning fork' sequence.

This Chapter is structured as follows. In Section 3.2 we introduce the relevant nomenclature and provide a brief analytical derivation of the relationship between morphology, kinematics and the anisotropy of the velocity dispersion from the tensor virial theorem. We then discuss our techniques for characterising the morphology and internal kinematics of simulated galaxies. We first cover our morphological descriptors in Section 3.3, by showing a detailed description of their computation in Section 3.3.1 before showing their diversity in EAGLE in Section 3.3.2. In Section 3.4 we cover our kinematics descriptors, presenting in Section 3.4.1 5 commonly used schemes in simulations, and looking at how they compare to each other in Section 3.4.2. We finally examine in Section 3.5 the relationship of these quantities with the location of the galaxies in the colour-stellar mass diagram. We summarise and discuss our findings in Section 3.6.

3.2 Galactic dynamics modelling

Because the stellar content of a galaxy can be looked at as a collection of individual particles, it is usual to think of it in thermodynamics terms, making the analogy between the stars constituting a galaxy and the molecules constituting a fluid. It is particularly common to employ thermal language when talking about stellar motion:

in this sense, a region in which stars have gained dispersive motion will be depicted as having "heated up". From there, modelling its statistical behaviour can be achieved using the collisionless Boltzman equation framework: we define a probability density function $f(\vec{r}, \vec{v}, t)$ over the 6D phase-space of all possible positions $\vec{r}$ and velocities $\vec{v}$ of the stars at the instant t, and using the continuity of the flow in phase-space we can find that it satisfies the following equation:

$$\frac{\partial f}{\partial t} + \vec{v} \cdot \overrightarrow{\nabla f} - \overrightarrow{\nabla \Phi} \cdot \frac{\partial f}{\partial v} = 0 \tag{3.1}$$

where $\Phi(\vec{r}, t)$ represents the gravitational potential. From this equation can then be derived the tensor formulation of the virial theorem, also known as tensor virial theorem, which takes the following form in a steady state:

$$2K_{ij} + W_{ij} = 0, \tag{3.2}$$

where K_{ij} and W_{ij} represent the kinetic and potential energy tensors. Binney (1978) and Binney and Tremaine (1987) show that the tensor virial theorem provides an analytical framework with which one can relate the morphology of oblate spheroids to their internal dynamics. Starting from Equation 3.2, the kinetic energy K_{ij} can be split into components denoting the streaming motion, T_{ij}, and the random motion Π_{ij}:

$$K_{ij} = T_{ij} + \frac{1}{2}\Pi_{ij}. \tag{3.3}$$

For an oblate system rotating about its short axis, we can use the notation $(v_{\rm rot}, \sigma_0, \delta)$, to be described fully in Section 3.4.1, σ_0 yielding:

$$T_{ij} = \frac{1}{2}M_\star v_{\rm rot}^2 \begin{pmatrix} 1/2 & 0 & 0 \\ 0 & 1/2 & 0 \\ 0 & 0 & 0 \end{pmatrix} ; \Pi_{ij} = M_\star \sigma_0^2 \begin{pmatrix} 1 & 0 & 0 \\ 0 & 1 & 0 \\ 0 & 0 & 1-\delta \end{pmatrix} \tag{3.4}$$

where $v_{\rm rot}$ represents the rotational velocity that is characteristic to the kinetic energy invested in ordered rotation, σ_0 represents the line-of-sight velocity dispersion along the (x, y) plane perpendicular to the rotation z-axis that is characteristic to the kinetic energy component invested in random motion along that direction, and δ represents the dispersion anisotropy parameter that quantifies the anisotropy between the latter velocity dispersion and that along the rotation axis ($\delta = 1 - \sigma_z^2/\sigma_0^2$ which also equals the anisotropy between the associated kinetic energies invested in random motion $1 - \Pi_{zz}/\Pi_{xx}$). These terms can be related to Cartesian components of the potential energy:

$$\begin{cases} \frac{1}{2}M_\star v_{\rm rot}^2 + M_\star \sigma_0^2 = -W_{xx} \\ M_\star(1-\delta)\sigma_0^2 = -W_{zz} \end{cases} \Rightarrow \frac{v_{\rm rot}^2}{\sigma_0^2} = 2(1-\delta)\frac{W_{xx}}{W_{zz}} - 2 \qquad (3.5)$$

where W_{xx}/W_{zz} is related to the flattening parameter, $\epsilon = 1 - c/a$. For convenience let us define the sphericity shape parameter $s = 1 - \epsilon$ and the term e, such that $s \equiv \sqrt{1-e^2}$. From Binney and Tremaine (1987, see also Roberts 1962; Binney 1978), we have for an oblate body that:

$$\begin{pmatrix} W_{xx} \\ W_{zz} \end{pmatrix} = -2\pi^2 G\frac{c}{a^3}\mathcal{S}\begin{pmatrix} Aa^2 \\ Cc^2 \end{pmatrix}, \ (\mathcal{S} \text{ being a constant})$$

$$\text{with } \begin{cases} A = \frac{\sqrt{1-e^2}}{e^2}\left(\frac{\arcsin e}{e} - \sqrt{1-e^2}\right) \\ C = 2\frac{\sqrt{1-e^2}}{e^2}\left(\frac{1}{\sqrt{1-e^2}} - \frac{\arcsin e}{e}\right) \end{cases}$$

$$\text{thus } \begin{cases} A = \frac{s}{1-s^2}\left(\frac{\arccos s}{\sqrt{1-s^2}} - s\right) \\ C = 2\frac{s}{1-s^2}\left(\frac{1}{s} - \frac{\arccos s}{\sqrt{1-s^2}}\right) \end{cases} \qquad (3.6)$$

$$\Rightarrow \frac{W_{xx}}{W_{zz}} = \frac{s^{-2}}{2}\frac{\arccos s - s\sqrt{1-s^2}}{s^{-1}\sqrt{1-s^2} - \arccos s}$$

The dashed tracks overlaid on the left-hand panel of Fig. 3.1 show the relationship between $v_{\rm rot}/\sigma_0$ and ϵ for $\delta = \{0, 0.1, 0.2, 0.3, 0.4, 0.5, 0.6\}$, derived using eq. (3.5) and (3.6).

This theoretical framework serves as a backbone for the definition and analysis of our
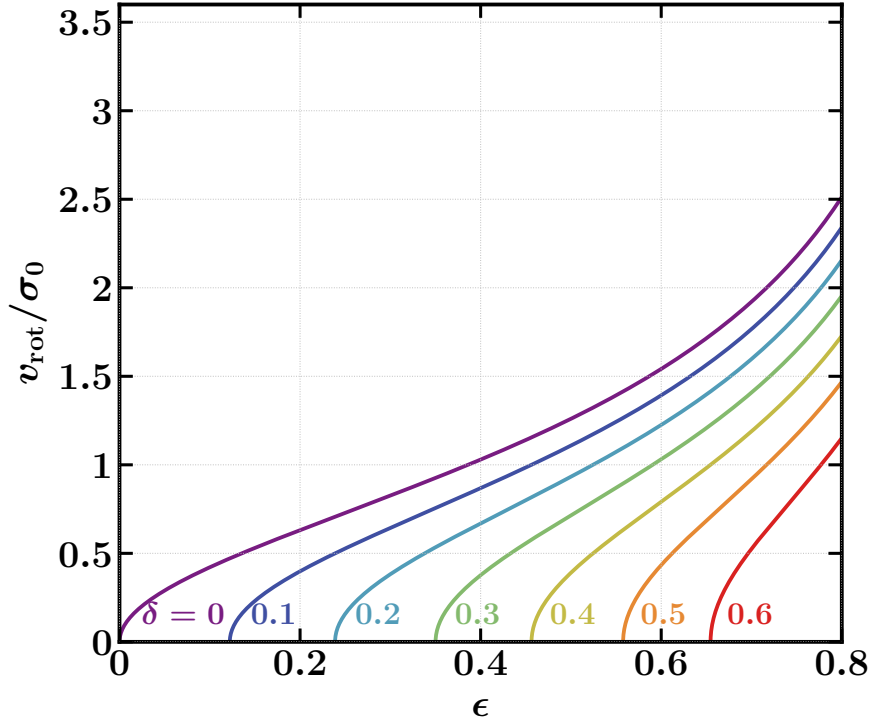
Figure 3.1: Curves representing the analytical relation between $v_{\rm rot}/\sigma_0$ and ϵ derived from the tensor virial theorem (eq. 3.5) for different value of the dispersion anisotropy $\delta = 0.0 - 0.6$ in increments of 0.1.

morphological and kinematics descriptors.

3.3 Measuring shapes in simulations

Numerous techniques have been developed for quantifying morphologies in observations: notably among them are the Sersic index (Sérsic, 1963, 1968; Graham and Driver, 2005), the Bulge-to-Total light ratio (Schade et al., 1995, 1996; Ratnatunga et al., 1999; Simard et al., 2002), the Gini coefficient (Abraham et al., 2003, using the statistical framework of Gini 1912), or M20, the 2nd order moment of the brightest 20% of the galaxy's flux (Lotz et al., 2004). Contrarily to observations however, parameters used in simulations can utilize the full potential of the 3D information that is available, allowing deeper insights when studying morphological properties. Also, we are interested in a technique to estimate the flattening parameter $\epsilon = 1 - c/a$ that allows the discrimination of oblate or prolate systems, as developed in our theoretical framework

from Section 3.2. Therefore, we decided to adopt morphological descriptions based on the quadrupole moments of the mass distribution, in which we estimate the 3 axes lengths of a characteristic ellipsoidal profile representing the mass distribution. We explain in detail the approach we use in Section 3.3.1 before presenting the diversity of EAGLE galaxies within the 2-parameter framework of such approach.

3.3.1   Quadrupole moments of the mass distribution

As discussed in Section 2.3.1 and demonstrated by Trayford et al. (2017), disc galaxies in the EAGLE simulations are more vertically-extended than their counterparts in nature. We therefore opt against performing a detailed structural decomposition to characterise the galaxies' morphologies, such as might be achieved by applying automated multi-component profiling algorithms (see e.g. Simard, 1998; Peng et al., 2002; Robotham et al., 2017) to mock images of the galaxies. Instead, we obtain a quantitative description of the galaxies' structures by modelling the spatial distribution of their stars with an ellipsoid, characterised by the flattening (ϵ) and triaxiality (T) parameters. These are defined as:

$$\epsilon = 1 - \frac{c}{a}, \text{ and } T = \frac{a^2 - b^2}{a^2 - c^2}, \tag{3.7}$$

where a, b, and c are the moduli of the major, intermediate and minor axes, respectively. For spherical haloes, $\epsilon = 0$ and T is undefined, whilst low and high values of T correspond to oblate and prolate ellipsoids, respectively. Clearly, these diagnostics are poor descriptors of systems that deviate strongly from axisymmetry but, as noted by Trayford et al. (2019), such galaxies are rare within the observed present-day galaxy population. The axis lengths are defined by the square root of the eigenvalues, λ_i (for $i = 0, 1, 2$), of a matrix that describes the galaxy's 3-dimensional mass distribution. The simplest choice is the tensor of the quadrupole moments of the mass distribution[1]

---

[1] As noted elsewhere, the mass distribution tensor is often referred to as the moment of inertia tensor,

(see e.g. Davis et al., 1985; Cole and Lacey, 1996; Bett, 2012), defined as:

$$\mathcal{M}_{ij} = \frac{\sum_p m_p r_{p,i} r_{p,j}}{\sum_p m_p} , \tag{3.8}$$

where the sums run over all particles comprising the structure, i.e. with $r_p < 30\,\mathrm{pkpc}$, $r_{p,i}$ denotes the component i (with $i, j = 0, 1, 2$) of the coordinate vector of particle p, and m_p is the particle's mass. However, we opt to use an iterative form of the reduced inertia tensor (see e.g. Dubinski and Carlberg, 1991; Bett, 2012; Schneider et al., 2012). The use of an iterative scheme is advantageous in cases where the morphology of the object can deviate significantly from that of the initial particle selection, as is the case here for flattened galaxies. The reduced form of the tensor mitigates the influence of structural features in the outskirts of galaxies by down-weighting the contribution of particles farther from their centre, i.e. with larger ellipsoidal radius, $\tilde{r}_p$ (eq. 3.10):

$$\mathcal{M}^r_{ij} = \frac{\sum_p \frac{m_p}{\tilde{r}_p^2} r_{p,i} r_{p,j}}{\sum_p \frac{m_p}{\tilde{r}_p^2}} . \tag{3.9}$$

In the first iteration, all stellar particles comprising the galaxy (those within a spherical aperture of $r = 30\,\mathrm{pkpc}$) are considered, yielding an initial estimate of the axis lengths (a, b, c). Stellar particles enclosed by the ellipsoid of equal volume described by the axis ratios:

$$\tilde{r}_p^2 \equiv r_{p,a}^2 + \frac{r_{p,b}^2}{(b/a)^2} + \frac{r_{p,c}^2}{(c/a)^2} \leq \left(\frac{a^2}{bc} \right)^{2/3} (30\,\mathrm{pkpc})^2, \tag{3.10}$$

are then identified, where the quantities $r_{p,a}$, $r_{p,b}$ and $r_{p,c}$ are the distances projected along the directions defined by the eigenvectors calculated in the previous iteration, and the axis lengths are recomputed from this set. This process continues until the fractional change of both of the ratios c/a and b/a converges to < 1 percent. Such convergence is generally achieved within 8-10 iterations, and the resulting median lengths of the aperture's major axis for galaxies of $\epsilon \simeq (0.2, 0.5, 0.8)$ are $a = (34, 39, 50)\,\mathrm{pkpc}$

---

since the two share common eigenvectors.

(stellar component only).

3.3.2 Diversity of ellipsoidal shapes

Fig. 3.2 shows with contours the 2-dimensional probability distribution of our sample of central galaxies at $z = 0$ (see Section 2.3.3 for the description of our sample) in the space defined by the triaxiality, T, and flattening, ϵ, shape parameters (see equation 3.7). The galaxies are assigned to a grid with 20 cells in each dimension, and contours are drawn for levels corresponding to the 50th, 84th and 99th percentiles of the distribution. The galaxies were then rebinned to a coarse grid of 8×6 cells, and a galaxy within each cell was selected at random. Face-on and edge-on images of these galaxies, created using the techniques described by Trayford et al. (2015), were extracted from the EAGLE public database[2] (McAlpine et al., 2016) and are shown in the background of the plot to provide a visual impression of the morphology corresponding to particular values of the shape parameters (ϵ, T).

Oblate systems ($T \simeq 0$) are found towards the left-hand side of the figure, and prolate ($T \simeq 1$) to the right[3], while highly-flattened discs are found towards the top of the figure and vertically-extended galaxies at the bottom. The contours indicate that the region of the (ϵ, T) plane most populated by the galaxies satisfying our initial selection criteria is that of flattened, oblate ellipsoids. The sample spans the full range of both parameters, with high-T galaxies tending to be less flattened and hence significantly prolate. The median values of ϵ and T are 0.46 and 0.19, respectively. The plane features two 'zones of avoidance', firstly at (high-ϵ, high-T) which requires that the entire galaxy assume a bar-like configuration, and secondly at the very lowest flattening values ($\epsilon < 0.1$), which require that galaxies are almost perfectly spherical. The artificial thickness caused by the lack of resolution in modelling the cold and dense phase of the ISM as discussed in Section 2.3.1 results in the distribution being compressed against too high ellipticities.

---

[2]http://galaxy-catalogue.dur.ac.uk
[3]Ellipsoids with $T \simeq 0.5$ are purely triaxial.
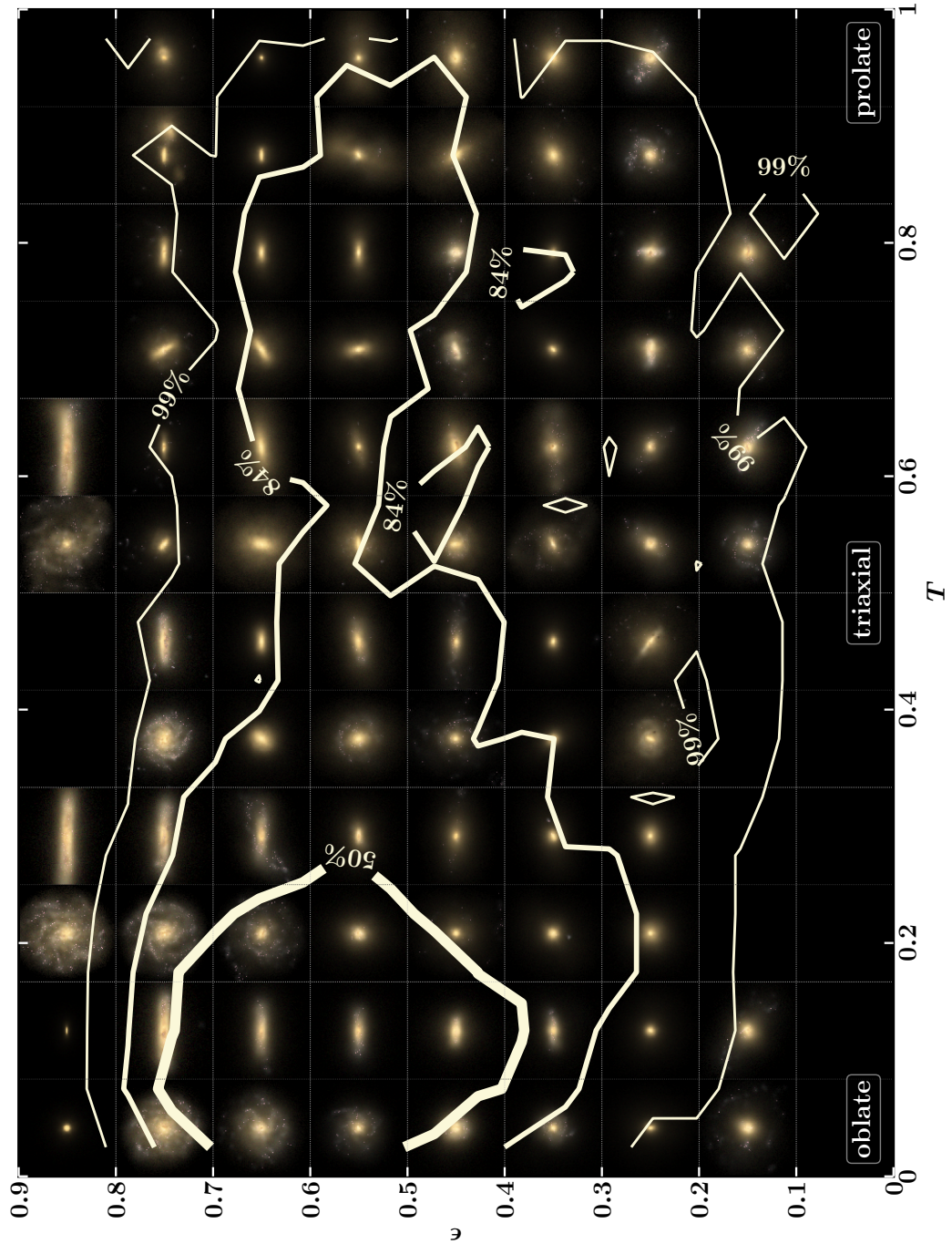
Figure 3.2: Two-dimensional histogram of the sample of 4155 central galaxies in the parameter space defined by the triaxiality, T, and flattening, ϵ, shape parameters (see eq. 3.7). The parameter space is sampled with cells of $\Delta T = 0.05$ and $\Delta \epsilon = 0.04$, and the overlaid contours correspond to the 50th, 84th and 99th percentiles of the distribution. The background is comprised of pairs of face-on and edge-on images of randomly-selected galaxies, $60\,\text{pkpc}$ on a side, drawn from the corresponding region of the parameter space to provide a visual impression of the morphology defined by the corresponding shape parameters. The most common configuration is a flattened, oblate ellipsoid, but galaxies span the majority of the available parameter space.

The oblate galaxies exhibit axisymmetry about the minor axis, while prolate systems are characterised by an intermediate axis that is significantly shorter than their major axis, and thus resemble cigars. We note that the face-on and edge-on orientations of the galaxy images were defined relative to the axis of rotation, rather than the structural minor axis; the two axes tend to be near-parallel in relaxed oblate systems but are often mis-aligned in prolate systems, the majority of which rotate about the major rather than minor axis (consistent with the observational findings of Krajnović et al., 2018). As such, the images of prolate systems can appear poorly aligned. The images of several prolate systems also show evidence of tidal disturbance and/or merger remnants, suggesting that prolate structure may be induced by interactions with neighboring galaxies.

Inspection of Fig. 3.2 also highlights a qualitative trend: star-forming galaxies, which are identifiable via blue, and typically extended, components in the images, are found preferentially in the (high-ϵ, low-T) regime, characteristic of discs. Conversely, red quiescent galaxies are preferentially located the low-ϵ regime. However, we note that the images of galaxies in the prolate regime exhibit blue, often asymmetric, structures, indicating that the interactions with neighbouring galaxies that induce prolate structure also induce star formation. Trayford et al. (2016) show that such interactions can enable red galaxies to temporarily "rejuvenate", and move from the red sequence back to the blue cloud (see also e.g. Robertson et al., 2006). In Section 3.5, we explore the consequences of this complexity in the (ϵ, T) plane in more detail.

3.4 Measuring dynamics in simulations

While morphological measurements of real galaxies can be achieved with a straightforward photometric approach, kinematics measurements require spectroscopic techniques for obtaining velocities via the Doppler shift. Also, while for the former measurements, CCD cameras alone could provide the necessary data, detailed kinematic measurements need more sophisticated technologies such as the recent Integral Field Unit (IFU) designs. These effectively combine independent spectrometers onto a ma-

trix of receptors, and can be used to create high-resolution velocity maps of galaxies. Recent years have seen the advent of panoramic surveys using IFUs, including the surveys SAURON (de Zeeuw et al., 2002), ATLAS^{3D} (Cappellari et al., 2011), SAMI (Croom et al., 2012), CALIFA (Sánchez et al., 2012), KROSS (Stott et al., 2016), MASSIVE (Ma et al., 2014), MaNGA (Bundy et al., 2015) and KMOS^{3D} (Wisnioski et al., 2015). These surveys approach the stellar medium in a similar modelling method to our theoretical framework from Section 3.2 by mapping streaming and random motions separately (respectively with the Doppler shift peaks and widths). Our intention is thus to use a descriptor adopting the same approach to conform with our theoretical framework, however many methods in use in the simulation communities must be considered. We review in detail each of those methods in Section 3.4.1, and present a comparative analysis in Section 3.4.2.

3.4.1 Characterising galaxy kinematics

Several diagnostic quantities are frequently used to characterise the kinematic properties of simulated galaxies. We briefly describe five of the most commonly-adopted diagnostics below, and assess the consistency between them in Section 3.4.2. In all cases, coordinates are computed in the frame centered on the galaxy's potential minimum, and velocities relative to the mean velocity of star particles within $30\,\mathrm{pkpc}$ of this centre. Unlike the calculation of the shape parameters, for which we consider particles within an iteratively-defined ellipsoidal aperture, the particle-based kinematic diagnostics described here are computed using stellar particles within a spherical aperture of $r = 30\,\mathrm{pkpc}$, for consistency with the existing literature.

Fraction of counter-rotating stars: The mass fraction of stars that are rotationally-supported (which can be considered the 'disc' mass fraction) is a simple and intuitive kinematic diagnostic. A popular means of estimating the disc fraction is to assume that the bulge component has no net angular momentum, and hence its mass can be estimated as twice the mass of stars that are counter-rotating with respect to the galaxy

(e.g. Crain et al., 2010; McCarthy et al., 2012; Clauwens et al., 2018). We therefore consider the disc-to-total mass fraction, D/T, to be the remainder when the bulge-to-total mass fraction, B/T is subtracted:

$$\frac{D}{T} = 1 - \frac{B}{T} = 1 - 2\frac{1}{M_\star} \sum_{i,L_{z,i}<0} m_i, \tag{3.11}$$

with $M_\star$ being the total stellar mass within $30\,\mathrm{pkpc}$, and where the sum is over all counter-rotating ($L_{z,i} < 0$) stellar particles within $30\,\mathrm{pkpc}$, m_i is the mass of each stellar particle and $L_{z,i}$ is the component of its angular momentum projected along the rotation axis, where the latter is the unit vector parallel to the total angular momentum vector of all stellar particles with $r < 30\,\mathrm{pkpc}$.

Rotational kinetic energy: the parameter κ_{co} specifies the fraction of a particle's total kinetic energy, K, that is invested in co-rotation $K_{\mathrm{co}}^{\mathrm{rot}}$ (Correa et al., 2017):

$$\kappa_{\mathrm{co}} = \frac{K_{\mathrm{co}}^{\mathrm{rot}}}{K} = \frac{1}{K} \sum_{i,L_{z,i}>0} \frac{1}{2} m_i \left(\frac{L_{z,i}}{m_i R_i}\right)^2, \tag{3.12}$$

where the sum is over all co-rotating ($L_{z,i} > 0$) stellar particles within $30\,\mathrm{pkpc}$, and R_i is the 2-dimensional radius in the plane normal to the rotation axis. The total kinetic energy in the centre of mass frame is $K = \sum_i \frac{1}{2} m_i v_i^2$, again summing over all stellar particles within $30\,\mathrm{pkpc}$.

Correa et al. (2017) used this diagnostic to characterise the kinematics of EAGLE galaxies, and found that dividing the population about a threshold in κ_{co} provides a means of separating the 'blue cloud' ($\kappa_{\mathrm{co}} > 0.4$) of disky star-forming galaxies from the 'red sequence' ($\kappa_{\mathrm{co}} < 0.4$) of spheroidal passive galaxies in the galaxy colour - stellar mass diagram. As those authors discussed, eq. 3.12 differs slightly from the usual definition of κ (Sales et al., 2010), insofar that only *corotating* particles contribute to the numerator. This results in a better measure of the contribution of rotation to the kinematics of the galaxy, since the majority of counter-rotating particles are found within the bulge component.

Spin parameter: we use the measurements of the mass-weighted stellar spin parameter, $\lambda_\star$, computed for EAGLE galaxies in a similar manner to the calculation of luminosity-weighted stellar spin parameters presented by Lagos et al. (2018). We create datacubes similar to those recovered by integral field spectroscopy, by projecting stellar particles onto a 2-dimensional grid to create a stellar mass-weighted velocity distribution for each pixel. We fit a Gaussian function to this distribution, defining the rotation velocity as that at which the Gaussian peaks, and the velocity dispersion as the square root of the variance, and arrive at the spin via:

$$\lambda_\star = \frac{\sum_i m_i r_i v_i}{\sum_i m_i r_i \sqrt{v_i^2 + \sigma_i^2}},$$

(3.13)

where m_i is the total stellar mass of the pixel i, v_i is its line-of-sight velocity, σ_i is its (1-dimensional) line-of-sight velocity dispersion, and r_i is the pixel's 2-dimensional galactocentric radius. The sum runs over pixels enclosed within the 2-dimensional projected stellar half-mass radius, $r_{\star,1/2}$. We compute spin measurements from maps in which the galaxies are oriented edge-on with respect to the spin vector. We note that this observationally-motivated definition of the spin parameter differs from the classical definition (see e.g. Bullock et al., 2001).

Orbital circularity: the parameter[4] ξ (see e.g. Abadi et al., 2003; Zavala et al., 2016) specifies the circularity of a particle's orbit by comparing its angular momentum to the value it would have if on a circular orbit with the same binding energy:

$$\xi_i = \frac{j_{\mathrm{z},i}}{j_{\mathrm{circ}}(E_i)},$$

(3.14)

where $j_{\mathrm{z},i}$ is the particle specific angular momentum projected along the rotation axis, and $j_{\mathrm{circ}}(E_i)$ is the specific angular momentum corresponding to a circular orbit with the same binding energy E_i. We estimate the latter as the maximum value of j_{z} for all

---

[4]We use the symbol ξ to denote the orbital circularity rather than the more commonly adopted ϵ to avoid confusion with the flattening parameter, ϵ, defined in Section 3.3.1.

stellar particles within $30\,\mathrm{pkpc}$ and $E < E_i$. Positive (negative) values of ξ correspond to co-rotation (counter-rotation).

An advantage of this method is that it can be used to assign particles to bulge and disc components, thus enabling a kinematically-defined structural decomposition. However, to enable a simple comparison with other kinematic diagnostics, we assign to each galaxy the median of the ξ values, $\overline{\xi}$, exhibited by star particles within $30\,\mathrm{pkpc}$ of the galaxy centre.

Ratio of rotation and dispersion velocities: the ratio of rotation and dispersion velocities is often used as a kinematical diagnostic since, as noted in the discussion of the spin parameter, both the rotation velocity and the velocity dispersion can be estimated from spectroscopic observations of galaxies (van de Sande et al., 2017). We adopt a cylindrical coordinate frame (r,z,θ), with the z-axis parallel to the total angular momentum of stellar particles within $30\,\mathrm{pkpc}$ and the azimuthal angle increasing in the direction of net rotation, and equate the rotation velocity of each galaxy, v_{rot}, to the absolute value of the 'mass-weighted median' of the tangential velocities, $v_{\theta,i}$, of its stellar particles. We compute mass-weighted medians of variables by identifying the value that equally divides the weights, i.e. we construct the cumulative distribution of weights from rank-ordered values of the variable in question, and interpolate to the value that corresponds to the 'half-weight' point. Since we weigh by particle masses, this is equivalently the 'half-mass value'.

To connect with observational measurements of the dispersion, which necessarily recover an estimate of the line-of-sight velocity dispersion, we seek the velocity dispersion in the 'disc plane', i.e. the plane normal to the z-axis, which we denote σ_0. The latter represents all remaining motion within the disc plane following the subtraction of the ordered co-rotational component (quantified by its corresponding kinetic energy $\frac{1}{2}M_\star v_{\mathrm{rot}}^2$), which can in principle comprise coherent streaming with respect to the centre-of-velocity frame, randomly-oriented elliptical orbits, or circular orbits that are mis-aligned with the disc, including counter-rotation. This component can be computed from the tensor virial equations: for an axisymmetric system of stellar particles

in a Cartesian frame and rotating about the z-axis, $2T_{xx} + \Pi_{xx} + W_{xx} = 0$, with $T_{xx} = T_{yy}$ and $T_{ij} = 0$ for $i \neq j$, and similarly for both Π and W. Here, W is the potential energy and T and Π are the contributions to the kinetic energy tensor, K, from ordered and disordered motion, respectively, such that $K_{ij} = T_{ij} + \frac{1}{2}\Pi_{ij}$. Binney and Tremaine (1987) show that $2T_{xx} = \frac{1}{2}M_\star v_{\mathrm{rot}}^2$ (assuming rotation about the z-axis is the only streaming motion) and $\Pi_{xx} = M_\star \sigma_0^2$.

Since we seek the velocity dispersion in the disc plane rather than along the line-of-sight, we exploit that the disc plane and vertical contributions are separable, i.e. $2T_{zz} + \Pi_{zz} + W_{zz} = 0$ also, and use

$$K - K_{zz} = \frac{1}{2}M_\star v_{\mathrm{rot}}^2 + M_\star \sigma_0^2, \tag{3.15}$$

which can be rearranged and solved for σ_0, as K and K_{zz} are the total and vertical kinetic energies of the system of stellar particles.

The disordered motion, Π, can also be separated into its components along the vertical axis ($M_\star \sigma_z^2$) and in the disc plane ($M_\star \sigma_0^2$); these are related via the parameter, δ, which describes the anisotropy of the galaxy's velocity dispersion:

$$\delta = 1 - \left(\frac{\sigma_z}{\sigma_0}\right)^2. \tag{3.16}$$

Values of $\delta > 0$ indicate that the velocity dispersion is primarily contributed by disordered motion in the disc plane, i.e. that defined by the intermediate and major axes, rather than disordered motion in the direction of the minor axis.

3.4.2 A brief comparison of kinematical diagnostics

We show in Fig. 3.3 the kinematical properties of EAGLE galaxies, as characterised by the diagnostics presented in Section 3.4.1. From top to bottom, these are: the disc-to-total stellar mass ratio, D/T; the kinetic energy in co-rotation, κ_{co}; the stellar mass-weighted spin parameter, $\lambda_\star$; and the median orbital circularity, $\bar{\xi}$. These quantities
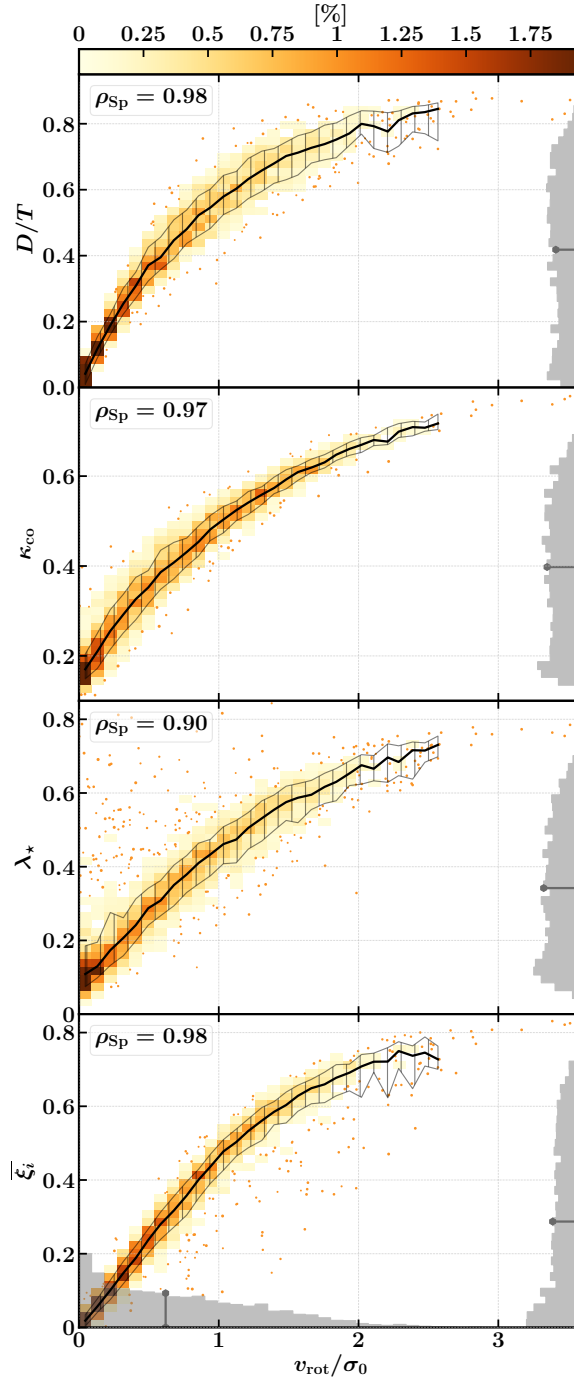
Figure 3.3: The relationship between v_{rot}/σ_0 and other kinematic diagnostics commonly used to characterise simulated galaxies, from top to bottom: D/T, κ_{co}, $\lambda_\star$ and $\overline{\xi_i}$. The panels show the 2-dimensional histogram of the 4155 galaxies in our sample, with the parameter space sampled by 40 cells in each dimension. Cells sampled by at least 3 galaxies are coloured to show their contribution to the distribution as a percentage of the total represented sample; galaxies associated with poorly-sampled cells are drawn individually. Overplotted lines show the binned median and 1σ (16th-84th) percentile scatter of the dependent variables. The 1-dimensional distributions in each variable are shown as grey-scale linear histograms, with the medians of these denoted by overlaid signposts. The four dependent variables each correlate strongly with v_{rot}/σ_0, having Spearman rank-order coefficients, ρ_{Sp}, of 0.98 (D/T), 0.97 (κ_{co}), 0.90 ($\lambda_\star$) and 0.98 ($\overline{\xi_i}$).

are shown as a function of the ratio of rotation and dispersion velocities, $v_{\rm rot}/\sigma_0$. The panels show the distribution of the 4155 galaxies of our sample as a 2-dimensional probability distribution function, with 40 cells in each dimension. Only cells sampled by at least 3 galaxies are coloured; galaxies associated with poorly-sampled cells are drawn individually. The overplotted lines show the binned median and 1σ (16th-84th percentile) scatter of the dependent variables. The 1-dimensional distributions in each variable are shown via the grey-scale linear histograms. The median values of D/T, $\kappa_{\rm co}$, $\lambda_\star$, $\overline{\xi}$ and $v_{\rm rot}/\sigma_0$, denoted by signposts on the grey-scale histograms, are 0.42, 0.40, 0.34, 0.27 and 0.62, respectively.

Reassuringly, there is a strong positive correlation between each of D/T, $\kappa_{\rm co}$, $\lambda_\star$ and $\overline{\xi}$, plotted as dependent variables, and $v_{\rm rot}/\sigma_0$. Since the correlations are not linear for all values of $v_{\rm rot}/\sigma_0$, we quantify their strength with the Spearman rank-order coefficient, $\rho_{\rm Sp}$, the values of which are unsurprisingly high: 0.98 for D/T, 0.97 for $\kappa_{\rm co}$, 0.90 for $\lambda_\star$, and 0.98 for $\overline{\xi}$. The scatter at fixed $v_{\rm rot}/\sigma_0$ is greatest for $\lambda_\star$, highlighting the intrinsic uncertainty associated with the recovery of kinematic diagnostics from surface-brightness-limited observations. In contrast, D/T, $\kappa_{\rm co}$ and $\overline{\xi_i}$ all scale nearly linearly with $v_{\rm rot}/\sigma_0$ in the regime $v_{\rm rot}/\sigma_0 \lesssim 1$, and $\kappa_{\rm co}$ in particular exhibits relatively little scatter at fixed $v_{\rm rot}/\sigma_0$.

We conclude from this brief examination that the five kinematical diagnostics are broadly consistent and can in general be used interchangeably. Following the suggestion of Correa et al. (2017) that division of the EAGLE population about a threshold of $\kappa_{\rm co} = 0.4$ separates the star-forming and passive galaxy populations (which we show later in Fig. 3.4), we infer that a similar outcome can be achieved by division about a threshold of $v_{\rm rot}/\sigma_0 \simeq 0.7$, which corresponds to $D/T \simeq 0.45$, $\lambda_\star \simeq 0.35$ or $\overline{\xi_i} \simeq 0.3$. Hereafter, we use $v_{\rm rot}/\sigma_0$ to characterise the internal kinematics of EAGLE galaxies; the main advantages being that it is derived using the same framework with which we compute the velocity dispersion anisotropy, δ, and that it is analogous to observational measurements derived from spectroscopy.

3.5 Correspondence with the colour-stellar mass relation

We now turn to a quantitative examination of the relationship between the morphology and kinematics of galaxies, and their location in the colour-stellar mass plane. As detailed in Section 2.3.3, our sample only includes galaxies with stellar masses above $10^{9.5}$ $M_\odot$. As shown by Schaye et al. (2015), galaxies below this threshold tend to be unreliably quantitatively quiescent due to poor star forming gas resolution. The panels of Fig. 3.4 show with contours the 2-dimensional histogram of the simulated galaxies in the $(u^\star - r^\star)$ colour - stellar mass plane, where the superscript * denotes intrinsic colours, i.e. rest-frame and dust-free. In all panels, galaxies are binned onto a grid with 20 cells in each dimension. As per the images shown in Fig. 3.2, broadband magnitudes were retrieved from the EAGLE public database, having been computed with the techniques described by Trayford et al. (2015), who showed that the $(g - r)$ colours of the EAGLE galaxy population are consistent with the dust-corrected colours of observed galaxies.

The dashed line overlaid on each panel corresponds to the definition of the 'green valley' proposed by Schawinski et al. (2014), $(u^\star - r^\star) = 0.25 \log_{10}(M_\star/M_\odot) - 0.495$, which separates the blue cloud of star-forming galaxies from the red sequence of passive galaxies. Trayford et al. (2015, 2017) show that EAGLE's galaxy population naturally divides into these two populations, and we see here that, despite the omission of satellite galaxies from our sample, which comprise a significant fraction of the low-mass regime of the present-day red sequence, colour bimodality is still clearly visible in the contours.

In the upper left-hand panel of Fig. 3.4, well-sampled cells are coloured by the median value of the flattening parameter, ϵ, of the galaxies within the cell. This plot is therefore analogous to the colour-stellar mass diagram shown by Correa et al. (2017, their Fig. 3), in which the galaxies are coloured by κ_{co}. As noted in Section 3.4.2, those authors show that the blue cloud and red sequence can be reasonably well separated by a simple
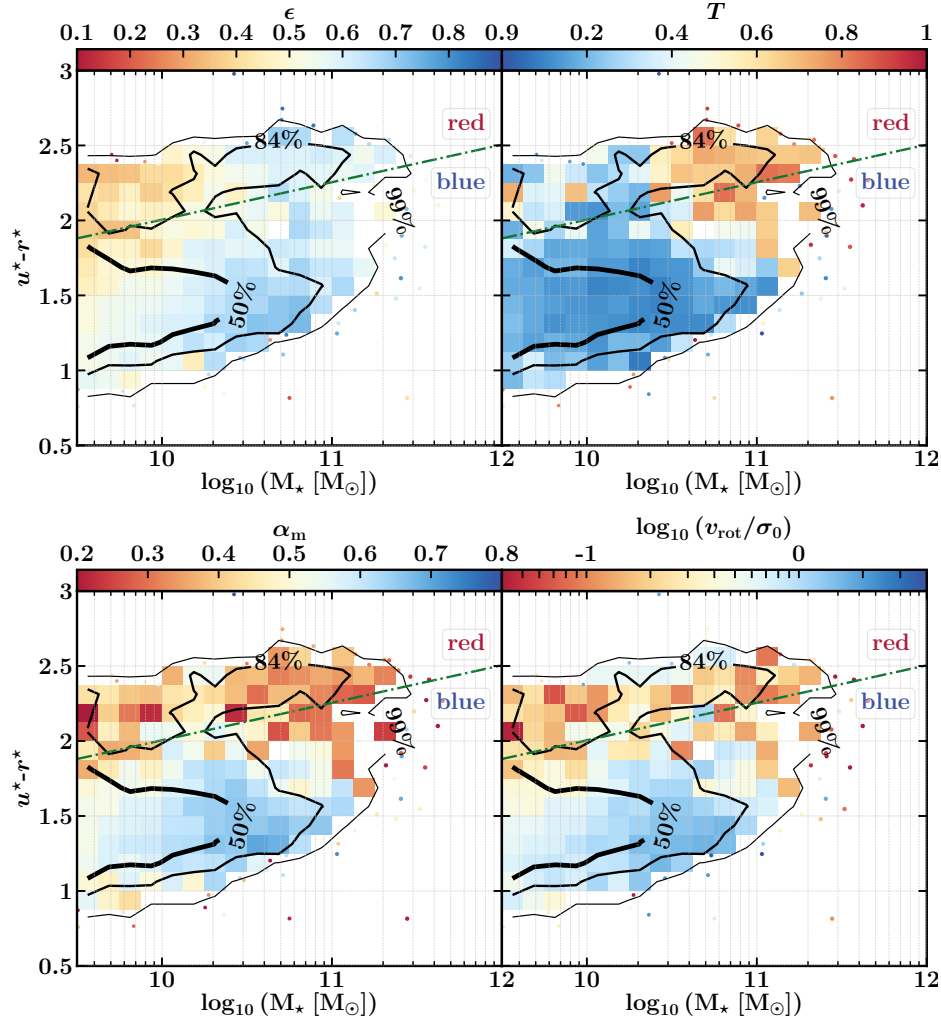
Figure 3.4: The $(u^\star - r^\star) - M_\star$ relation at present day, using our sample of 4155 well-sampled central galaxies. The parameter space is sampled with 20 cells in each dimension, and the overlaid contours correspond to the 50th, 84th and 99th percentiles of the distribution. In the regime where cells are sampled by fewer than 3 galaxies, galaxies are represented individually by points. The dot-dashed line corresponds to the definition of the 'green valley' advocated by Schawinski et al. (2014), separating the 'red sequence' from the 'blue cloud'. Cells and points are coloured by the median flattening, ϵ, of the galaxies in the upper left-hand panel, the median triaxiality, T, of galaxies in the upper right-hand panel, by the median of the parameter α_{m} (see main text) in the lower left-hand panel, and by the median rotation-to-dispersion velocity, v_{rot}/σ_0, in the lower right-hand panel. The colouring shows that the blue cloud is preferentially comprised of flattened, rotationally-supported galaxies with low triaxiality, whilst red sequence galaxies tend to be spheroidal or prolate, and exhibit significant dispersion support. The two populations can be differentiated with similar efficacy using thresholds of $\alpha_{\text{m}} \simeq 0.5$ or $v_{\text{rot}}/\sigma_0 \simeq 0.7$.

threshold in κ_{co}. As might also be inferred from inspection of Fig. 3.2, we find here that a simple threshold in ϵ does not enable such a clean separation; whilst the blue cloud is dominated by flattened galaxies $\epsilon \gtrsim 0.5$, only the low-mass end of the red sequence is dominated by spheroidal galaxies. Inspection of the upper right-hand panel of Fig. 3.4, in which the cells are coloured by the median value of the triaxiality parameter, T, shows that the flattened galaxies populating the high-mass end of the red sequence are prolate ($T \simeq 1$) rather than disc-dominated systems. An increasing prolate fraction with increasing stellar mass was also reported by Li et al. (2018) based on an analysis of the morphology of galaxies in the Illustris simulations, and recent observations with the MUSE integral field spectrograph of massive galaxies corroborate this prediction (Krajnović et al., 2018). Conversely, we find that the blue cloud is overwhelmingly dominated by flattened systems with very low values of the triaxiality parameter, i.e. disky galaxies.

Since neither ϵ nor T alone affords a simple means of separating the blue cloud from the red sequence, we construct a new morphological diagnostic that combines both shape parameters, $\alpha_{\mathrm{m}} = (\epsilon^2 + 1 - T)/2$. This heuristic approach allows us to access a new single morphological parameter with a similar range to that of the ellipticity and triaxiality parameters. While its specific form was not thought from a physical basis[5], it may be used for its characterization of the morphological parameter space. Notably, this diagnostic separates by construction spheres and prolate spheroids, characteristic of the morphology of early-type galaxies, from the oblate spheroids that characterise the morphology of late-type galaxies. Cells are coloured by this quantity in the lower left-hand panel of Fig. 3.4, showing that a simple threshold of $\alpha_{\mathrm{m}} \simeq 0.5$, does a reasonable job of distinguishing galaxies of the blue cloud from those of the red sequence.

In the lower right-hand panel of Fig. 3.4, cells are coloured by the median $v_{\mathrm{rot}}/\sigma_0$ of the galaxies in each pixel. Visual inspection shows that the blue cloud is dominated by rotationally-supported galaxies, whilst the galaxies comprising the red sequence are generally dispersion supported. As might be expected when considering the correspondence between κ_{co} and $v_{\mathrm{rot}}/\sigma_0$ discussed in Section 3.4.2, a simple threshold

---

[5]although further work could help investigating a potential physical interpretation

in the latter (e.g. $v_{\rm rot}/\sigma_0 \simeq 0.7$) therefore differentiates the blue cloud from the red sequence with a similar efficacy to the $\kappa_{\rm co} = 0.4$ threshold advocated by Correa et al. (2017). Comparison of the lower two panels of Fig. 3.4 thus shows that the two populations can be differentiated with similar efficacy using morphological or kinematical diagnostics, but only using morphology if one is able to measure both the flattening and triaxiality of the galaxies. In general this is not the case for observational studies, making the spectroscopically-accessible $v_{\rm rot}/\sigma_0$ diagnostic a particularly effective means of differentiation. For analyses of simulations, the $\kappa_{\rm co}$ diagnostic is attractive, since it requires the calculation of a single quantity that is simple to interpret and which takes values in the range of [0,1].

3.6 Summary and discussions

After introducing some necessary theoretical elements, we have presented diagnostics used for characterising the morphology and internal kinematics of the stellar component of galaxies in the EAGLE suite of cosmological simulations. We then investigated their diversity and relation with galaxy colours. Our results can be summarized as follows:

1. Modelling EAGLE galaxies as ellipsoids described by the flattening (ϵ) and triaxiality (T) parameters (eq. 3.7) provides a quantitative description of their stellar morphology that is consistent with their qualitative visual appearance. The sample exhibits a diversity of morphologies, including spheroidal, oblate and prolate galaxies. The majority of the sample are oblate ($T \lesssim 0.3$) and flattened ($\epsilon \gtrsim 0.4$), characteristics of "disky" galaxies (Fig. 3.2).

2. Comparison of five diagnostic quantities frequently used to describe the internal kinematics of the stellar particles comprising simulated galaxies, namely the disc-to-total stellar mass fraction, D/T, computed assuming the bulge mass is equal to twice the mass of counter-rotating stellar particles; the fraction of kinetic energy in ordered co-rotation, $\kappa_{\rm co}$; the mass-weighted spin parameter, $\lambda_\star$;

the median orbital ellipticity, $\overline{\xi}_i$; and the ratio of the rotational and dispersion velocities, $v_{\mathrm{rot}}/\sigma_0$, reveals that they are strongly correlated. This indicates that such descriptors can in general be used interchangeably (Fig. 3.3).

3. The distribution of the shape parameters in the $(u^\star\text{-}r^\star)$ colour - stellar mass plane shows that star-forming central galaxies (comprising the blue cloud) are typically flattened, oblate (rotation-supported) galaxies. The red sequence (of central galaxies) is comprised primarily of spheroidal galaxies at low masses, whilst the more massive regime is dominated by flattened, prolate (dispersion-supported) galaxies. Since both the blue cloud and the red sequence are populated by flattened galaxies, a threshold in ϵ does not separate the two populations as effectively as as a kinematic criterion such as the $\kappa_{\mathrm{co}} = 0.4$ threshold advocated by Correa et al. (2017) (Fig. 3.4). We show that a diagnostic constructed from both shape parameters, $\alpha = (\epsilon^2 + 1 - T)/2$, designed to separate spheres and prolate spheroids from oblate spheroids, is able to separate the two populations with similar efficacy to a kinematic criterion. However we note that T is not readily accessible from observations, making kinematical diagnostics such as $v_{\mathrm{rot}}/\sigma_0$ preferable.

It had long been assumed that morphologies and internal kinematics tend to correlate, with late-type galaxies being more rotation-supported and early-type galaxies being more dispersion-supported. However, the relation between these properties and colours reveals a disconnection: structural and dynamic properties represent differently the red sequence and blue cloud. Accordingly, the next Chapter focuses on the correlation between morphologies and internal kinematics.

Chapter 4

Stellar morpho-kinematics and halo structure

4.1 Introduction

The relatively recent advent of large surveys conducted with wide-field integral field spectrographs has enabled the compilation of large and diverse samples of galaxies in the local Universe with well-characterised morphological and kinematical properties (e.g. de Zeeuw et al., 2002; Cappellari et al., 2011; Croom et al., 2012; Sánchez et al., 2012; Ma et al., 2014; Bundy et al., 2015). One of the prime outcomes of these endeavours is the demonstration that there is a not a simple mapping between galaxy morphology and internal kinematics, particularly within the family of early-type galaxies for which the kinematics are not generally dominated by rotation (for a recent review see Cappellari, 2016). Early-type galaxies with similar morphologies are found to exhibit a diversity of kinematic properties, indicating that kinematic diagnostics may yield a more fundamental means of classifying galaxies than purely morphological descriptions (e.g. Emsellem et al., 2007; Krajnović et al., 2013; Cortese et al., 2016; Graham et al., 2018). Similarly, Foster et al. (2017) recently showed that the morphologies of kinematically-selected galaxies are clearly correlated with the degree of rotational support, but with a large degree of scatter. As seen in Section 3.2, analytic modelling

of galaxies using the tensor virial theorem indicates that this diversity stems from differing degrees of anisotropy in the stellar velocity dispersion (e.g. Binney, 1976), but the origin of the diversity in the inferred anisotropy remains unclear.

In this Chapter, we extend the analysis of Chapter 3 with an examination of the relationship between the morphology and internal kinematics of galaxies formed in the EAGLE simulations. The simulation also enables us to investigate the origin of scatter about the relation between the two properties. We develop this relationship in Section 4.2 in which we first study its connection with stellar mass. Then we investigate further the origin of its scatter by isolating two subsamples: one made of prolate galaxies (Section 4.2.2) and the other composed of oblate and spheroidal galaxies (Section 4.2.3). We notably reveal in the latter subsample the connection with the dispersion anisotropy, to develop further in Section 4.3 its relation with dark matter morphology. We focus first in Section 4.3.1 on the relation between dark matter morphologies and stellar morpho-kinematics, to conclude with the relation with stellar dispersion anisotropy in section 4.3.2. We summarise and discuss our findings in Section 4.4.

4.2 Relationship between morphology and kinematics

We now turn to the correspondence between the morphology and kinematics of EAGLE galaxies from Ref-L100N1504. In Fig. 4.1, we show how galaxies populate the $v_{\rm rot}/\sigma_0 - \epsilon$ plane with contours corresponding to the $50^{\rm th}$, $84^{\rm th}$ and $99{\rm th}$ percentiles of the distribution. The background colouring denotes the characteristic stellar mass of galaxies at each location in $v_{\rm rot}/\sigma_0 - \epsilon$ space. van de Sande et al. (2018a) recently demonstrated that EAGLE galaxies selected to mimic those targeted by the SAMI survey populate this parameter space in a similar fashion to the observed sample. The upper panel of Fig. 4.1 shows the distribution of all 4155 central galaxies comprising our overall sample, whilst the lower panel shows the distribution for the sub-set of 2703 galaxies that are spheroidal ($\epsilon < 0.3$), or are oblate ($T < 1/3$) and have their angular momentum axis aligned with their structural minor axis to within 10 degrees. As might be inferred from Fig. 3.4, massive galaxies (i.e. $M_\star \gtrsim 10^{10.5}\,{\rm M}_\odot$) tend to populate the
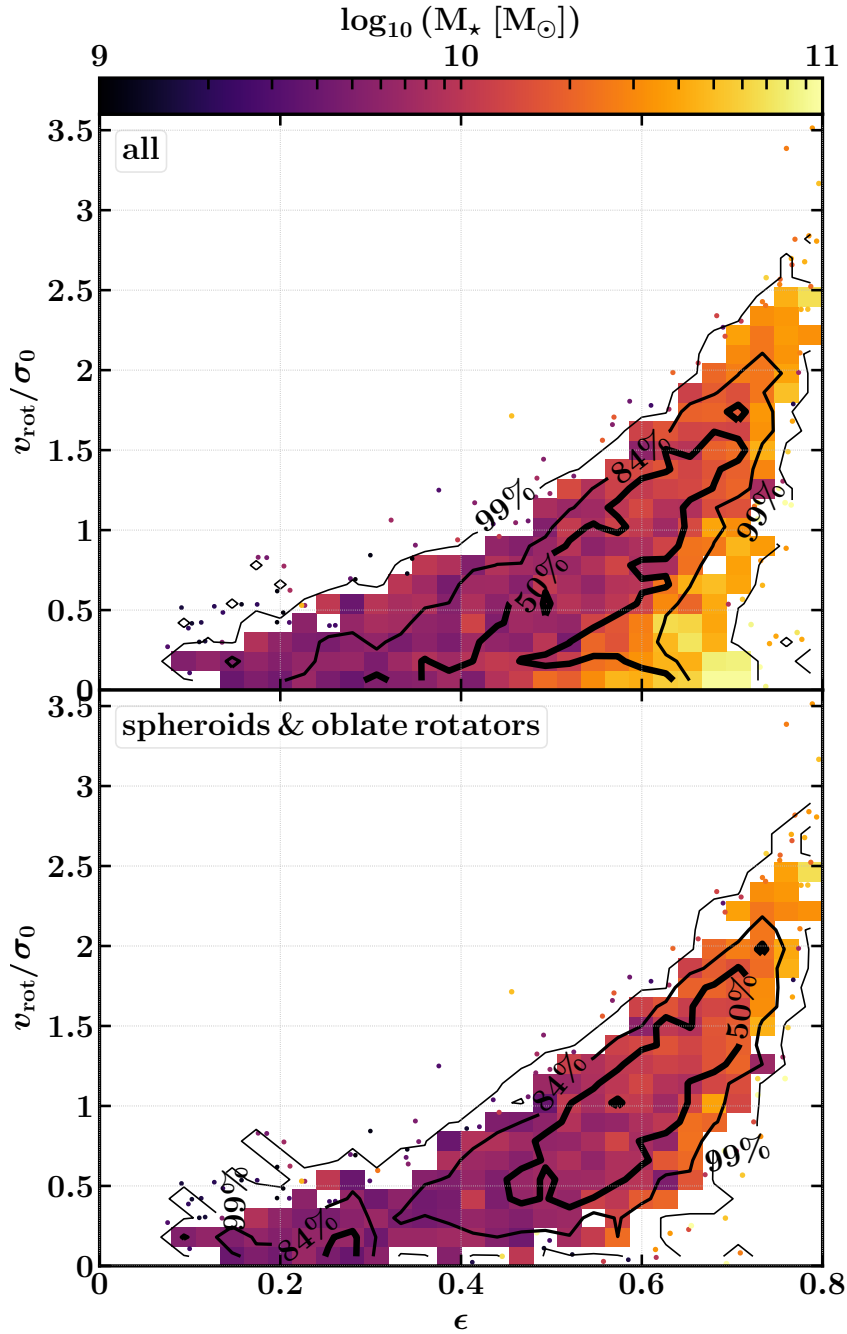
Figure 4.1: Two-dimensional probability distribution function in the $v_{\rm rot}/\sigma_0$ and flattening, ϵ, plane shown as contours corresponding to the $50^{\rm th}$, $84^{\rm th}$ and 99th percentiles of the distribution, drawn on a 30×30 grid. Well-sampled cells are colour-coded by their median stellar masses, while galaxies associated with cells sampled by fewer than 3 galaxies are drawn and coloured individually. The upper panel shows the full sample of 4155 galaxies, the lower panel shows the sub-set of 2703 galaxies that are spheroidal ($\epsilon < 0.3$), or oblate ($T < 1/3$) and have their angular momentum axis aligned with their structural minor axis to within 10 degrees. Excision of the prolate and mis-aligned systems primarily eliminates a population of dispersion-supported ($v_{\rm rot}/\sigma_0 \simeq 0$) galaxies with diverse morphologies. The remaining sample exhibits a strong correlation between the morphological and kinematic diagnostics, but there is significant scatter in ϵ at fixed $v_{\rm rot}/\sigma_0$.

high-ϵ regime, but exhibit a diverse range of $v_{\rm rot}/\sigma_0$ values since they can be rotating discs or prolate spheroids with significant dispersion support. The excision of prolate galaxies, and a small number of systems whose morphology and kinematics have been influenced significantly by encounters with neighbours or recently-merged satellites, therefore preferentially eliminates a population of dispersion-supported ($v_{\rm rot}/\sigma_0 \simeq 0$) galaxies with diverse morphologies.

The remaining sample exhibits a strong correlation between the morphological and kinematic diagnostics (Spearman rank-order coefficient of $\rho_{\rm Sp} = 0.72$), but with significant scatter in ϵ at fixed $v_{\rm rot}/\sigma_0$. It is possible to identify galaxies with $v_{\rm rot}/\sigma_0 \simeq 1$ and flattening parameters as diverse as $\epsilon \simeq 0.3 - 0.8$. Similarly, flattened galaxies with $\epsilon \simeq 0.7$ can exhibit rotation-to-dispersion velocity ratios between $v_{\rm rot}/\sigma_0 \simeq 0.5$ and $v_{\rm rot}/\sigma_0 \simeq 3.5$. It is therefore clear that morphological and kinematical diagnostics are not trivially interchangeable, indicating that the morphology of a galaxy is significantly influenced not only by $v_{\rm rot}/\sigma_0$, but also by at least one other property. In this respect the simulations are in qualitative agreement with the findings of surveys conducted with panoramic integral field spectrographs that show significant scatter in the $v_{\rm rot}/\sigma_0$ - ϵ diagram (Emsellem et al., 2011; Fogarty et al., 2014; Cappellari, 2016; van de Sande et al., 2017; Graham et al., 2018).

4.2.1 Numerical convergence test

Here we briefly assess the convergence of the kinematics (using the rotation-to-dispersion velocity ratio, $v_{\rm rot}/\sigma_0$) and morphology (using the flattening, ϵ) of EAGLE galaxies with respect to resolution. We consider the 'weak convergence' test[1], comparing the properties of galaxies formed by the Reference model at standard resolution with those of galaxies formed by the Recalibrated model at high-resolution.

In Fig. 4.2 we show as a 2-dimensional histogram in $v_{\rm rot}/\sigma_0 - \epsilon$ space the distribution of the sub-set of 2703 galaxies from our main sample in the Ref-L100N1504 simulation that are i) spheroidal ($\epsilon < 0.3$) or ii) oblate ($T < 1/3$) galaxies and have their

---

[1]The concept of strong and weak convergence testing was introduced by Schaye et al. (2015).
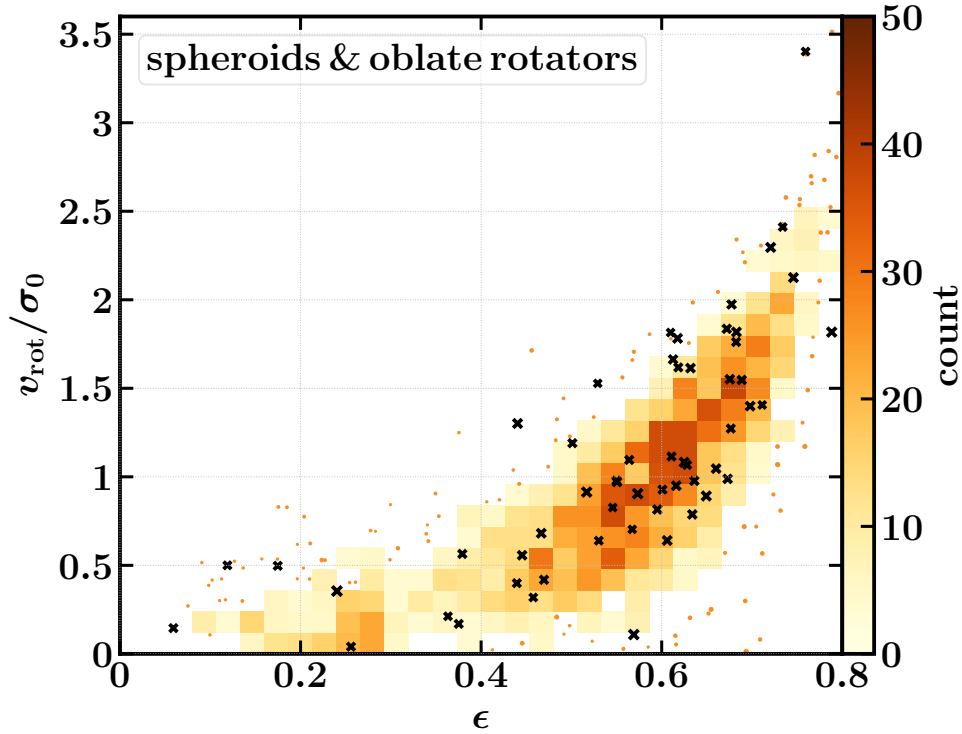
Figure 4.2: The relationship between $v_{\rm rot}/\sigma_0$ and flattening, ϵ, for central galaxies with $M_\star > 10^{9.5}\,{\rm M_\odot}$ and which are i) spheroidal ($\epsilon < 0.3$) or ii) oblate ($T < 1/3$) galaxies and have their morphological and rotational axes aligned to within 10 degrees. The 2-dimensional histogram and orange dots represent the 2703 galaxies of Ref-L100N1504 that satisfy these criteria (as per the bottom panel of Fig. 4.1), whilst black crosses denote the corresponding 57 galaxies from Recal-L025N0752. Visual inspection suggests that the weak convergence behaviour of $v_{\rm rot}/\sigma_0$ and ϵ is good, an impression corroborated by the two-sample Kolmogorov-Smirnoff test in each case.

morphological and rotational axes aligned to within 10 degrees. The overlaid crosses denote the 57 galaxies that satisfy the same selection criteria in the high-resolution Recal-L025N0752 simulation. Inspection of the figure suggests that the distributions of $v_{\rm rot}/\sigma_0$ and ϵ from the two simulations are similar. We obtain a quantitative measure of this similarity using the two-sample Kolmogorov-Smirnoff test, to assess the hypothesis that the values of $v_{\rm rot}/\sigma_0$ and ϵ for galaxies in the Ref-L100N1504 and Recal-L025N0752 simulations share similar distributions. In both cases the test indicates that this hypothesis cannot be rejected; for $v_{\rm rot}/\sigma_0$ we obtain ($D = 0.11$, $p = 0.23$) whilst for ϵ we obtain ($D = 0.11$, $p = 0.20$), where D is the Kolmogorov-Smirnoff statistic and p is the two-tailed probability value. These findings are unchanged if instead we compare Recal-L025N0752 to Ref-L025N0376, to control against box-size effects.

4.2.2 Prolate kinematically misaligned galaxies

Prolate galaxies constitute a minor component of our sample, but they are a significant fraction of the dispersion-supported region of the morphokinematic distribution, as shown by their excision from the latter. As they come in variously elongated configurations, they contribute significantly to the scatter at low rotation-support of this relationship. Recent observations have revealed the existence of such prolate galaxies exhibiting rotation around their major axis (e.g. Tsatsi et al., 2017). Our kinematic descriptors are defined from the angular momentum, the orientation of which may deviate from the morphological ellipsoidal axes, which can make their comparison inapplicable. We can study the relationship between our galaxies' morphological orientation and their stellar rotational orientation, for which we define a dimensionless rotational orientation parameter $\lfloor \vec{L} \rceil_{\|\vec{c}\|\equiv 0}^{\|\vec{a}\|\equiv 1}$:

$$\lfloor \vec{L} \rceil_{\|\vec{c}\|\equiv 0}^{\|\vec{a}\|\equiv 1} = \frac{1}{2} \left(\frac{\angle(\vec{c}, \vec{L})}{90°} + 1 - \frac{\angle(\vec{a}, \vec{L})}{90°} \right) \tag{4.1}$$

where $\angle(\vec{u}, \vec{v})$ represents the *geometric* measure of the angle between 2 arbitrary vectors $\vec{u}$ and $\vec{v}$. This *geometric* measure does not take consideration of the order of the vectors but always evaluate the positive measure below $180°$ that separates those vectors, contrary to the *algebraic* measure that can take the positive measure above $180°$ or the corresponding negative measure above $-180°$. Also, because $\vec{a}$ and $\vec{c}$ are eigenvectors, their orientation can be freely chosen so that both $\angle(\vec{a}, \vec{L})$ and $\angle(\vec{c}, \vec{L})$ are acute angles comprised between 0 and $90°$. With this specification, $\lfloor \vec{L} \rceil_{\|\vec{c}\|\equiv 0}^{\|\vec{a}\|\equiv 1}$ varies then between 0 and 1: it equals 0 if and only if $\angle(\vec{c}, \vec{L}) = 0°$ & $\angle(\vec{a}, \vec{L}) = 90°$ i.e. if the galaxy rotates around its minor axis (later referred as oblate rotation), and it equals 1 if and only if $\angle(\vec{c}, \vec{L}) = 90°$ & $\angle(\vec{a}, \vec{L}) = 0°$ i.e. if the galaxy rotates around its major axis (later referred as prolate rotation).

Figure 4.3 shows the relation between the rotational orientation parameter and the morphological 2-dimensional diversity of galaxies for our full sample of 4155 galaxies. Specifically, the colour-coding represents in bluer colours regions with a majority of
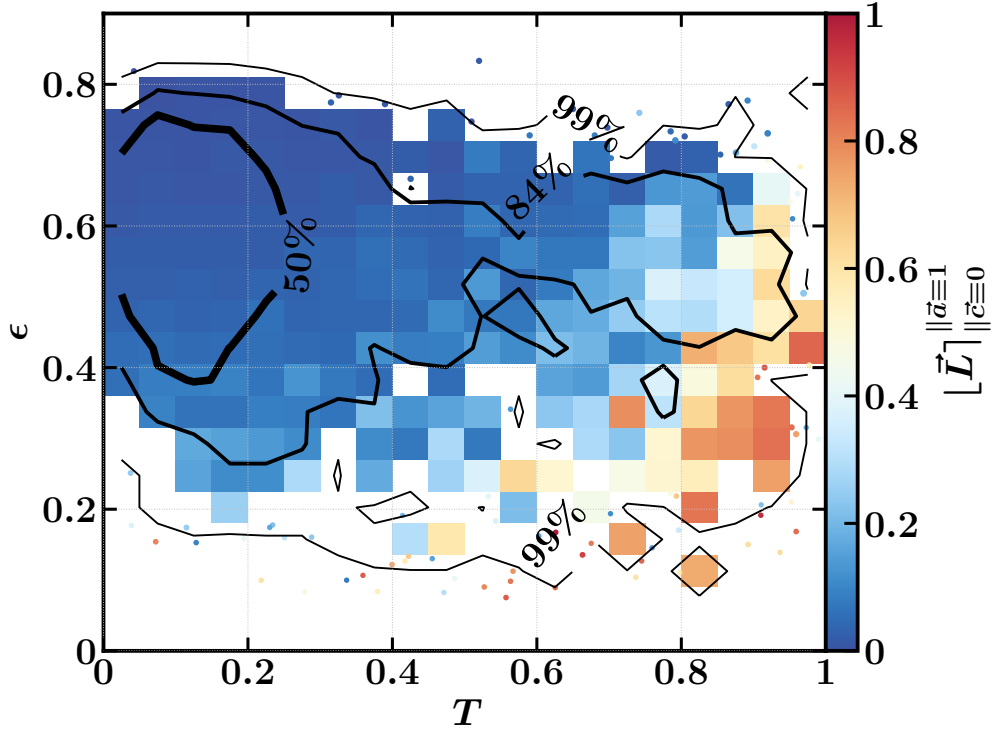
Figure 4.3: Relationship between the distribution shown in figure 3.2 and the rotational orientation parameter $\lfloor\vec{L}\rceil_{\|\vec{c}\equiv0}^{\|\vec{a}\equiv1}$. The parameter space is sampled as in figure 3.2, with a colour-coding reflecting the median rotational orientation parameter for well-sampled cells, while other galaxies are drawn and coloured individually. Contours illustrate the morphological distribution as shown in figure 3.2.

galaxies with oblate rotation while redder colours associate to prolate rotation. While a vast majority of our sample exhibit oblate rotation, the higher the triaxiality of a galaxy, the more its rotation turns to a prolate rotation. This implies that the EAGLE simulation is capable of forming prolate rotators, and as shown by Tsatsi et al. (2017), potentially via specific past merging configurations, which remain to be explored further in EAGLE.

4.2.3 Oblate rotators and spheroids

The morphology and kinematics of collisionless systems are linked via the tensor virial theorem. Its application to oblate, axisymmetric spheroids rotating about their short axis, modelled as collisionless gravitating systems, is discussed in detail by Binney (1978) and Binney and Tremaine (1987). They show that such bodies trace distinct
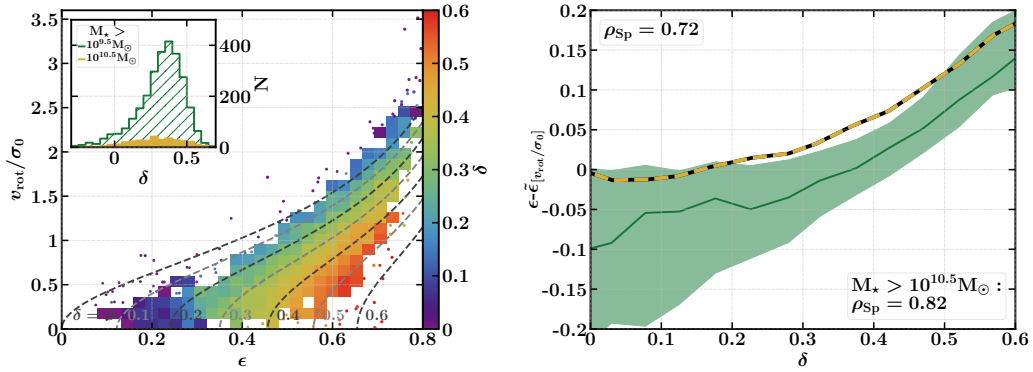
Figure 4.4: *Left:* The same sample of galaxies shown in the lower panel of Fig. 4.1, with colour coding of each cell denoting the median velocity dispersion anisotropy δ (eq. 3.16) of its associated galaxies. The alternately black and grey dashed curves represent as Figure 3.1 the $v_{\rm rot}/\sigma_0$ - ϵ relation expected for $\delta = 0.0 - 0.6$ in increments of 0.1, from application of the tensor virial theorem. The simulations reproduce the analytical predictions in both qualitative and quantitative senses, with increased flattening at fixed $v_{\rm rot}/\sigma_0$ clearly associated with increased anisotropy. The inset panel shows the histogram of anisotropy values realised by this sample (green hatching) and also separately for galaxies with $M_\star > 10^{10.5}\,{\rm M_\odot}$ (yellow). *Right:* the deviation of a galaxy's flattening, ϵ, from the median flattening for galaxies of similar $v_{\rm rot}/\sigma_0$, $\tilde{\epsilon}_{[v_{\rm rot}/\sigma_0]}$, as a function of δ. The solid line and shaded region denote the median and 1σ ($16^{\rm th}$-$84^{\rm th}$ percentile) scatter about it, respectively, in bins of $\Delta\delta = 0.05$. The correlation of these quantities has a Spearman rank-order coefficient of $\rho_{\rm Sp} = 0.72$. Similarly, the yellow dashed curve represents the median relationship for the high-mass end sub-population, showing a correlation with a Spearman rank-order coefficient of $\rho_{\rm Sp} = 0.82$.

paths in the $v_{\rm rot}/\sigma_0$ - ϵ plane, for fixed values of the velocity dispersion anisotropy, δ (see eq. 3.16), offering a potential explanation for the morphological diversity of galaxies at fixed $v_{\rm rot}/\sigma_0$.

In the left-hand panel of Fig. 4.4, we plot once again the $v_{\rm rot}/\sigma_0 - \epsilon$ distribution of the sub-sample of 2703 spheroidal and well-aligned oblate galaxies. Here, the colour coding denotes the median velocity dispersion anisotropy of galaxies associated with each cell that was shown in the bottom panel of Fig. 4.1. The overlaid dashed curves represent the $v_{\rm rot}/\sigma_0 - \epsilon$ relation expected from application of the tensor virial theorem to collisionless gravitating systems with $\delta = 0.1 - 0.6$, in increments of 0.1. We remind the reader that, as shown in Fig. 4.1, the high-ϵ regime is dominated by more-massive galaxies ($M_\star \gtrsim 10^{10.5}\,{\rm M_\odot}$), whilst the majority of the plane is sampled by galaxies with mass closer to our selection limit of $M_\star = 10^{9.5}\,{\rm M_\odot}$.

The main plot demonstrates that the analytic predictions are a good representation of

the behaviour of the simulated galaxies. At fixed $v_{\mathrm{rot}}/\sigma_0$, more anisotropic galaxies are clearly associated with a more flattened morphology; taking galaxies with $v_{\mathrm{rot}}/\sigma_0 \simeq 1$ as an example, those with $\epsilon \simeq 0.45$ exhibit a typical anisotropy of $\delta \simeq 0.2$, whilst the most-flattened examples, with $\epsilon \simeq 0.7$, exhibit $\delta \simeq 0.5$. The inset panel shows the histogram of anisotropy values realised by the sub-sample of 2703 (green hatching), and also those of the 329 galaxies from this sub-sample with $M_\star \gtrsim 10^{10.5}\,\mathrm{M_\odot}$ (yellow). For the main sub-sample, the distribution is broadly symmetric about a median of 0.34, albeit with a more extended tail to low (even negative) values. A small but significant fraction of galaxies in the sample ($\simeq 5$ percent), exhibit $\delta > 0.5$. The sub-set of high-mass galaxies spans a similar range in δ but exhibits a lower median value of 0.29.

To highlight the influence of δ on morphology more clearly, we compute $\tilde{\epsilon}_{[v_{\mathrm{rot}}/\sigma_0]}$, the median flattening parameter of galaxies in bins of fixed $v_{\mathrm{rot}}/\sigma_0$, and plot in the right-hand panel of Fig. 4.4, as a function of δ, the deviation of each galaxy's flattening parameter from this median, $\epsilon - \tilde{\epsilon}_{[v_{\mathrm{rot}}/\sigma_0]}$. The solid line and shaded region denote the median and 1σ ($16^{\mathrm{th}} - 84^{\mathrm{th}}$ percentile) scatter of this deviation in bins of $\Delta\delta = 0.05$. The two quantities are strongly correlated, with a Spearman rank-order coefficient of $\rho_{\mathrm{Sp}} = 0.72$. The yellow dashed curve represents the trend of the sub-set of high-mass galaxies; since these galaxies are largely confined to high-ϵ values, we cannot recompute $\tilde{\epsilon}_{[v_{\mathrm{rot}}/\sigma_0]}$ from this sub-set, and use that of the main sample. As such the median $\epsilon - \tilde{\epsilon}_{[v_{\mathrm{rot}}/\sigma_0]}$ at fixed δ for this sub-set is necessarily elevated. The morphologies of the high-mass sub-set are even more strongly correlated with the anisotropy, with a Spearman rank-order coefficient of $\rho_{\mathrm{Sp}} = 0.82$. The physical interpretation one may therefore draw is that the flattening of EAGLE galaxies, particularly those with low and intermediate levels of rotation support (i.e. $v_{\mathrm{rot}}/\sigma_0 < 1$), can be influenced significantly by the anisotropy of the stellar velocity dispersion, with some galaxies exhibiting anisotropy values as high as $\delta \simeq 0.5$.

4.3 The origin of the velocity anisotropy

The simulations enable us to examine the origin of the velocity anisotropy that, as discussed in the previous section, can have a significant influence on galaxy morphology. Since the equilibrium orbits of stellar particles are strongly influenced by the structure of the gravitational potential, we focus on the relationship between the velocity anisotropy of galaxies and the morphology of their dark matter haloes, since the latter is a proxy for the structure of the potential.

In analogy with the morphology of galaxies, we quantify the halo morphology via the flattening parameter, ϵ_{dm}, in this case applying the iterative reduced tensor to the distribution of dark matter particles. Since we are concerned with the structure of the potential in the same region for which we have 'tracers' of the potential (i.e. stellar particles), we begin iterating the tensor on the set of dark matter particles located within the same $r = 30$ pkpc spherical aperture, centred on the galaxy's potential minimum, that is applied to the stellar particles when computing the flattening[2], ϵ. We compute the halo flattening for galaxies in the Ref-L100N1504 simulation, denoting this quantity as $\epsilon_{\mathrm{dm}}^{\mathrm{Ref}}$, and also for their counterparts identified in a simulation of the same volume, at the same resolution, but considering only collisionless gravitational dynamics (DMONLY-L100N1504). This latter quantity, which we denote as $\epsilon_{\mathrm{dm}}^{\mathrm{DMO}}$, is instructive because it describes the *intrinsic* shape of the halo that emerges in the absence of the dissipative physics of galaxy formation, and thus enables us to distinguish between cause and effect. The haloes are paired between the Ref and DMONLY simulations using the bijective particle matching algorithm described by Schaller et al. (2015a), which successfully pairs 2678 of the 2703 haloes that host spheroidal and well-aligned oblate galaxies (99.1 percent; see Section 4.2 for the definition of the sample).

---

[2]We find that correlations between galaxy morphology or velocity anisotropy with the 'global' halo morphology, i.e. considering all dark matter particles bound to the main subhalo, are weak. This is perhaps unsurprising, since the galaxy is most directly influenced by the inner halo (Zavala et al., 2016), and it is well established that the morphology and kinematics of central galaxies are not strongly correlated with those of their host haloes (e.g. Sales et al., 2012).

4.3.1 Dark matter and stellar structures

Fig. 4.5 shows the distribution of the matched galaxies in the $v_{\rm rot}/\sigma_0$ - ϵ plane. Here, the cells and points are coloured by the median value of $\epsilon_{\rm dm}^{\rm Ref}$ and $\epsilon_{\rm dm}^{\rm DMO}$ in the upper and lower panels, respectively. Both panels show a clear trend such that, in the regime of intermediate rotational support, the flattening of the galaxy correlates significantly with the flattening of the central regions of its parent halo, irrespective of whether $\epsilon_{\rm dm}$ is measured in the Ref or DMONLY simulation.

The influence of the morphology of the halo on that of the galaxy is shown more clearly in the upper panel of Fig. 4.6 where, in analogy to the right hand panel of Fig. 4.4, we show the deviation of a galaxy's flattening parameter from the median flattening of galaxies with similar kinematics, $\epsilon - \tilde{\epsilon}_{[v_{\rm rot}/\sigma_0]}$, here as a function of the inner halo flattening. The red curve adopts $\epsilon_{\rm dm}^{\rm Ref}$ as the halo flattening diagnostic, and should be compared to the upper panel of Fig. 4.5, whilst the blue curve adopts $\epsilon_{\rm dm}^{\rm DMO}$ and shows the correlation present in the lower panel of Fig. 4.5. As per the yellow dashed curve of Fig. 4.4b, dotted and dot-dashed thick lines here denote the median relations constructed using the sub-set of galaxies with $M_\star > 10^{10.5} \, {\rm M}_\odot$.

The formation of stars following the dissipative collapse of gas drives dark matter haloes towards a more spherical and axisymmetric morphology (e.g. Katz and Gunn, 1991; Dubinski, 1994; Evrard et al., 1994; Springel et al., 2004; Kazantzidis et al., 2004; Bryan et al., 2012, 2013), such that in general $\epsilon_{\rm dm}^{\rm DMO} > \epsilon_{\rm dm}^{\rm Ref}$ (see Fig. 4.5). The two halo flattening diagnostics are strongly correlated ($\rho_{\rm Sp} > 0.5$) but the fractional deviation from the 1:1 relation correlates, as could be expected, with the halo's stellar mass fraction within $30 \, {\rm kpc}$. The morphological transformation of the halo by dissipative physics therefore acts to compress the dynamic range in $\epsilon_{\rm dm}$, steepening the gradient of the $(\epsilon - \tilde{\epsilon}_{[v_{\rm rot}/\sigma_0]}) - \epsilon_{\rm dm}$ and $\delta - \epsilon_{\rm dm}$ relations. However, the Spearman rank correlation coefficients of these relationships are significantly higher when considering $\epsilon_{\rm dm}^{\rm Ref}$; for the former we recover $\rho_{\rm Sp} = (0.38, 0.55)$ for ($\epsilon_{\rm dm}^{\rm DMO}, \epsilon_{\rm dm}^{\rm Ref}$) respectively, whilst for the latter relationship we recover $\rho_{\rm Sp} = (0.21, 0.46)$. The compression of the dynamic range therefore does not preserve the rank ordering in $\epsilon_{\rm dm}$, and indicates
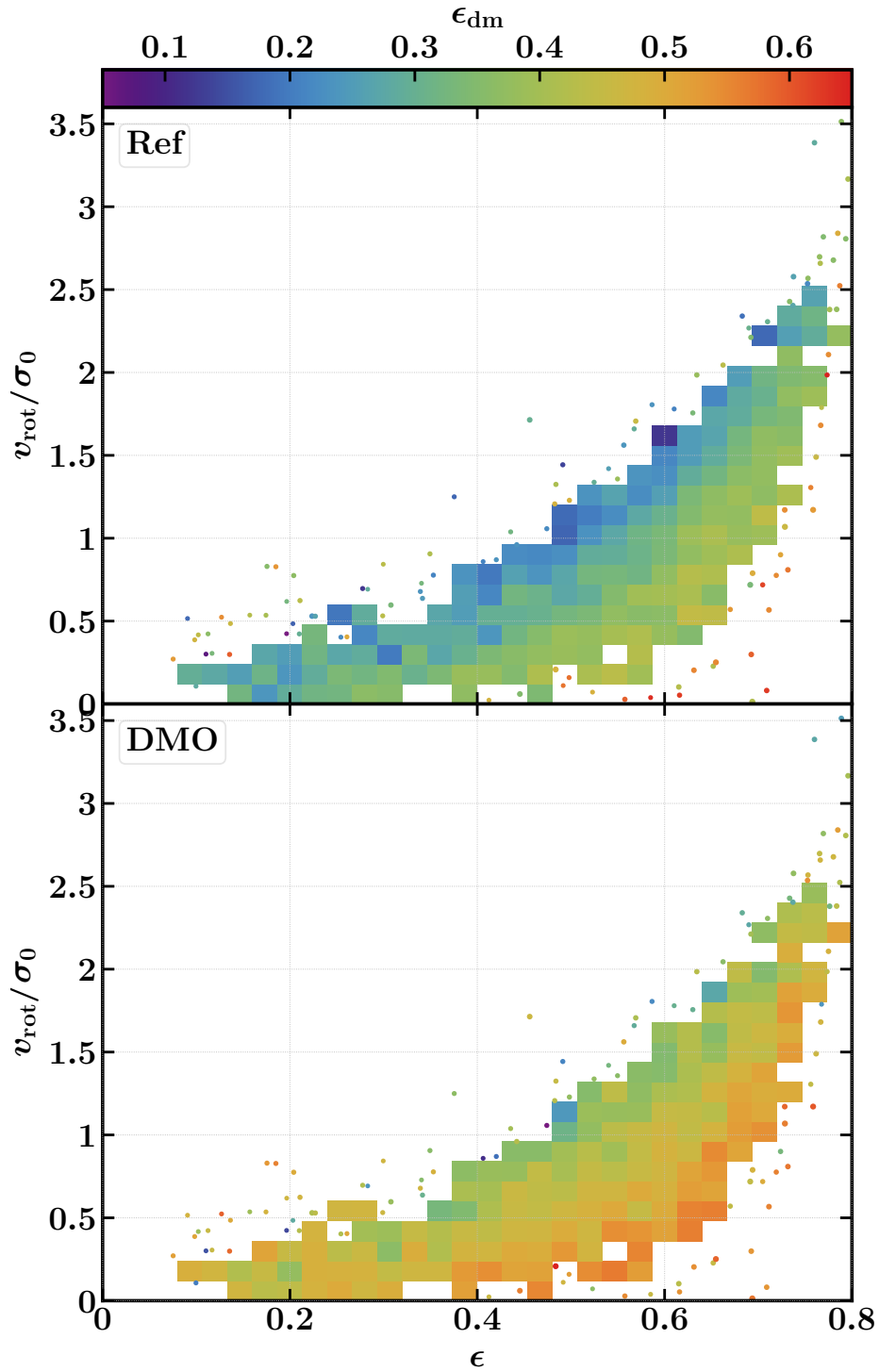
Figure 4.5: The same sample of galaxies shown in the lower panel of Fig. 4.1, but here the cells are colour-coded by the flattening of the inner ($< 30\,\mathrm{pkpc}$) dark matter halo, ϵ_{dm}. In the upper panel, this quantity is equated to the flattening of the dark matter halo in the Reference simulation, $\epsilon_{\mathrm{dm}}^{\mathrm{Ref}}$, whilst in the bottom panel it is equated to the flattening of the corresponding halo in dark matter-only simulation, $\epsilon_{\mathrm{dm}}^{\mathrm{DMO}}$. Irrespective of which measure is used, the most flattened galaxies at fixed $v_{\mathrm{rot}}/\sigma_0$ are preferentially hosted by dark matter haloes whose inner regions are more flattened.
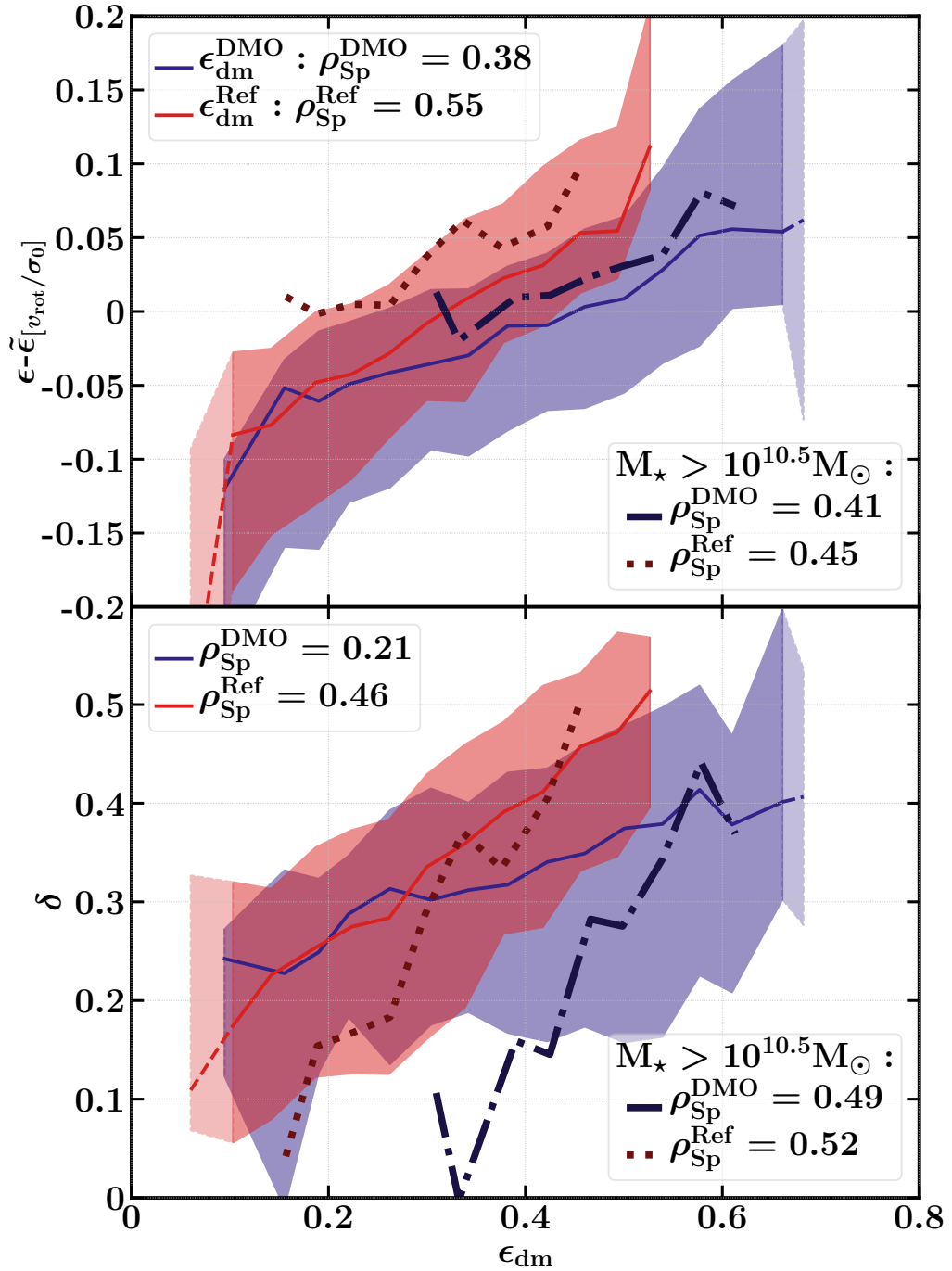
Figure 4.6: The deviation of a galaxy's flattening, ϵ from the median flattening for galaxies of similar $v_{\mathrm{rot}}/\sigma_0$ ($\epsilon - \tilde{\epsilon}_{[v_{\mathrm{rot}}/\sigma_0]}$, *upper panel*), and the anisotropy of the stellar velocity dispersion (δ, *lower panel*), as a function of the flattening of the inner dark matter halo, ϵ_{dm}. The solid lines and shaded regions denote the median relations and the 1σ ($16^{\mathrm{th}} - 84^{\mathrm{th}}$ percentile) scatter about them, respectively. The red curves adopt $\epsilon_{\mathrm{dm}}^{\mathrm{Ref}}$ as the halo flattening diagnostic, the blue curves adopt $\epsilon_{\mathrm{dm}}^{\mathrm{DMO}}$. Medians are drawn with dashed lines in bins sampled by fewer than 5 galaxies. Dotted and dot-dashed thick lines represent the corresponding median relations for the high-mass ($M_\star > 10^{10.5}\,\mathrm{M_\odot}$) sub-population for which only bins sampled by more than 5 galaxies are drawn.

that this property is, perhaps unsurprisingly, not the sole influence on galaxy morphology at fixed $v_{\rm rot}/\sigma_0$. Nonetheless, the panel shows that, irrespective of which halo flattening diagnostic is considered, there is a clear positive correlation between the morphology of the galaxy (at fixed $v_{\rm rot}/\sigma_0$) and that of its host halo. The persistence of the correlation when considering $\epsilon_{\rm dm}^{\rm DMO}$ demonstrates that it is intrinsic, and does not emerge as a *response* to the formation of a flattened galaxy at the halo centre. This engenders confidence that there is a causal connection between a galaxy's morphology and that of its host inner dark matter halo, which agrees with the findings of Zavala et al. (2016).

4.3.2 Dispersion anisotropy and dark matter

Having seen that the deviation of a galaxy's flattening from the median flattening at fixed $v_{\rm rot}/\sigma_0$, $\epsilon - \tilde{\epsilon}_{[v_{\rm rot}/\sigma_0]}$, correlates with both the anisotropy of the stellar velocity dispersion, δ (see Fig. 4.4), and the morphology of the dark matter halo, $\epsilon_{\rm dm}$ (see Fig. 4.5), we check the correlation between δ and $\epsilon_{\rm dm}$, shown in the bottom panel of Fig. 4.6. Again, dotted and dot-dashed thick lines here correspond to the sub-set of galaxies with $M_\star > 10^{10.5}\,{\rm M_\odot}$. There is a clear positive correlation between δ and $\epsilon_{\rm dm}$, which again persists when one considers $\epsilon_{\rm dm}^{\rm DMO}$ rather than $\epsilon_{\rm dm}^{\rm Ref}$, indicative of an intrinsic rather than an induced correlation. We note that in the specific case of high-stellar mass galaxies, haloes whose central regions are relatively unflattened induce significantly less anisotropy than is the case for the broader galaxy population; this is to be expected since high-stellar mass galaxies also exhibit high stellar mass *fractions* ($f_\star = M_\star/M_{200}$, see e.g. Fig. 8 of Schaye et al., 2015), mitigating the influence of the inner halo. Nevertheless, the trend is qualitatively similar for galaxies of all masses, and the corollary is thus that the anisotropy of a galaxy's stellar velocity dispersion is in part governed by the morphology of its inner dark matter halo, with flattened haloes inducing greater anisotropy. The intrinsic morphology of dark matter haloes is likely governed by a combination of their formation time and their intrinsic spin; Allgood et al. (2006) note that earlier forming haloes (at fixed mass) are systematically more spherical, Bett et al. (2007) show that intrinsically flatter haloes exhibit a small but sys-

tematic offset to greater spin values, and Jeeson-Daniel et al. (2011) found that formation time (or concentration) and spin are the first two principal components governing dark matter halo structure. These properties emerge simply from the distribution of fluctuations in the initial conditions of the simulations.

4.4 Summary and discussions

We have performed a quantitative comparison between diagnostics for the morphology and internal kinematics of the stellar component of galaxies in the EAGLE suite of cosmological simulations, and investigated the origin of scatter in this relation. We consider 4155 present-day central galaxies with stellar masses $M_\star > 10^{9.5} \, M_\odot$, and in later analyses focus on the sub-set of 2703 spheroidal or oblate galaxies whose structural and kinematic axes are well-aligned. Our results can be summarized as follows:

1. Examination of the internal kinematics (quantified via $v_{\mathrm{rot}}/\sigma_0$) as a function of morphology (quantified via the flattening, ϵ) reveals a correlation between the two: as expected from dynamical considerations, rotationally-supported galaxies tend to be flatter than dispersion-supported counterparts. However, for all but the most rotationally-supported galaxies, there is significant scatter so that the population of galaxies at fixed $v_{\mathrm{rot}}/\sigma_0$ exhibits a broad range of morphologies. The most massive galaxies ($M_* \gtrsim 10^{10.5} \, M_\odot$) tend to populate the high-ϵ regime, being either rotationally-supported discs or prolate spheroids. Excision of galaxies with prolate morphology and/or mis-aligned structural and kinematic axes enables analysis of the morpho-kinematics of the remaining subsample with the tensor virial theorem (Fig. 4.1).

2. The tensor virial theorem (Section 3.2) indicates that the flattening of a collisionless system, at fixed $v_{\mathrm{rot}}/\sigma_0$, is governed by the anisotropy of its velocity dispersion, δ (eq. 3.16). This prediction is borne out, in a quantitative sense, by the simulated galaxies. At any $v_{\mathrm{rot}}/\sigma_0$, more flattened oblate galaxies exhibit

greater δ, for all galaxy masses (Fig. 4.4).

3. A similar trend to that shown in Fig. 4.4 is seen if one correlates ϵ at fixed $v_{\rm rot}/\sigma_0$ with the flattening of the inner ($< 30\,{\rm pkpc}$) dark matter halo, $\epsilon_{\rm dm}$. This suggests that a galaxy's morphology is influenced in part by the morphology of its host halo, which is a proxy for the structure of the potential in the region traced by stellar particles. We verify that this is an intrinsic (rather than induced) correlation by measuring $\epsilon_{\rm dm}$ in both the Reference EAGLE simulation (denoting this quantity $\epsilon_{\rm dm}^{\rm Ref}$) and in a simulation considering only collisionless dynamics starting from identical initial conditions ($\epsilon_{\rm dm}^{\rm DMO}$), finding similar trends in both cases (Fig. 4.5).

4. The anisotropy δ correlates with the flattening of the inner dark matter halo, regardless of whether one considers the flattening of the halo in the Reference simulation, $\epsilon_{\rm dm}^{\rm Ref}$, or its counterpart in the dark-matter-only simulation, $\epsilon_{\rm dm}^{\rm DMO}$ (Fig. 4.6).

We point out that the link we have established between the shapes of galaxies and the flattening of the inner dark matter halo complements in a fundamental way previous work on the *alignments* of galaxies with surrounding matter. Indeed, it is well established both theoretically and observationally that galaxies tend to preferentially align themselves with the (dark matter-dominated) large-scale potential (e.g., Deason et al. 2011; Velliscig et al. 2015a,b; Welker et al. 2017, 2018). This leads to intrinsic alignments of neighbouring galaxies, which acts as a major source of error in measurements of cosmic shear (e.g., Hirata and Seljak 2004; Bridle and King 2007). Our work demonstrates that, not only do galaxies tend to align themselves in a preferential way, but their actual shapes are also determined, to an extent, by the shape of the (local) dark matter potential well.

Our finding that the anisotropy of the stellar velocity dispersion of galaxies correlates with the intrinsic morphology of their inner dark matter haloes is intriguing. The finding that the correlation persists when using the morphology of the inner halo in the corresponding dark matter only simulation is indicative of a causal connection (see also

Zavala et al., 2016). In such a scenario, the formation of a dark matter halo whose inner mass distribution is intrinsically flattened (in the absence of the dissipative physics of galaxy formation) will foster the formation of a galaxy whose stellar velocity dispersion is preferentially expressed in the plane orthogonal to the axis of rotation. As predicted by the tensor virial theorem, this anisotropy fosters the formation of a galaxy that is flatter than typical for galaxies with similar internal $v_{\mathrm{rot}}/\sigma_0$.

The relationship between δ and ϵ_{dm} revealed by EAGLE is, in principle, testable with observations. If one stacks galaxies of similar flattening in bins of $v_{\mathrm{rot}}/\sigma_0$, and measures the flattening of the total matter distribution (e.g. with weak gravitational lensing), the simulations indicate that one should expect the latter to be systematically greater for galaxies of lower $v_{\mathrm{rot}}/\sigma_0$. We note that the overlap of the SDSS-IV/MaNGA integral field survey with the deep imaging fields of the Hyper Suprime-Cam (HSC) survey offers a potential means by which this might be achieved.

Chapter 5

Morpho-kinematics of globular cluster systems and their host galaxy

5.1 Introduction

Globular clusters have been now shown to be a crucial class of astrophysical objects in the study of galaxy formation. These are compact and massive roughly spheroidal associations of stars, with half-light radii of a few parsecs for stellar masses ranging between $\sim 10^4$ and $\sim 10^6$ M$_\odot$ (Brodie and Strader, 2006). Extra-galactic observations of these objects have been recorded in a large number of galaxies, with stellar masses as low as 10^9 M$_\odot$. Despite their origin being poorly understood, they are generally inferred to be significantly old (over 10 Gyr; Cohen et al., 1998; Kissler-Patig et al., 1998; Beasley et al., 2000, 2004; Forbes et al., 2001; Brodie and Larsen, 2002; Schroder et al., 2002; Puzia et al., 2005; Strader et al., 2005; Marín-Franch et al., 2009; VandenBerg et al., 2013) implying that their formation occurred mostly in the early Universe. Nevertheless, it is also suggested that their formation may also occur at all epochs due to the observation of young massive clusters with the Hubble Space Telescope (Portegies Zwart et al., 2010). Consequently, they are believed to provide powerful diagnostics of their host galaxy assembly.

Among the characteristics of globular clusters relevant to the study of their host history, their metallicity is a fundamental one. Usually interpreted from their colour in observations (Yoon et al., 2006; Blakeslee et al., 2010), their metallicities are often distributed in a bimodal fashion (Zepf and Ashman, 1993; Whitmore et al., 1995; Gebhardt and Kissler-Patig, 1999; Kundu and Whitmore, 2001; Larsen et al., 2001; Peng et al., 2006; Sinnott et al., 2010; Brodie et al., 2012) suggesting the two populations may exhibit different formation mechanisms that cannot yet be easily distinguished owing to the limited precision of current age measurements (Rosenberg et al., 1999; Strader et al., 2005; Marín-Franch et al., 2009; Forbes and Bridges, 2010; Hansen et al., 2013; Leaman et al., 2013; VandenBerg et al., 2013; Forbes et al., 2015).

Indeed, together with this bimodality, metal-rich and metal-poor globular cluster populations diverge in other aspects. metal-rich globular clusters appear more centrally concentrated within their host galaxy halo than their metal-poor counterparts (Geisler et al., 1996; Bassino et al., 2006; Goudfrooij et al., 2007; Faifer et al., 2011; Strader et al., 2011; Forbes et al., 2012). metal-rich and poor globular clusters also differ in size with the former being smaller than the latter (Kundu and Whitmore, 2001; Jordán et al., 2005; Masters et al., 2010). Their populations also show significant differences in shape and dynamics, with metal-rich globular cluster populations more likely to be flattened and rotationally supported (Lee et al., 2010; Strader et al., 2011; Park and Lee, 2013; Pota et al., 2013). At the moment, the scenario that prevails for explaining these differences suggests that metal-rich globular clusters are formed within the galaxy they inhabit (formation *in-situ*), while metal-poor globular clusters are accreted from interactions with former satellites (formation *ex-situ*) (Ashman and Zepf, 1992; Zepf and Ashman, 1993; Côté et al., 1998; Beasley et al., 2002; Masters and Ashman, 2010; Arnold et al., 2011).

We showed in Chapter 2 how the galaxy formation field has, in the last 5 years, taken a leap forward with the development of realistic simulations that combine in a cosmological context the self-consistent solution of gravitational and hydrodynamical interactions with specific treatments for physics operating at unresolved scales. Some recent simulations attempted to add such a treatment that follows the formation and evolu-

tion of stellar clusters: this is notably the case of the E-MOSAICS project (Pfeffer et al., 2018; Kruijssen et al., 2019). This project builds on the successes of the EAGLE model in producing realistic populations of galaxies by incorporating the MOSAICS (Kruijssen et al., 2011) semi-analytic model of the formation and evolution of stellar clusters. One of their notable achievements was to demonstrate the ability to recover the assembly histories of galaxies via the age-metallicity distribution of their globular clusters.

Relative to that, an important observational finding was that not only do metal-rich globular cluster systems show more flattened and rotational morpho-kinematics than their metal-poor counterparts, but they also appear to trace those same properties of the galaxy itself (Lee et al., 2010; Strader et al., 2011; Park and Lee, 2013; Pota et al., 2013). This observational finding is therefore a useful diagnostic with which to confront the E-MOSAICS simulations: we aim at verifying with its simulated galaxies if this trend is also reproduced.

This Chapter is structured as follows. We describe in Section 5.2 our numerical tools, by giving an overview of the E-MOSAICS suite of simulations with our criteria for characterizing globular cluster populations, as well as the techniques for computing our morphological and kinematic diagnostics. Section 5.3 focusses on the results we present, notably our galaxy sample demographics according to their globular cluster population morpho-kinematics, the velocity, kinematics and morphology correspondence between the globular cluster and field star populations, and investigation of the link between the morphology and kinematics in field stars and metal-rich globular clusters. Lastly, we discuss and summarize our findings in Section 5.4.

5.2   Numerical methods

We presented in Section 2.3.2 an overview of the E-MOSAICS project (Pfeffer et al., 2018; Kruijssen et al., 2019), a suite of simulations that embeds the semi-analytic model of stellar cluster formation and evolution MOSAICS (Kruijssen et al., 2011)

within the gas-dynamic model of cosmological galaxy formation of EAGLE (Schaye et al., 2015; Crain et al., 2015). We describe in Section 5.2.1 the composition of a subhalo within these simulations, as well as how we define globular clusters and our sample criteria. We introduce our diagnostics for measuring simulated structures' rotational support and flatness in Sections 5.2.2 and 5.2.3.

5.2.1 Identifying galaxies and their globular cluster populations

The E-MOSAICS suite of simulations is built on the EAGLE model, and hence, as there, matter is represented by particles that describe various matter components (star, gas, dark matter and black holes). In that collection of particles, we first identify haloes/groups through a friend-of-friends algorithm (FoF) applied to the DM distribution, groups to which baryonic particles are attached depending on these particles' nearest DM neighbour. We then identify galaxies through substructures we name 'subhaloes'. Given the FoF set of particles that represent a halo, we identify its subhaloes by applying the SUBFIND algorithm (Springel et al., 2001; Dolag et al., 2009), and define as galaxies the stellar content of each subhalo. The subhalo containing the particle with lowest gravitational potential is defined as the 'central' subhalo, while all others are considered its 'satellites'. The position of that particle defines the halo centre of potential. Notably, we use this centre to compute the halo spherical overdensity mass, M_{200}, for the adopted enclosed density contrast of 200 times the critical density, as well as the galaxy's stellar mass, $M_\star$, summing all stellar particles enclosed within a $30\,\mathrm{pkpc}$ spherical aperture.

Specific to the E-MOSAICS model is a subgrid model governing the formation and evolution of stellar clusters (SCs). Each stellar particle has some fraction of its mass tracked in a clustered form: in practice, the implementation is done in such way that each stellar particle traces a population of SCs. We define globular clusters (GCs) as SCs with age older than 2 Gyr and with mass $m_{\mathrm{GC}} > 10^{4.5}\,\mathrm{M_\odot}$. As we are interested into averaged properties that represent all GCs of a population equally, we consider them to have equal mass for the rest of this work. Additionally, we consider as metal-

rich all GCs with metallicity ratio $[\text{Fe/H}] > -1$, and metal-poor if $[\text{Fe/H}] < -1$.

In this work we consider only central galaxies to avoid the complication of environmental effects. Our sample is composed of the 25 galaxies in the zoom-simulations presented by Pfeffer et al. (2018), and a selection of central galaxies from the periodic volume simulation Recal-L34N1034 (Crain et al., in prep.). The latter selection contains all central galaxies from Recal-L34N1034 with stellar mass $M_\star > 10^{9.5} \ \text{M}_\odot$, except 2 poorly sampled cases for which our morphological diagnostic applied to either the metal-rich GCs or metal-poor GCs could not converge (discussed in detail in Section 5.2.2). This leaves us with 230 galaxies of which 80 are considered Milky-Way (MW) mass-like, similarly to those selected for the zoom-simulations, with virial masses M_{200} ranging between 7×10^{11} and $3 \times 10^{12} \ \text{M}_\odot$. These latter cases will be explicitly highlighted throughout our study as a special MW-like sub-sample of 105 galaxies within our total (box+zooms) sample of 255 galaxies.

5.2.2 Characterising morphology

To characterise the morphology of a population of particles, we use the morphological parameter α_m constructed in Chapter 3. As we showed there, this diagnostic separates the colour-mass diagram reasonably into its blue cloud and red sequence. As a reminder, it requires the use of the iterative form of the reduced inertia tensor in order to estimate characteristic scale lengths $a > b > c$, respectively associated to the major, intermediate and minor axes of the population of particles. At each iteration, those are obtained from the squareroot of the eigenvalues and associated eigenvectors of the tensor:

$$\mathcal{M}_{ij}^r = \frac{\sum_p \frac{m_p}{\tilde{r}_p^2} r_{p,i} r_{p,j}}{\sum_p \frac{m_p}{\tilde{r}_p^2}}, \tag{5.1}$$

where m_p and r_p are the mass and position of each particle p, while $\tilde{r}_p$ represents the ellipsoidal radius (see equation 3.10). The convergence of this method is globally well achieved within 8-10 iterations, we note however that 2 cases failed to converge because of poor sampling: during the iteration process, the ellipsoidal aperture resulting from the constant volume condition reached a configuration that would leave no

particles inside. As explained in Section 5.2.1, we removed these 2 cases from our sample. From there, the ellipticity and triaxiality are computed as $\epsilon = 1 - c/a$ and $T = (a^2 - b^2)/(a^2 - c^2)$ leading to $\alpha_{\mathrm{m}} = (\epsilon^2 + 1 - T)/2$.

In order to assess the effect of projection on morphological properties, we adapted the above-described process to a two-dimensional case where only 2 scale lengths $a > b$ and associated major and minor axes are sought. While equation 5.1 remains unchanged (the indexes i and j being associated to 2 axes instead of 3), the evaluation of the ellipsoidal radius loses a term, and the constant volume condition becomes a constant area one:

$$\tilde{r}_p^2 \equiv r_{p,a}^2 + \frac{r_{p,b}^2}{(b/a)^2} \leq \frac{a}{b}(30\,\mathrm{pkpc})^2. \tag{5.2}$$

Likewise, the iterative process terminates when the ratio b/a converges within 1 percent. We obtain from this process the projected ellipticity

$$\epsilon_{\mathrm{proj}} = 1 - \frac{b}{a}. \tag{5.3}$$

This process requires the input particle positions to have 2 coordinates, those within the plane perpendicular to the axis of projection. In our case, we are interested in computing 3 projections along each of the 3 axes[1] recovered by application of the iterative reduced inertia tensor in its 3D form to the stellar particles i.e. the galaxy's minor, intermediate and major axes. Accordingly, after calculating the coordinates of each particles along these 3 axes, we apply to each pair of coordinates the iterative reduced inertia tensor in its 2D form.

5.2.3 Characterizing kinematics

Various techniques exist for quantifying the kinematics of a population in a simulation. We showed in Section 3.4.2 that most conventionally used methods provide equivalent diagnostics. Among all the methods we tested, the non-parametric ratio of rotation and dispersion velocities $v_{\mathrm{rot}}/\sigma_0$ has the advantage of a convenient framework

---

[1]that represent an orthonormal basis of the 3D space

for understanding the relationship between morphologies and kinematics via the velocity dispersion anisotropy δ as shown in Chapter 4. Additionally, this framework connects with recent observations where the v_{rot} and σ_0 velocity quantities of populations of globular clusters have been measured for a sample of galaxies, such as with the SLUGGS survey (Pota et al., 2013; Brodie et al., 2014). We proceed with this technique as described in Section 3.4.1.

5.3 Results

We first examine in Section 5.3.1 the distributions of morphological and kinematic properties for each GC population. We then look at the relationship for various properties between GC populations and the galaxy in Section 5.3.2: we notably look at different velocity properties, at kinematic properties, and at morphological properties. In Section 5.3.3 where we discuss the relationship between morphological and kinematic properties, separately for field star and metal-rich GC systems.

5.3.1 Globular cluster demographics

Due to its large range of stellar masses, our sample of simulated galaxies exhibits a significant diversity of GC system demographics, with GC populations ranging between 28 and 5848 members with a median value of 444 (807 for the MW-like sub-sample). In terms of metal-poor/rich sub-demographics, metal-poor GCs are often in the minority with the 5th and 95th percentiles of population ratios respectively at 6 and 49 percent for a median at 17 percent. For this reason, the following results often show parameter distributions for metal-rich GC populations that tend to be similar to those of complete GC populations.

We show in Figure 5.1 the distributions of kinematic and morphological parameters of various populations of GCs for the full sample of galaxies. Notably, blue, red and yellow distributions represent, respectively, parameters computed for the metal-poor,
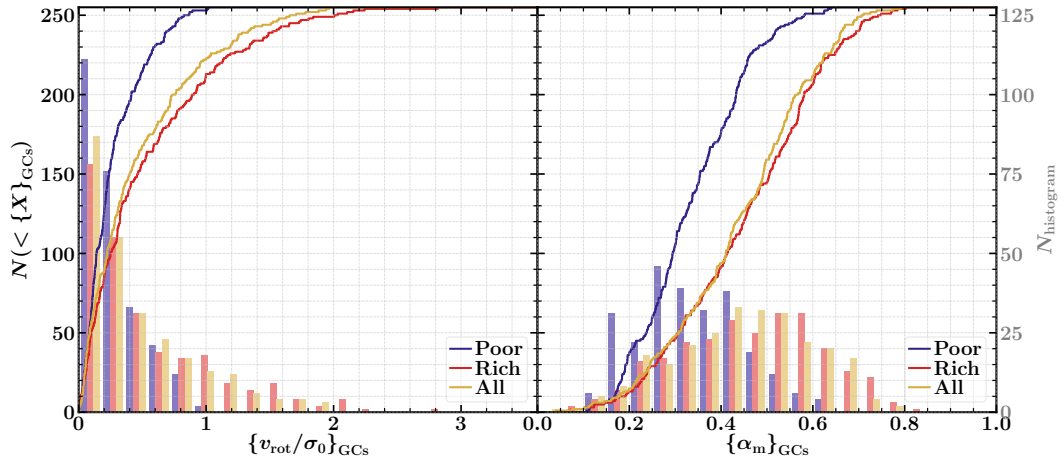
Figure 5.1: Globular cluster population kinematics - left hand panel - and morphology - right hand panel - parameter distributions. Each panel presents the distributions of parameters computed for each galaxy: metal-poor, metal-rich and complete GC populations are shown respectively in blue, red and yellow colour. Distributions are shown with a non-parametric cumulative distribution as coloured step curves in the foreground, and a binned histogram as desaturated bar plots in the background. The cumulative distribution is scaled along the left hand side y-axis, while the histogram is scaled along the right hand side y-axis. Lastly, the histograms are computed from a selection of 12 bins linearly dividing the represented x-axis ranges, and each population is presented as side-by-side bars in each bin.

the metal-rich and the complete GC populations. On the left hand panel are shown distributions for the $v_{\mathrm{rot}}/\sigma_0$ parameter while the right hand panel exhibits the distributions for the α_{m} parameter. The distributions are shown in 2 ways: step curves in the foreground represent cumulative distributions whose values are scaled on the left-hand side y-axis, while the bars shown in the background represent the histogram whose values are scaled on the right hand side y-axis (in grey). The cumulative distribution is non-parametric i.e. each increment is dependent on the sample, while the histogram is computed over 20 bins regularly distributed along the represented x-axis. For the latter, each bin is split into 3 bars of different colours representing each GC population.

The kinematic distributions exhibit a globally skewed contiguous profile, with median values of $v_{\mathrm{rot}}/\sigma_0 = 0.20$, 0.33 and 0.31 respectively for the metal-poor, the metal-rich and the complete GC populations. Above those rotation-support values, skewed distributions expand towards 95th percentile values of respectively $v_{\mathrm{rot}}/\sigma_0 = 0.73$, 1.58 and 1.36, corresponding to between 3.6 and 4.7 times the median values. These figures confirm the trend that the cumulative distributions show more clearly: the kinemat-

ics of metal-poor GCs appear more dispersion supported than those of the metal-rich GCs. Also, the comparison with the complete populations reveals that the median values of both ratios $\{v_{\rm rot}/\sigma_0\}_{\rm Poor} / \{v_{\rm rot}/\sigma_0\}_{\rm All}$ and $\{v_{\rm rot}/\sigma_0\}_{\rm Rich} / \{v_{\rm rot}/\sigma_0\}_{\rm All}$ are respectively 0.76 and 1.11, meaning that the kinematics of the complete population is often between that of the metal-poor and metal-rich populations. These trends are slightly more pronounced for the MW-like sub-sample, with these median values being respectively 0.37 and 1.16, and median values of $v_{\rm rot}/\sigma_0$ being respectively 0.19, 0.77 and 0.69 for the metal-poor, metal-rich and complete populations.

On the right hand panel of Figure 5.1, the morphological distributions are contiguous and not so strongly skewed. The morphological parameters have median values of respectively $\alpha_{\rm m} = 0.33$, 0.46 and 0.45 for the metal-poor, metal-rich and complete populations, and respectively 0.34, 0.54 and 0.53 for the MW-like sub-sample. Also, the median values of both ratios $\{\alpha_{\rm m}\}_{\rm Poor} / \{\alpha_{\rm m}\}_{\rm All}$ and $\{\alpha_{\rm m}\}_{\rm Rich} / \{\alpha_{\rm m}\}_{\rm All}$ are respectively 0.77 and 1.02, and 0.70 and 1.02 for the MW-like sub-sample. As was found for kinematics, metal-poor and metal-rich GC populations have significantly distinct morphologies, with the former being more elliptical and the latter being more disky, while the complete populations have an intermediate morphology between those of the sub-populations. The difference between the full sample and the MW-like sub-sample is however not as pronounced for morphological properties as it is for kinematic properties.

5.3.2 Correspondence of GC and host galaxy properties

Velocity properties

We look in this section at the relationship between velocity properties of galaxies and their globular cluster populations. To illustrate further those relationships, we included the observational data from the SLUGGS survey (Pota et al., 2013) that presented measurements of velocity properties for GC populations of 12 early-type galaxies. They compiled their own spectroscopic measurements of radial velocities for their selection

of GCs per galaxy, with long-slit spectroscopy and/or extragalactic planetary nebula kinematic measurements from other works (van der Marel and Franx, 1993; Bender et al., 1994; Fried and Illingworth, 1994; Kronawitter et al., 2000; Simien and Prugniel, 2000; Coccato et al., 2009; Proctor et al., 2009; Weijmans et al., 2009; Forestell and Gebhardt, 2010), to compute the amplitude of the rotation and velocity dispersion (as per Foster et al., 2011) within 3 times the effective radii. They applied this technique to both red and blue GC populations, selected based on a colour bimodality analysis, to obtain kinematic measurements for both populations: we will consider in this work that red and blue GCs represent respectively metal-rich and metal-poor GCs (Yoon et al., 2006; Blakeslee et al., 2010).

In Figure 5.2, we show the relationships between the velocity dispersion σ_0 of both metallicity-split GC sub-populations, and that of the galaxy and the dark matter halo. This 4 panel figure shares respectively y-axis and x-axis characteristics between panels of the same row and of the same column. Horizontally, y-axes of panels on the upper row show the metal-rich GC populations' velocity dispersions $\{\sigma_0\}_{\text{GCs}}^{\text{Rich}}$, while the metal-poor GC populations' dispersions $\{\sigma_0\}_{\text{GCs}}^{\text{Poor}}$ are scaled along the lower row y-axes. The x-axes of panels on the left hand side columns scale the velocity dispersion $\{\sigma_0\}_\star$ of the galaxies, while the dark matter halo dispersions $\{\sigma_0\}_{\text{DM}}$ are scaled along the right hand side x-axes. In each panel, we represent our sample in scattered dots, coloured by the stellar masses on a logarithmically scaled colour map. The dots vary between 2 sizes, with bigger dots representing galaxies from our MW-like sub-sample while non-MW-like galaxies are shown as smaller dots. In the foreground of the left column panels, grey error-barred dots are plotted according to Pota et al. (2013)'s SLUGGS survey observational data. Lastly, each panel has in the upper left corner the Spearman rank correlation coefficient and p-value of our E-MOSAICS sample for the associated relationship.

We focus first on the comparison between E-MOSAICS and SLUGGS data in the left hand column panels. We note that E-MOSAICS GC or stellar populations tend to have lower velocity dispersions than those of the 12 galaxies from SLUGGS (more of them can be found at higher σ_0 than the represented range). On one hand, this could be due
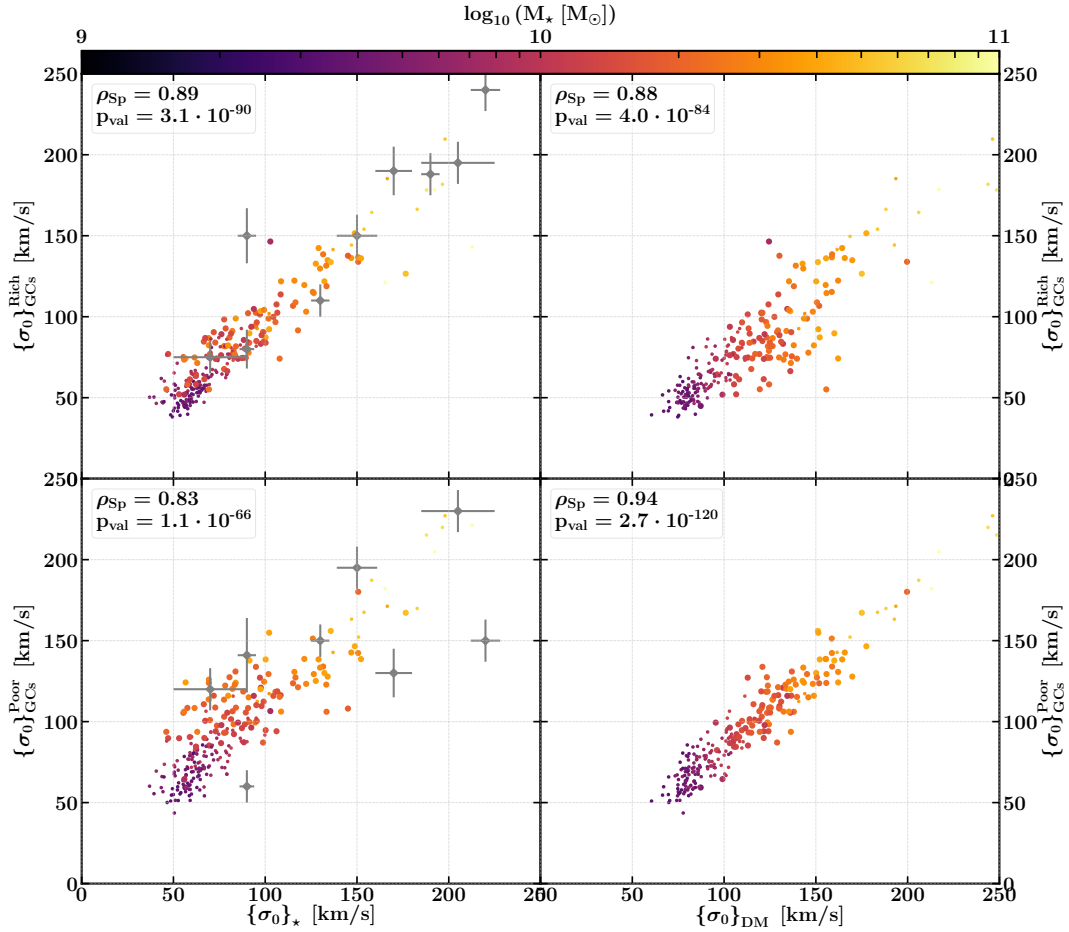
Figure 5.2: Relation between the velocity dispersion σ_0 of distinct content within galaxies with their stellar mass. The upper and lower row y-axes respectively show the metal-rich and metal-poor GC populations' velocity dispersions $\{\sigma_0\}_{\mathrm{GCs}}^{\mathrm{Rich}}$ and $\{\sigma_0\}_{\mathrm{GCs}}^{\mathrm{Poor}}$. The left hand and right hand column x-axes respectively show the field star and inner halo dark matter velocity dispersions $\{\sigma_0\}_\star$ and $\{\sigma_0\}_{\mathrm{DM}}$. The relationships are presented as scatter plots of the full sample colour coded according to the galaxy stellar mass, with large dots highlighting galaxies comprising the MW-like sub-sample. Grey error-barred scatter plots are plotted in the foreground of both left hand side panels to show observational measurements from the SLUGGS survey (Pota et al., 2013). Each relationship shows strong correlations with Spearman rank coefficients of respectively 0.89, 0.88, 0.83 and 0.94 for the upper left, upper right, lower left and lower right panels.

to the SLUGGS survey selecting massive early-type galaxies[2], thus likely to exhibit significantly higher velocity dispersions. On the other hand, our velocity properties are estimated within an aperture of $30\,\mathrm{pkpc}$ while SLUGGS data depict kinematics within 3 times the galaxy effective radius: this often corresponds approximately to half of our aperture, thus depicting inner kinematics that is more likely to be dispersion-supported. Despite this, the agreement between simulated and observed data appears remarkable, both for metal-rich and poor dispersions.

Regarding the relationships themselves in all panels, we find that all velocity dispersions correlate with each other to various degrees. In particular, correlations appear slightly tighter in the upper left and lower right panels, namely, the relationships between metal-rich GCs and galactic dispersions $\{\sigma_0\}_{\mathrm{GCs}}^{\mathrm{Rich}}$ and $\{\sigma_0\}_\star$, and between metal-poor GCs and halo dispersions $\{\sigma_0\}_{\mathrm{GCs}}^{\mathrm{Poor}}$ and $\{\sigma_0\}_{\mathrm{DM}}$, with Spearman rank coefficients of respectively 0.89 and 0.94. The 2 other relationships have slightly lower Spearman rank coefficients (0.83 in the lower left panel and 0.88 in the upper right).

Globally, we can observe from the colour-coding that the galaxy stellar mass appears to be generally well correlated with all velocity dispersions as colour gradients follow naturally each correlation's progression. We note especially that the lower right $\{\sigma_0\}_{\mathrm{GCs}}^{\mathrm{Poor}}$ vs. $\{\sigma_0\}_{\mathrm{DM}}$ relationship shows a particularly tight correlation. The latter appears more discernible when examining how those gradients are profiled in relations displayed in the lower left and upper right panels. In the lower left panel, namely $\{\sigma_0\}_{\mathrm{GCs}}^{\mathrm{Poor}}$ vs. $\{\sigma_0\}_\star$, the colour gradient appears to evolve along the $\{\sigma_0\}_{\mathrm{GCs}}^{\mathrm{Poor}}$ y-axis, perpendicularly to the $\{\sigma_0\}_\star$ x-axis. In the upper right panel, namely $\{\sigma_0\}_{\mathrm{GCs}}^{\mathrm{Rich}}$ vs. $\{\sigma_0\}_{\mathrm{DM}}$, the colour gradient similarly appears to evolve along the $\{\sigma_0\}_{\mathrm{DM}}$ x-axis, perpendicularly to the $\{\sigma_0\}_{\mathrm{GCs}}^{\mathrm{Rich}}$ y-axis. Indeed, Spearman rank correlation coefficients between $M_\star$ and each of the 4 dispersions $\{\sigma_0\}_\star$, $\{\sigma_0\}_{\mathrm{GCs}}^{\mathrm{Rich}}$, $\{\sigma_0\}_{\mathrm{GCs}}^{\mathrm{Poor}}$ and $\{\sigma_0\}_{\mathrm{DM}}$ are respectively 0.77, 0.87, 0.92 and 0.96.

In light of this relationship with stellar mass, it is natural that reducing to the MW-like sub-sample reduces the range of dispersions covered. This causes correlations to be slightly less robust, especially for the 2 previously 'weakest' ones, with Spearman

---

[2]K-band absolute magnitudes ranging between -22.4 and -25.4 with a median at -24.1

rank coefficients of respectively 0.85, 0.65, 0.57 and 0.84 for the relations $\{\sigma_0\}_{\mathrm{GCs}}^{\mathrm{Rich}}$ vs. $\{\sigma_0\}_\star$, $\{\sigma_0\}_{\mathrm{GCs}}^{\mathrm{Poor}}$ vs. $\{\sigma_0\}_\star$, $\{\sigma_0\}_{\mathrm{GCs}}^{\mathrm{Rich}}$ vs. $\{\sigma_0\}_{\mathrm{DM}}$ and $\{\sigma_0\}_{\mathrm{GCs}}^{\mathrm{Poor}}$ vs. $\{\sigma_0\}_{\mathrm{DM}}$.

Similarly to the way Figure 5.2 showed the relation between velocity dispersions, we examine in Figure 5.3 the relation between rotational velocities of distinct galactic populations. However, while Figure 5.2 emphasized in its right hand column the relation between GC properties and halo properties, Figure 5.3 has only a single column similar to the left hand one in Figure 5.2 to look only at GC vs. galaxy properties. As there is little to no rotational ordered motion in the dark matter content, those plots would demonstrate little significance (although, we note Spearman rank correlation coefficients of respectively 0.19 and 0.58 for the relations of $\{v_{\mathrm{rot}}\}_{\mathrm{GCs}}^{\mathrm{Rich}}$ and $\{v_{\mathrm{rot}}\}_{\mathrm{GCs}}^{\mathrm{Poor}}$ with $\{v_{\mathrm{rot}}\}_{\mathrm{DM}}$). Therefore, the layout and characteristics between this Figure and Figure 5.2 left hand column are completely identical, except that are now shown the rotational velocities v_{rot} instead of the velocity dispersions σ_0.

The relationship between rotational velocities of GC populations and the galaxy stellar content shows greater differences than for velocity dispersions. Notably, between the metal-rich and poor GCs, only the rotational velocities of metal-rich GC populations show significant correlations with the stellar rotational velocities. The Spearman rank correlation coefficient for the former relationship is 0.70 while that for the relation between metal-poor GCs and stellar content sits at a weak value, 0.27. The correlation of the former (upper panel) is strongly scattered, with a visual link to stellar mass from the colour-coding: at fixed $\{v_{\mathrm{rot}}\}_\star$, $\{v_{\mathrm{rot}}\}_{\mathrm{GCs}}^{\mathrm{Rich}}$ seems to increase with higher stellar masses. SLUGGS data from massive galaxies seem to follow this trend, as they populate mostly the higher $\{v_{\mathrm{rot}}\}_{\mathrm{GCs}}^{\mathrm{Rich}}$ part of the relationship. In the lower panel, SLUGGS data appear very different to the E-MOSAICS data, with half of its represented galaxies showing higher rotational velocities in their metal-poor GC populations, with however large measurement uncertainties.
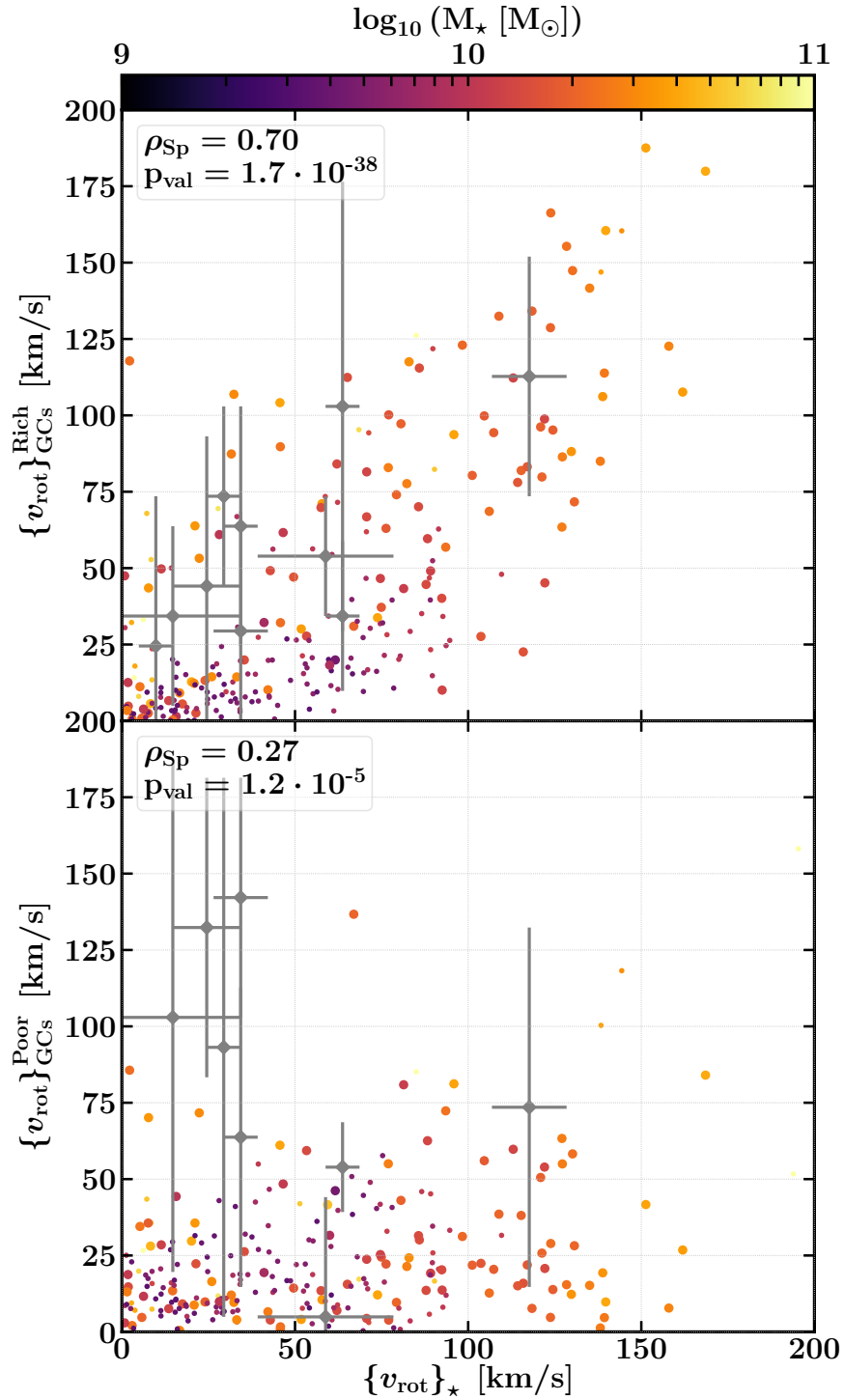
Figure 5.3: Relationship between the rotational velocity $v_{\rm rot}$ of metallicity split GC and field star populations with galaxy stellar masses. As per Figure 5.2 left column, upper and lower panel y-axes scale the metal-rich and metal-poor GC populations' rotational velocities $\{v_{\rm rot}\}_{\rm GCs}^{\rm Rich}$ and $\{v_{\rm rot}\}_{\rm GCs}^{\rm Poor}$, while x-axes scale the field star rotational velocities $\{v_{\rm rot}\}_\star$. Scatterplots are identical to Figure 5.2, colour-coded by stellar mass with larger dots for the MW-like sub-sample, and the grey error-barred scatterplots represent data from the SLUGGS survey (Pota et al., 2013). Spearman rank correlation coefficients are respectively equal to 0.70 and 0.27 for the upper and lower relationship.
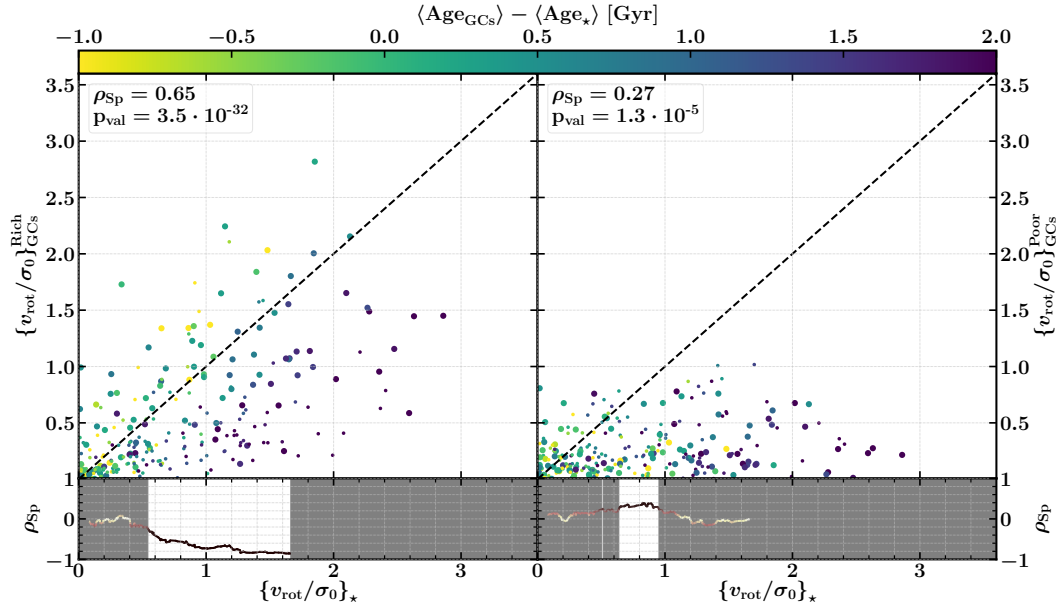
Figure 5.4: Relationship between the kinematics parameter v_{rot}/σ_0 of galaxy metallicity split GC and field star populations with the difference $\langle\text{Age}_{GCs}\rangle - \langle\text{Age}_\star\rangle$ between the GC and field stars average age. All panels represent on the x-axes the field star rotation-support parameter $\{v_{rot}/\sigma_0\}_\star$, and the y-axes of the upper left and right hand panels scale respectively the metal-rich and poor GC populations rotation-support parameter $\{v_{rot}/\sigma_0\}_{GCs}^{Rich}$ and $\{v_{rot}/\sigma_0\}_{GCs}^{Poor}$. As in Figures 5.2 and 5.3, y-x relationships in the upper panels are shown as scatter plots with larger dots for MW-like galaxies, but colour encodes $\langle\text{Age}_{GCs}\rangle - \langle\text{Age}_\star\rangle$, with a black dashed line highlighting the 1-to-1 relationship. The lower panels display as a black curve the running Spearman rank correlation between the y-axes and color-coding parameters at fixed x-axis of each upper relationship (detail in text). The cleared area denotes $\{v_{rot}/\sigma_0\}_\star$ domains with significance (specifically p below 0.1) in the correlation (positive curve) or anti-correlation (negative curve) between the y-axes and color-coding parameter deviations at fixed x-axis value.

Kinematic properties

In this section we focus on the rotation-support diagnostic applied to both metal-split GC populations and to their comparison with the stellar rotation-support. From the analysis of velocity properties presented in the previous part, it can be expected that metal-rich GC populations trace suitably well the kinematics of the stellar galaxy content, contrarily to the metal-poor GC populations. Additionally, we look further in these relationships by comparing them with the difference between the average GC population's stellar age and the average galaxy stellar age.

Figure 5.4 shows those relationships in a left/right-column layout, with the left hand column illustrating the relationship between the metal-rich GCs and the field stars,

and the right hand column illustrating that between the metal-poor GCs and the field stars. Both upper panels display the relationship as a scattered plot in the same style as Figures 5.2 and 5.3 where dot sizes are larger for MW-like galaxies, and with the Spearman rank correlation coefficients and p-values in the upper left corner. GC properties are scaled on the y-axes while stellar properties are scaled on the x-axes, and dots are colour-coded according to the age-average differences between GCs and field stars $\langle \mathrm{Age_{GCs}} \rangle - \langle \mathrm{Age_\star} \rangle$. Additionally, those panels are completed with a black dashed line representing the 1-to-1 relationship.

Because the colour-coding of the upper row of panels reveals trends with the y-axis at fixed x-axis, we apply in the lower row of panels a graphic technique we will hereafter refer as "running Spearman rank" (also used in all 4 figures of Davies et al., 2019). This technique illustrates in a quantitative sense the significance of those trends: it does so by showing the profile of Spearman rank correlation coefficients between the variations in colour-coding and y-axis quantities over windows along the x-axis. Given the 3 quantities scaled by the x-axis, the y-axis and the colour-coding, we proceed as follows:

- First, we apply the LOcally WEighted Scatterplot Smoothing (LOWESS; Cleveland, 1979, 1981; Cleveland and Devlin, 1988) technique to get an estimate of the median profile of a parameter (either the y-axis or the colour coding) at fixed x-axis (here, the stellar rotation-support $\{v_{\mathrm{rot}}/\sigma_0\}_\star$). From the sample of (x_i, y_i), we obtain for each element a smoothed $\widetilde{y_i}$ estimated via a number of iterations of successive local weighted linear regressions. These regressions are done over a number of nearest neighbour elements in x_i values corresponding to a fraction of the full sample, and the weights are iteratively affected by the residuals from the previous iteration. In our case, we use a fraction of 20 percent of the full sample for the nearest neighbour elements, with 3 successive iterations.

- Then, after using the LOWESS technique on both the y-axes and the colour-coding properties, we obtain for each (x_i, y_i, c_i) element a pair of smoothed $(\widetilde{y_i}, \widetilde{c_i})$. We use them for computing the local running Spearman rank correlation

coefficients and p-value of a window of $(y_i - \widetilde{y}_i, c_i - \widetilde{c}_i)$ pairs of deviations. We choose this window to correspond to 50 elements (for consistency with the chosen 20 percent fraction of the full sample for the LOWESS method), and we obtain for a series of x-axis positions Spearman rank coefficients ρ_{Sp} and p-values.

We plot in the lower panel of each column the running Spearman rank coefficients obtained by application of this technique to the upper panel triplet of properties: on the left hand side column are shown $\{v_{\mathrm{rot}}/\sigma_0\}_\star$, $\{v_{\mathrm{rot}}/\sigma_0\}_{\mathrm{GCs}}^{\mathrm{Rich}}$, $\langle \mathrm{Age}_{\mathrm{GCs}} \rangle - \langle \mathrm{Age}_\star \rangle$ while $\{v_{\mathrm{rot}}/\sigma_0\}_\star$, $\{v_{\mathrm{rot}}/\sigma_0\}_{\mathrm{GCs}}^{\mathrm{Poor}}$, $\langle \mathrm{Age}_{\mathrm{GCs}} \rangle - \langle \mathrm{Age}_\star \rangle$ are shown on the right hand side column. We emphasize the correlations' significances by filling in grey regions where the p-values associated with the running Spearman rank is higher than 0.1, leaving cleared the parts of the curve where the correlation is significant.

As expected in comparing both upper panels, the rotation-support of the metal-rich GC populations exhibits a stronger correlation with that of the field stars than the metal-poor GCs. We observe a Spearman rank of 0.65 for the former relation against 0.27 for the latter. When reducing to the MW-like sub-sample, this difference is slightly more pronounced, with ranks of respectively 0.72 and 0.21. Focusing on the relationship between $\{v_{\mathrm{rot}}/\sigma_0\}_{\mathrm{GCs}}^{\mathrm{Rich}}$ and $\{v_{\mathrm{rot}}/\sigma_0\}_\star$, we note that the relation exhibits a significant scatter: at fixed $\{v_{\mathrm{rot}}/\sigma_0\}_\star$, there is a wide diversity of $\{v_{\mathrm{rot}}/\sigma_0\}_{\mathrm{GCs}}^{\mathrm{Rich}}$. The relation between this scatter and the difference of average ages between GC populations and field stars may hint at the explanation to this.

As illustrated by the colour coding, galaxies tend to exhibit lower rotational support in their metal-rich GC populations at fixed stellar rotation-support with higher $\langle \mathrm{Age}_{\mathrm{GCs}} \rangle - \langle \mathrm{Age}_\star \rangle$ i.e. when GCs are much older than the field stars. There is an anti-correlation between $\{v_{\mathrm{rot}}/\sigma_0\}_{\mathrm{GCs}}^{\mathrm{Rich}}$ and $\langle \mathrm{Age}_{\mathrm{GCs}} \rangle - \langle \mathrm{Age}_\star \rangle$ at fixed $\{v_{\mathrm{rot}}/\sigma_0\}_\star$, which is quantified in the lower panel: between, $\{v_{\mathrm{rot}}/\sigma_0\}_\star = 0.6$ and 1.6, the anti-correlation is significant. Outside of this range, there is no correlation: in the higher end, this is due to the poor sampling of the $\{v_{\mathrm{rot}}/\sigma_0\}_\star$ domain. For the lower end non-correlation, we can understand it from what the anti-correlation suggests: specifically that difference

of ages may drive the difference of rotation-support.

When a field star population is younger than its surrounding GC population, it is less likely to have converted its ordered motion into random motion from random gravitational encounters in comparison with the older surrounding GC population. With this aspect in mind, we can understand why the lower $\{v_{\mathrm{rot}}/\sigma_0\}_\star$ end does not show the same anti-correlation: high $\langle\mathrm{Age}_{\mathrm{GCs}}\rangle - \langle\mathrm{Age}_\star\rangle$ cannot populate the lower left corner of the $\{v_{\mathrm{rot}}/\sigma_0\}_{\mathrm{GCs}}^{\mathrm{Rich}}$ vs. $\{v_{\mathrm{rot}}/\sigma_0\}_\star$ relationship, and the non-correlation is reflective of the $\{v_{\mathrm{rot}}/\sigma_0\}_{\mathrm{GCs}}^{\mathrm{Rich}}$ noise for a galaxy population with $\langle\mathrm{Age}_{\mathrm{GCs}}\rangle \simeq \langle\mathrm{Age}_\star\rangle$.

Relative to the $\{v_{\mathrm{rot}}/\sigma_0\}_{\mathrm{GCs}}^{\mathrm{Poor}}$ vs. $\{v_{\mathrm{rot}}/\sigma_0\}_\star$ relation in the right column, we note from the lower right panel that their relation to the age difference shows no equivalent trend. While most of the $\{v_{\mathrm{rot}}/\sigma_0\}_\star$ range does not display significance in the running median, it includes only a narrow weak correlation range between $\{v_{\mathrm{rot}}/\sigma_0\}_\star = 0.6$ and 1.0. The colour coding of the upper scatter plot shows no sign of a trend either, so we conclude from this that the metal-poor GC population shows no significant kinematic link with the field star population.

Morphological properties

The morphologies and kinematics of stellar populations are fundamental properties that relate to each other often in a complex way. In the previous part, we have looked at the relation between kinematics of both metal-split GC populations with the field stars of E-MOSAICS galaxies, so we may wonder if such relations exist with morphologies. We investigate this question in this section, in a similar manner to the way it was done for kinematics.

Figure 5.5 represents our data as in Figure 5.4, but replacing the kinematics parameters with their morphological analogues. Similarly to the kinematic relationships, the morphology of metal-rich GC populations is correlated with the morphology of field stellar populations, with a Spearman rank coefficient of 0.64. Interestingly, the same relationship for the metal-poor GC populations presents a weak correlation with a Spearman coefficient of 0.45. The MW-like sub-sample presents slightly stronger correlations
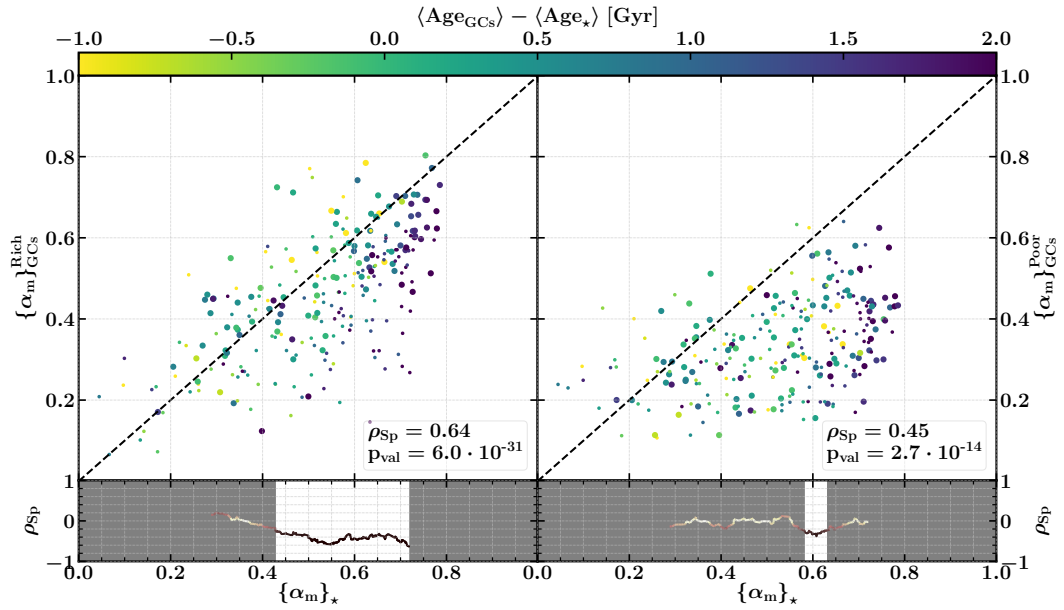
Figure 5.5: Relationship between the morphological parameter α_m of galaxy metallicity split GC and field star populations with the difference $\langle \text{Age}_{\text{GCs}} \rangle - \langle \text{Age}_\star \rangle$ between the GC and field star average ages. The layout and characteristics of this figure are identical to Figure 5.4 but representing morphological parameters α_m instead of kinematic parameter v_{rot}/σ_0.

of Spearman rank 0.75 for the former $\{\alpha_m\}_{\text{GCs}}^{\text{Rich}}$ vs. $\{\alpha_m\}_\star$ relationship, and of almost identical Spearman rank 0.46 for the latter $\{\alpha_m\}_{\text{GCs}}^{\text{Poor}}$ vs. $\{\alpha_m\}_\star$. Galaxy metal-rich GC populations remain suitably similar to their host galaxy in terms of their morphologies, but metal-poor GC population distributions appear to be also affected to a lesser extent.

The left column $\{\alpha_m\}_{\text{GCs}}^{\text{Rich}}$ vs. $\{\alpha_m\}_\star$ also presents a similar trend with the age difference $\langle \text{Age}_{\text{GCs}} \rangle - \langle \text{Age}_\star \rangle$. However, comparing the lower panels of both Figures 5.4 and 5.5 shows that this trend presents weaker correlations, with running Spearman rank evolving around $\rho_{\text{Sp}} \sim 0.4$ against 0.7 for the former case. Nonetheless, galaxies are more likely to have metal-rich GC populations that are more elliptically shaped than their field star populations if their GCs are older than their field stars on average. On the other hand, age difference trends in the $\{\alpha_m\}_{\text{GCs}}^{\text{Poor}}$ vs. $\{\alpha_m\}_\star$ relationship remain null.

Because our diagnostics are based on three-dimensional properties, we wish to investigate the way those morphological relationships behave from a projected point of view. In Figure 5.6, we plot 3 reproductions of the 2 upper scatter plots in Figure 5.5, but replacing the morphological parameter α_m by the projected flatness parameter ϵ_{proj}
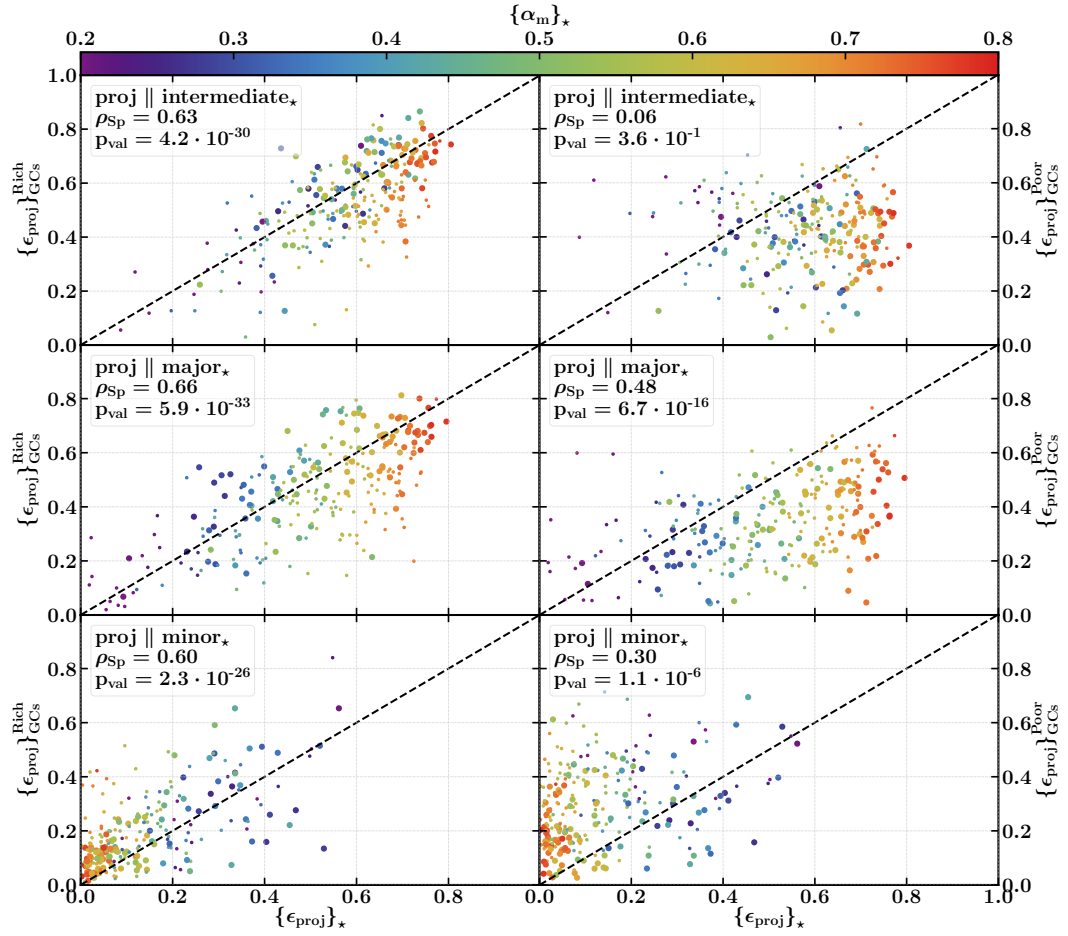
Figure 5.6: Relationship between the projected flatness parameter ϵ_{proj} along the intermediate (*upper row*), major (*middle row*) and minor (*lower row*) galaxy stellar axes, of metallicity split GC and field star populations, with the galaxy stellar 3-dimensional morphological parameter $\{\alpha_{\mathrm{m}}\}_{\star}$. Each row reproduces the layout and characteristics of the upper row of Figure 5.5, replacing the morphological parameters α_{m} by their projected flatness analogues ϵ_{proj} and the colour-coding by $\{\alpha_{\mathrm{m}}\}_{\star}$.

along each of the 3 stellar axes (see Section 5.2.2): along the intermediate axis in the upper row, along the major axis in the middle row, and along the minor axis in the lower row. Another way to appreciate these projections is the plane within which the flatness is measured: data in the upper, middle and lower rows consider respectively projections within the (minor,major)-axes plane, the (minor,intermediate)-axes plane and the (intermediate,major)-axes plane. We chose to represent these 3 projections only as they should be independent enough to generalize further results to any projections. Lastly, the colouring does not encode the age difference as per Figures 5.4 and 5.5 but the stellar morphological parameter $\{\alpha_{\mathrm{m}}\}_{\star}$ to illustrate the effect of triaxiality.

We note that once again, the left hand side column, representing relationships between metal-rich GC and field star population properties, shows strong correlations, while the right hand side column, showing relationships between metal-poor GC and field star analogues, presents weak to no correlations. In particular, all left hand side panels have scattered samples following the 1-to-1 dashed line, with Spearman rank coefficients of respectively 0.63, 0.66 and 0.60 for the upper, middle and lower panels. On the other hand, results in the right hand side column show a variety of Spearman rank coefficients: the upper panel is the weakest, at 0.06, revealing no correlation, with the middle panel being the strongest, at a 0.48 value, closer to its 3-dimensional 0.45 analogue in Figure 5.5. In summary, one can then expect that the relation between the morphologies of metal-rich GC and field star populations should be similar along any projection.

Because of the choice of projections shown in each row, it should be expected that flatness from the upper row should be larger than that from the middle row. Indeed, if we refer to $a > b > c$ the major, intermediate and minor axes, upper row flatness should be close to $1 - c/a$ and middle row flatness to $1 - b/a$. This results in a larger spread of ϵ_{proj} values in the middle row, leading to the higher Spearman rank coefficients these panels present. Additionally, the colour coding appears almost identical between the 2 upper rows, following the stellar ϵ_{proj} progression, while it is found reversed in the lower row. The 2 upper rows present flatness measured in 2 independent edge-on views, while the lower row presents the face-on projections. In this latter projection,

the highest α_{m} corresponding to disk systems should show projected flatness ϵ_{proj} near zero because of the strong circularity of disks. On the other hand, low α_{m} corresponds to ellipticals, with a significant fraction of prolate galaxies presenting stronger flatness in their 'face-on' view.

5.3.3 Morpho-kinematic relationship

We focus in this Section on the relationship between the metal-rich GC and field star population properties. Notably, we observed in Section 5.3.2 that kinematic diagnostics offer a stronger link than the morphological analogues between these 2 populations. This opens a question on the relationship between these 2 diagnostics in both populations. As shown in Chapter 4, theoretical work from Binney (1978) and Binney and Tremaine (1987) revealed that for gravitationally bound oblate, axisymmetric systems rotating about their short axis, the relation between morphology and kinematics depends on a third parameter, namely, the anisotropy of that system's velocity dispersion. We also noted that in the case of the stellar content of a galaxy, its anisotropy is correlated with both the flatness of the associated inner dark matter halo, and of the inner halo from counterparts identified in a simulation of the same volume, at the same resolution, but considering only collisionless gravitational dynamics (DMONLY). We investigate if these trends are found in the field stars, as well as metal-rich GC populations, of the E-MOSAICS galaxies via Figure 5.7.

Figure 5.7 presents the relationship between the rotation-to-dispersion ratio and the morphological parameter for the field stars in the left hand panel and metal-rich GC populations in the right hand panel. The y and x-axes of each panel scales respectively the rotation-to-dispersion ratio $v_{\mathrm{rot}}/\sigma_0$ and the morphological parameter α_{m}. Similarly to previous figures, our sample is represented as a scatterplot with larger dots highlighting the MW-like sample. The colour-coding encodes the velocity dispersion anisotropy of the population represented in the panel.

Examining the left panel and the relation for field stars, we note a trend in anisotropies similar to that found in the EAGLE simulation in Chapter 4. When applying the
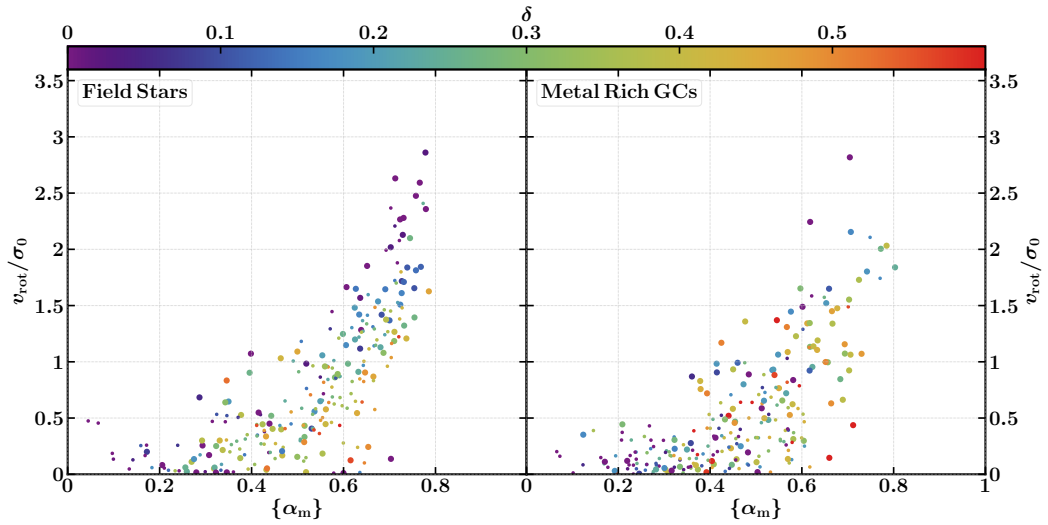
Figure 5.7: Relationships between the morphological parameter α_m and rotation-to-dispersion ratio v_rot/σ_0 with the dispersion anisotropy δ for populations of field stars - left hand panel - and metal-rich GCs - right hand panel. Sample is represented as a colour-coded scatter-plot, with dots of larger size for the MW-like sub-sample, and colour encoding the dispersion anisotropy δ. α_m and v_rot/σ_0 are respectively scaled along the x and y axes.

LOWESS technique to estimate deviations from the median α_m at fixed v_rot/σ_0, we find a Spearman rank coefficient of 0.41 between these deviations and the anisotropy values. This value corresponds to the full sample; if we apply the same cut as in Section 4.2.3 to isolate spheroidal and rotationally aligned oblate galaxies[3], we get a higher coefficient of 0.60. This shows good agreement with the previous trend of Section 4.2.3, Figure 4.4. Given that E-MOSAICS has a mass resolution 8 times higher than EAGLE, this confirms that this trend shows good convergence.

On the other hand, the right panel of Figure 5.7 presents the same relation for metal-rich GC populations. While the field star populations showed a trend in δ in their morpho-kinematics space, metal-rich GC populations do not appear to present one. Using the same LOWESS technique to estimate deviations from the median α_m at fixed v_rot/σ_0, those deviations show poor correlation with δ, with Spearman rank coefficient of 0.28 (or 0.38 for spheroidal and rotationally aligned oblate galaxies).

A reason for this difference is that the theoretical framework of Binney (1978) and Binney and Tremaine (1987) links the motion characteristics of a self-gravitating sys-

---

[3]$\epsilon_\star < 0.3$, or $T_\star < 1/3$ with the geometric angle between the minor axis and the angular momentum below 10 degrees.

tem to the shape of its potential, instead of the shape of a sub-system such as the stellar population or metal-rich GC population. In the case of field stars, they often contribute significantly to the material content in the central galactic region, and thus the potential, and our morphological parameter favours (by design) the material at the centre. Therefore, in a first approximation, it is likely that field stars will satisfy this theoretical framework (with a 2nd order perturbative trend due to the dark matter shape as shown in Section 4.3.2). On the other hand, metal-rich GC populations do not contribute significantly to the potential: stated differently, it is unlikely that their shape should show a similar trend to their motion characteristics.

5.4 Summary and discussions

We have examined the morphological and kinematic properties of various globular cluster and field star populations from galaxies of the E-MOSAICS simulations. As part of the analysis, we also investigated the relation between the morpho-kinematic properties of metal-rich GCs and field stars, linking with our results of Chapter 4. We study a sample of 255 present-day central galaxies with stellar masses $M_\star > 10^{9.5}$ M$_\odot$, composed of a sub-sample of 105 galaxies with MW-like virial masses M_{200} ranging between $7 \cdot 10^{11}$ and $3 \cdot 10^{12}$ M$_\odot$. Our results can be summarized as follows:

1. GC system demographics are diverse due to the large range of stellar masses, with 28 to 5848 GCs per galaxy, a majority of which are composed of 17 percent or less of metal-poor GCs. This results in GC systems showing similar morphological and kinematic properties to their metal-rich sub-population, both being widely diverse. We note that this fraction is lower than is often estimated for observed GC populations (Peng et al., 2006); this is primarily owing to the (known) under-disruption of metal-rich GCs in E-MOSAICS (Pfeffer et al., 2018). In any case, one may also consider our choice of metallicity threshold at [Fe/H] $= -1$ to be somewhat arbitrary. Nonetheless, metal-poor and metal-rich GC systems show, respectively, more elliptical/dispersion-supported and

disky/rotation-supported morphologies/kinematics than the complete GC systems (Fig. 5.1).

2. A detailed examination of the relationship between the velocity dispersion of metal-rich GC, metal-poor GC, field star and dark matter systems reveals that all correlate to some degree, and tend to show good agreement with SLUGGS observational trends shown in Pota et al. (2013). The correlation is strongest between the metal-poor GC and dark matter dispersions, which exhibit a Spearman rank of 0.94. Also, both of the latter velocity dispersions correlate significantly with the galaxy stellar mass, with Spearman ranks of respectively 0.92 and 0.96 for metal-poor GC and dark matter systems, against 0.77 and 0.87 respectively for field star and metal-rich GC systems (Fig. 5.2).

3. While the velocity dispersions of all 4 components show good correlations, analyzing their characteristic rotational velocities reveals different trends, with only metal-rich GC and field star velocities correlating (Spearman rank of 0.70). Nonetheless, this also shows good agreement with Pota et al. (2013) SLUGGS observational trends despite the large measurement uncertainties (Fig. 5.3).

4. As for the trends presented for the velocity dispersion, the rotation-to-dispersion ratios replicate trends seen for the rotational velocity, with metal-rich GC and field star ratios correlating, contrary to metal-poor GC and field star ratios (Spearman ranks of respectively 0.65 and 0.27). This correlation exhibits a wide scatter, which correlates with the difference of average age between GC and field star systems: at fixed $\{v_{\rm rot}\}_\star$, metal-rich GC systems exhibit more dispersion-support when GCs are older than field stars (Fig. 5.4).

5. Likewise, the morphological parameter of metal-rich GC systems is similarly correlated to that of the field stars (Spearman rank of 0.64), with a similar but slightly weaker gradient in GC - field star age differences. On the other hand, the morphological parameter of metal-poor GC systems displays a weak correlation with that of the field stars (Fig 5.5). Both relationships appear to be followed closely even when using projected flatness along the 3 independent axes of the

field stars' ellipsoidal representation (Fig. 5.6).

6. Both metal-rich GC and field star systems have their morphological and kinematic properties well correlated at high rotation-to-dispersion ratio, but scattered at lower ratio. However, while field star properties reproduce the morpho-kinematics relationship shown in Chapter 5 with the dispersion anisotropy, metal-rich GC properties do not exhibit a similar trend (Fig. 5.7). This is likely due to the non-contribution of metal-rich GCs to the gravitational potential, unlike field stars.

Our finding that metal-rich GC systems tend to resemble field star properties in both morphologies and kinematics, as has been shown in observational measurements, is a strong corroboration of the E-MOSAICS simulations. It echoes with the recent years of globular cluster observational searches and the findings of various studies (Lee et al., 2010; Strader et al., 2011; Park and Lee, 2013; Pota et al., 2013). But the E-MOSAICS simulation enables a deeper understanding of trends previously shown in observations. In particular, our finding that the GC - field star age difference affects the efficacy with which metal-rich GC properties mimic those of the field stars broadly corroborates the current prevailing scenario for metal-split rich-in-situ/poor-ex-situ GC formation.

Indeed, having a GC system older than field stars allows a wider diversification of kinematics towards the dispersion-supported end for metal-rich GC systems with respect to the kinematic type of field stars. That diversification depends on the extra time GCs had for their motion to dynamically heat compared to that of the field stars. metal-poor GC systems do not show such a trend on the other hand, due to their formation being preferentially at earlier times (likely in previously merged galaxies), making such trend unlikely to appear.

This work leaves open a question on the morpho-kinematic situation of these metal-poor GC systems. We concentrated our focus on the relationship between GC and field star system morphological and kinematic properties. But it is likely that, considering the accreted scenario for populating galaxies with metal-poor GCs, the latter could show some relation in morpho-kinematics with the dark matter halo. This conjecture

could fuel future investigations.

Chapter 6

Conclusions and future works

Galaxies result from an intricate cosmological evolution mixing gravitational interactions and fluid dynamics with a rich diversity of baryonic processes (Chapter 1). Such complex and interleaved physics influencing their formation requires us to develop, run and analyze numerical simulations that compute those interactions together in a self-consistent way (Chapter 2). Through this thesis, we looked at such simulations to study the morphology and kinematics of galaxies, dark matter haloes and globular cluster populations, motivated by the fact that those properties are fundamentally tied to the formation history of the host galaxy. Examining their diversity and understanding their origin is an essential step towards a better comprehension of galaxy formation. As observational surveys are getting access to an ever-wider catalogue of objects, ever more distant and with ever more detailed morpho-kinematics mapping, it is a perfect time to develop predictions related to those properties. In particular, as simulations are becoming more realistic, they have become an indispensable tool with which to formulate and test theoretical ideas. With the predictive power of the EAGLE model, we looked at the relationships between galaxy morpho-kinematics and galaxy colour (Chapter 3), between galaxy morphologies and kinematics, with respect to the dark matter halo shapes (Chapter 4), and between the morpho-kinematics of galaxy globular cluster and field star populations (Chapter 5). We summarize below the discussion presented in this thesis (Section 6.1) and suggest some questions that this work opens

up (Section 6.2).

6.1 Summary

In Chapter 1, we introduced the context of the work of this thesis. After a brief summary of the various achievements that shaped extra-galactic astrophysics through the 20th century, we presented the current cosmological paradigm, the ΛCDM cosmogony, in particular its historic construction and its 3 key evidential foundations. This allowed us to introduce various crucial aspects of the formation of galaxies for our work, namely their hierarchical formation, their internal star formation and their feedback processes. Lastly, we discussed core concepts in relation to the morpho-kinematics of self-gravitating systems and the necessity of numerical simulations to investigate them.

From this introduction we moved in Chapter 2 to a brief introduction to cosmological simulations with particular attention to those that we use in this thesis. We started with an overview of the generic structure of current state-of-the-art projects, detailing their crucial elements, notably the widely used N-body TreePM gravity solver and the smoothed particle hydrodynamics method for solving the fluid equations, as well as an overview to the concept of subgrid physics. In the second part of Chapter 2, we introduced in more detail the simulation projects EAGLE and E-MOSAICS, on which our analyses are based. Lastly we described the criteria with which we define a galaxy in those simulations and the main criteria defining our samples.

In Chapter 3 we discussed the relation between morphologies and internal kinematics with the colour of a galaxy. We first presented some elements of theory on the morphologies and kinematics of self-gravitating systems, and used them to establish definitions of the parametric tools we use throughout this thesis. Notably, we developed the framework presented by Binney (1978) and Binney and Tremaine (1987) linking the shape and dynamics of oblate galaxies. We then introduced our methods to measure the flatness and the triaxiality of a system, using the scale-lengths of the quadrupole moments of the mass distribution, and looked at how EAGLE galaxies

are described by these two parameters. We then presented various parameters used in simulations to characterise galaxies' internal kinematics and compared them to the rotation-to-dispersion technique we use throughout this thesis, a technique that also provides a measure of the disperson anisotropy. We apply these diagnostics to a sample of central galaxies with stellar masses larger than $10^{9.5}$ M$_\odot$ drawn from the largest EAGLE simulation ($100\,\mathrm{Mpc}$).

We showed that our sample of EAGLE galaxies exhibit a wide diversity of morphologies, with spheroidal, oblate and prolate galaxies. In particular, most of the sample present oblate morphologies which are characteristic of "disky" galaxies. Thereafter, we found that the 5 methods used for measuring rotation-support in simulated galaxies yield remarkably consistent impressions of their internal kinematics, with strong correlations between them. This suggests that they can be used interchangeably, and in our case we used the rotation-to-dispersion ratio from there for its connection with the theoretical framework we discussed, and the use of the dispersion anisotropy. Lastly, we investigated the relation between these morphological and kinematic parameters and the colour-stellar mass diagram. We notably found that while kinematic parameters appear to separate suitably the red sequence and blue cloud through a single rotation-support measure, morphological parameters require more complexity as both flatness ϵ and triaxiality T are needed. This led us to define a new parameter $\alpha_{\mathrm{m}} = (\epsilon^2 + 1 - T)/2$ which proved to perform an equally effective separation of the colour split in the galaxy population.

Investigating the relation between morpho-kinematics and the colour-stellar mass diagram motivated the investigation of the relation between morphologies and kinematics. Indeed, both have long been assumed to be correlated such that rotation-supported and dispersion-supported systems respectively correspond to flattened and spheroidal galaxies. Questioning this correlation has become even more important now that the deployment of integral field spectrographs for panoramic surveys has become widespread. Moreover, this correlation had been at the basis of a general practice for assessing the morphologies of simulated galaxies from their kinematics, as particle dynamics are simple and unambiguous to compute.

We looked precisely at this relationship through Chapter 4, employing the theoretical groundwork developed in Chapter 3 through our set of morpho-kinematics parameters. We revealed a tight correlation between ellipticity and rotation-to-dispersion ratio for rotation-supported galaxies, but exhibiting a wide scatter in the dispersion-supported regime. The origin of this scatter is investigated via two distinct avenues, one of them being the existence of prolate galaxies, occasionally rotationally misaligned, whose flatness may not be related to their internal kinematics. The second, and dominant, contribution to this scatter (65 percent of the sample) is through spheroidal and rotationally-aligned galaxies. Such systems are at the core of the theoretical groundwork of Binney (1978) and Binney and Tremaine (1987) with the predicted relationship between the morpho-kinematics scatter and the velocity dispersion anisotropy. We find that our sample of simulated galaxies reproduces this relationship faithfully: galaxies are more flattened at fixed rotation-support if a greater fraction of their velocity dispersion is confined to motion in the plane of the disk, rather than in the direction of the angular momentum.

The velocity dispersion anisotropy is intriguing as it relates to a difference of dispersion intensity along 2 directions. The origin of this difference was assessed in the second half of Chapter 4. Acknowledging the plausible influence of the shape of the potential in driving this morpho-kinematic relation, we characterised dark matter halo shapes with the same technique used to characterise galaxy morphologies. Comparing this property with the $v_{\rm rot}/\sigma_0$ - ϵ diagram, we observed an equivalent trend to that observed with the dispersion anisotropy: that galaxies at fixed rotation-support exhibit more flattened/spheroidal shapes if their dark matter inner halo is more flattened/spheroidal too. This suggests a causal relationship, with the inner halo shape influencing the galaxy shape via stellar dynamics, but to confirm that possibility, we needed to "remove the baryons" from the picture.

Since simulations are built in a modular fashion, it is trivial to remove baryonic physics, leaving only the collisionless dynamics of dark matter. Starting from identical initial conditions, we can evolve a virtually identical dark matter only (DMO) Universe in which halos are equivalent to those of the main simulation, but do not feel the effect of

baryons. The shape of such haloes can thus be considered "intrisic", specified by the initial conditions of the early Universe. By comparing galaxies' morpho-kinematics with these intrinsic halo shapes, we observed an equivalent trend to that with the baryon-influenced halo shapes. Moreover, we also revealed that both trends for intrinsic and baryon-influenced halo shapes could be linked to the dispersion anisotropy in a correlated fashion. A conclusion from this is that the present-day dispersion anisotropy has its origin partly in the shape of the dark matter inner halo.

The tools developed in this thesis are valuable additions to the simulator's toolkit and can serve the many spin-off projects that uses the EAGLE model as a basis. One such project is the E-MOSAICS simulation, which adds to EAGLE a model for formation and evolution of globular clusters. Recent years have seen a substantial research effort devoted to the study of galactic and extragalactic globular clusters and their potential to reveal galaxy assembly histories. The prevailing scenario for the formation of globular clusters establishes 2 routes, leading to different metallicity signatures within these objects, with metal-rich signatures generally corresponding to in-situ formation, whilst metal-poor signatures are assumed to signal ex-situ formation. Our work in Chapter 5 contributes to this effort: by applying the tools we developed to a similar sample of galaxies from the E-MOSAICS simulations, we study the morpho-kinematic properties of metallicity-split[1] globular cluster systems relative to that of the field stars in galaxies.

Looking at their globular cluster demographics, we find that our sample of galaxies host diverse populations of globular clusters, although those that are metal-rich appear to dominate in each galaxy's globular cluster populations. Their morpho-kinematics are diverse with a tendency for metal-poor and rich systems to diverge respectively towards the elliptical/dispersion-supported and disky/rotation-supported ends. Analyzing the velocity characteristics of both metal-split populations reveals that the rotational motion of metal-rich globular cluster populations resembles that of the field stars, despite the field stars and both metal-split GC systems (as well as the dark matter halo) sharing identical dispersion motions (those dispersions appearing strongly correlated with the hosting galaxy stellar mass). On this basis, by comparing the rotation-

---

[1]threshold at $[\mathrm{Fe/H}] = -1$

to-dispersion ratios of each systems, we find that metal-rich globular cluster and field star internal kinematics are well correlated, while metal-poor globular cluster systems show no correlation with the latter. This is qualitatively (and to some degree quantitatively) in agreement with observational measurements. This relationship also has a strong dependency on the difference of ages between globular clusters and field stars.

Similarly, metal-rich globular clusters also appear to share more comparable shapes to the galaxy they inhabit than the metal-poor globular clusters, both in 3-dimensions and in projection, exhibiting an equivalent trend with the globular cluster - field star difference of ages. This proxy property in morpho-kinematics supports the scenario that metal-rich globular clusters are more likely to have formed in the main progenitor of their galaxy rather than having been accreted through extragalactic encounters. Interestingly however, while field star morpho-kinematics echo the relation previously found with their dispersion anisotropy, metal-rich globular cluster morpho-kinematics do not, despite exhibiting similar kinematics to their galaxy's disc. This corroborates the idea that the theoretical framework of Binney (1978) and Binney and Tremaine (1987) should not be expected to apply to all morpho-kinematic relationships equivalently. In particular, it only applies to systems that are self-gravitating.

6.2 Future directions

The work presented in this thesis opens paths to future research directions. Below, we suggest means by which our investigations might be extended, and also highlight forthcoming projects to which the tools presented here might be applied.

6.2.1 Expanding our results

Among our results we summarized in Section 6.1, some particularly raised our interest. For instance, when studying the relationship between the morphology and kinematics of galaxies we noted the existence of galaxies with prolate morphologies exhibiting

rotation around their major axis (Section 4.2.2). These so-called "prolate rotators" have recently been detected in integral field surveys (Tsatsi et al., 2017), but little is known about their origin. The most likely cause for their formation seems to be through very particular merging configurations. A route that may lead to a better understanding of these peculiar systems would be to isolate our cases found in the EAGLE simulation, and examine their merger history.

On a similar subject, we ignored a small population of flattened systems whose morphologies were purely triaxial, that is with triaxiality near 0.5. Indeed for staying within our theoretical framework, it was necessary to examine only galaxies with a high degree of circularity (equal major and intermediate scale lengths). We believe such systems may feature nuclear bar structures which the EAGLE model successfully produces (Algorry et al., 2017). Also, as a more general view, it would be interesting to examine how our morphological diagnostics reflect the existence of a bar. In particular, it may be the case that some of those we identify as prolate may be so because of a bar, since the inner structure has more weight in the reduced inertia tensor technique. It is important to mention that, consequently, bars may also have an influence on the dynamical heating and the dispersion anisotropy.

An important question we wish to assess is that of the proxy ability of metal-poor globular cluster systems to reveal the morpho-kinematic properties of the dark matter halo. Indeed, since those clusters likely find their origin through the accretion of material via extragalactic gravitational encounters, it is assumed that they tend to populate the outer part of the galaxy, following the halo potential. During the course of this thesis, we had a chance to start investigating this question, and found some positive leads. We notably found a weak correlation between the morphology, quantified as per Fig. 5.5, of metal-poor globular cluster systems and the dark matter inner halo. However that relation featured a large scatter around the correlation trend; in order to better understand the origin of this trend, it would be instructive to establish what drives this scatter.

6.2.2 Exploiting our tools

The tools developed through this work have the benefit of being versatile, and perfectly suited for any EAGLE-like simulation. This was notably a particular advantage for our study of globular cluster systems' morpho-kinematics via the EAGLE-spin-off project E-MOSAICS. In conjunction with this, many other such spin-off projects exist or are under development which may require morpho-kinematic tools. In our case, we are interested in 2 potential future projects which could be of direct interest for improving the results shown in this thesis.

One of them is named EAGLE-XL; it aims to reproduce the observed galaxy population with ever better fidelity than EAGLE, and within a volume a factor of ~ 30 greater. Typically, while the largest volume in the EAGLE suite of simulations has a box size of $100\,\mathrm{Mpc}$, EAGLE-XL should increase that length to $300\,\mathrm{Mpc}$. This directly offers markedly superior statistics and enables searches for 'rare' objects. With a larger number of galaxies, it is possible to access relations that could not be reached with the EAGLE box. Notably, the lack of statistics prevented us from exploring fully the variation of the relation between morphologies and kinematics for more defined mass ranges. Such a larger volume would allow this.

As we discussed in Section 2.3.1, the EAGLE model does not explicitly resolve the cold, dense phase of the ISM. This results in simulated disc galaxies being artificially thicker than their counterparts in nature. With the aim to improve other shortcomings of the model, the EAGLE collaboration are now working on a project known as COL-IBRE. Among the improvements that are proposed, revamping the modelling of the cold, dense phase of the ISM is a key part of their agenda. Naturally, it would be interested to see how our results differ with this new simulation, with galaxies populating much thinner morphologies.

Appendix A

Rendering cosmological simulations

As simulation data are usually generated in binary format, their interpretation require to be done by processing them, altering them to compute representative measurable quantities, allowing the analysis of potential correlations. But another way to ease the interpretation is to render the simulated phenomena, for scientific or recreational purpose, especially by producing flyby movies within the simulated Universe in the case of computational cosmology. During a previous student experience in the summer 2014 with the University of Victoria, Canada, software was developed using the PYTHON package PY-SPHVIEWER (Benítez-Llambay, 2015) to allow in an ergonomic way the computation of such movies with customizable trajectories from GADGET3-made simulations (some frames of these movies[1] are shown in figure A.2). We have used this software, and upgraded it if necessary, to prepare and provide media contents for the outreach activities of the Astrophysics Research Institute (ARI), and to contribute to the press release that accompanied the publication of Oppenheimer et al. (2016).

---

[1]available here: `https://vimeo.com/278487892` for dark matter, `https://vimeo.com/278494116` for gas, and `https://vimeo.com/278494665` for stars

A.1 Software development

A.1.1 PY-SPHVIEWER renderer

The software manipulates the PYTHON package PY-SPHVIEWER (Benítez-Llambay, 2015) which renders N-body + Hydrodynamics simulations with smoothed particles in 3 steps, with 3 specific PYTHON implemented classes of objects, `Particle`, `Scene` and `Render`, which interface multi-threaded C-native routines.

- `Particle` prepares a framework of any number of smoothed particles when given the coordinates and the masses of all these particles. It computes the smoothing lengths associated to these particles via a distributed k-Nearest Neighbor Search (kNNS) algorithm in which k can be given as a parameter. As this process is time consuming, if these smoothing lengths are already known, they can be given to the object as an input to limit unnecessary computation.

- `Scene` uses the `Particle` object to prepare the scenery, given a `Camera` object for which the parameters are the 3 coordinates of its target, the 3 panning/tilting/rolling camera angles defined according to the Tait-Bryan $x - y' - z''$ intrinsic rotation fashion, the zoom of its field-of-view (FoV) and its horizontal and vertical pixel-resolution. It isolates the particles that can be seen into the related FoV and computes their projected coordinates and smoothing lengths.

- `Render` finally uses `Scene` to produce the raw array of intensities pixel by pixel that are viewed in the `Camera` FoV by summing all the projected smoothed particles. It has an optional native logarithmic scale that can be applied but we choose to not use it, and apply our own logarithmic scale.

PY-SPHVIEWER is a fairly simple and intuitive package to use, but produces only images and not videos yet; the software we detail in this appendix acts, in the context of GADGET3-style outputs, as a wrapper of PY-SPHVIEWER to temporarily address this need in wait of further development of the package (and for potential contributions to it).
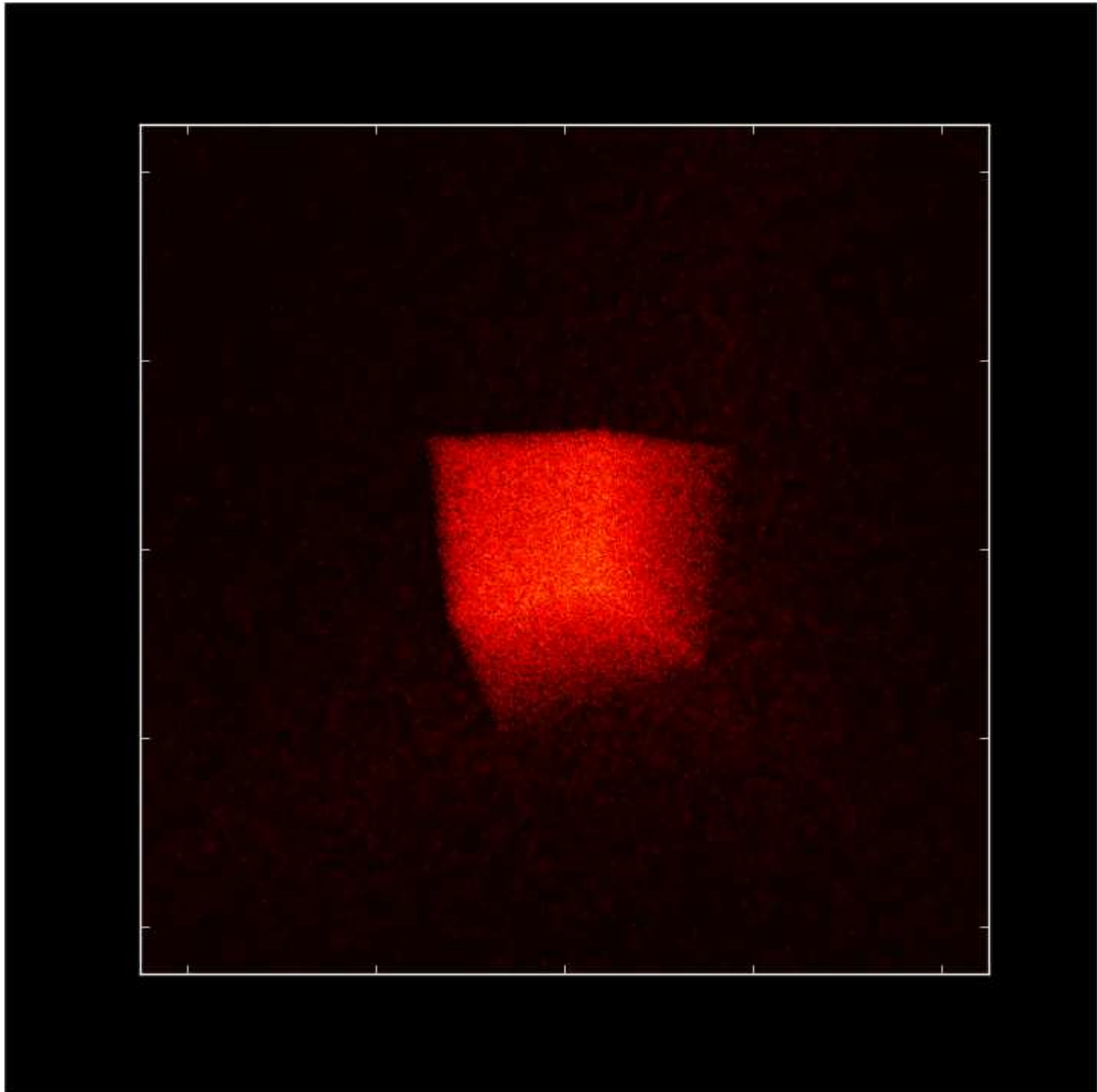
Figure A.1: Illustration of PY-SPHVIEWER rendering performance by rendering 100000 identical particles, randomly positioned in a uniform 3D box, and duplicated in an environmental stretched box to produce a background of particles in which the initial particle-made box is immersed.

A.1.2   Main scheme & and recent improvements

The wrapper runs through 5 major steps, leading to the encoding of the movie in an exploitable format (with a configurable framerate and image resolution):

- *Volume structure:* The first step is a preliminary exploration of the file system, having been given the root path where all the GADGET3 and SUBFIND outputs are saved. It knows the syntax of file names of that structure (with the possibility to adapt to any custom naming), and it creates a redshift sorted list of PYTHON flag-objects that can be used to load arrays of data. It is also able to distinguish snapshot and snapshot outputs (more details of this distinction in section 3 of Schaye et al., 2015). In case the user requires additional data that are associated to the particles but available in other files, as long as those adopt a similar file structure, they can be added "on-the-fly" as a new list of PYTHON flag-objects consistent with the resdhift sorting of the main list.

- *Halo tracking:* Although limited by the necessity to manually input the arrays of subhalo position coordinates per snapshot prior to this PhD project, the halo tracking now takes into account merger trees publicly made available online by the EAGLE collaboration (McAlpine et al., 2016; Qu et al., 2016). However, it is also possible to provide any other target tracking as a list of coordinates per snapshot. Once these are known, the software adapts them first to the snipshots by linear interpolation of their values. Then, it filters those trajectories with a Butterworth (1930) low-pass discrete filter calibrated on the framerate to avoid tracking that would be visually erratic (a switch parameter can be activated in the tracking smoothing to take into account cyclic boxes - i.e. with periodic boundary conditions). All considered haloes have an associated integer *id* for identifying them in the next step, and their filtered trajectories are stored in a list of halo tracking tables accordingly sorted by identified haloes.

- *Suretarget:* The last step before movie production consists of describing the camera behavior and the choice of snapshot/snipshot for evolution movies. For this, a function has been implemented (inspired by the graphic interface of the

software Adobe After Effects [2] and the independent preset Suretarget [3]) to pro-
duce smoothed interpolated trajectory parameters and to choose relevant snap-
shots/snipshots from custom time-lined "anchor-points". These "anchor-points"
are each associated with a specific movie frame *ids* and fix one or more param-
eters among the following: the redshift to explore, the subhalo to target, the
distance to the target, the 3 panning/tilting/rolling angles and the zoom of the
camera. The function treats first the redshifts, modifying the number of frames
between the anchor points if needed (EAGLE is limited by 400 snipshots/28 snap-
shots), and then, using the halo tracking tables at the right redshift, it interpolates
and filters, with the same Butterworth (1930) low-pass filter, the other parame-
ters to get the final exhaustive evolution of movie parameters.

- *Frame rendering:* These parameters are then loaded in a routine that exploits
  PY-SPHVIEWER with the volume data structure produced in step 1 to gener-
  ate the raw arrays of intensity at each frame of the particles of a chosen type
  (Dark Matter, Gas, Star or Black Hole). Knowing the data structure of GAD-
  GET3 files, it uses the coordinates and masses of particles of the chosen type,
  and if available, the associated smoothing lengths. GADGET3-made simulations
  often describe the mass of sub-components of a specific type, such as chemical
  enrichment in gas particles, as fractions of the particle mass, the routine can ren-
  der that sub-component if the path to that fraction in the data structure is given
  as input. Similarly, the routine can replace all-together the mass used for render-
  ing by another quantity of the user's choice if the path to that quantity is given
  as input. The routine considers also optional features like cyclic boxes (i.e. pe-
  riodic boundary conditions), spherical apertures, quadratic fading with distance
  of particle intensities, smoothing length cap, stereoscopic 3D movie production.
  These arrays are then saved on the local data storage for the next last step.

- *Video making:* Finally, the raw images go through 3 layers of video processing
  before being saved in a final image format, and encoded together in a single

---

movie: First, statistical analysis is made on each image (in order to avoid images to have their dynamic - i.e. their distribution of pixel intensities - to be too skewed) to find proper logarithmic pivot values p_i, that are averaged together to find the logarithmic scale $x_{\log} : X \longmapsto \log\left(\langle p_i \rangle + X\right)$ that is uniformly applied to all images; Then, applying this logarithmic scale, it generates a list of minimum and maximum thresholds, here again statistically estimated, to keep an appreciable dynamic range of the image, and smooths these 2 lists of threshold values through the same Butterworth (1930) low-pass filter. The final step applies a raised cosine scaling function to the log-scaled intensities, after their normalization and clipping according to the minimum and maximum thresholds, to enhance the dynamic contrast before saving the image with a pre-chosen colourmap.

$$x_{\text{norm}} = \left[\frac{x_{\log} - x_{\log}^{\min}}{x_{\log}^{\max} - x_{\log}^{\min}}\right]_{\to 0}^{\to 1} \in [0,1] \longmapsto \frac{1}{2}\left(1 + \sin\left(\pi(x_{\text{norm}} - 0.5)\right)\right) \quad \text{(A.1)}$$

Once all images are generated in a convenient image format (generally Portable Network Graphics/PNG for a lossless compressed format or Tagged Image File Format/TIFF for a deep-color format), they are encoded using the free suite of software FFMPEG[4].

A.2 Extrinsic applications

A.2.1 Oppenheimer et al. (2016) Press release

Our collaborators Oppenheimer et al. (2016) were given the opportunity of a press release associated with the publication of their research in the Monthly Notices of the Royal Astronomical Society. To enhance this press release, we produced movies of 2 of the 20 simulated halos that this research generated: a spiral and an elliptical galaxy. We produced flyby movies of 4 components: dark matter, gas, star, and the

---

[4]`https://www.ffmpeg.org/`
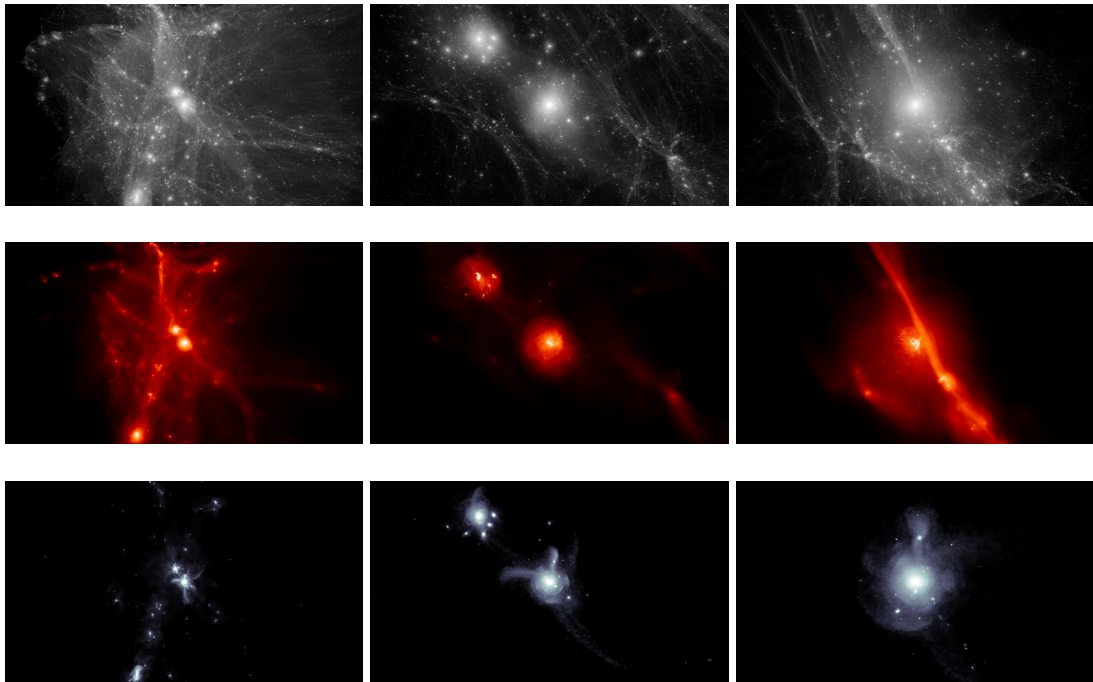
Figure A.2: Frames from the $z = 0$ flyby movies produced during the original project that led to the development of the software. The movies render the Local-Group alike volume V1 from the APOSTLE project (Fattahi et al., 2016; Sawala et al., 2016). The upper, middle and lower rows respectively represent the dark matter, gas and star components. The left, centre and right columns represent distances from the camera to the main target - the main galaxy - of respectively 36.8 Mpc, 8 Mpc and 3.6 Mpc.

ionized oxygen component. For each halo, we made available[5] the 4 single component movies, a blended version of the gas and stars (with gas as an alpha channel with 40% of transparency), and a quad-view with all 4 components being shown in each corner of the same video file (screens are shown in figure A.3). The press release and our media were featured in international media and on the front page of the LJMU website[6].

A.2.2 Fiske planetarium demonstration

Our collaborators at the Fiske planetarium of the University of Boulder, Colorado, had the ambition to produce an outreach projection of the formation of a galaxy. Using a simulation with high resolution in cosmic time, we used our software to generate such

---

[5]quad-view movies are available here `https://vimeo.com/279215687` for the elliptical galaxy and `https://vimeo.com/279215384` for the spiral galaxy

[6]`https://www.ljmu.ac.uk/about-us/news/wasteful-galaxies`
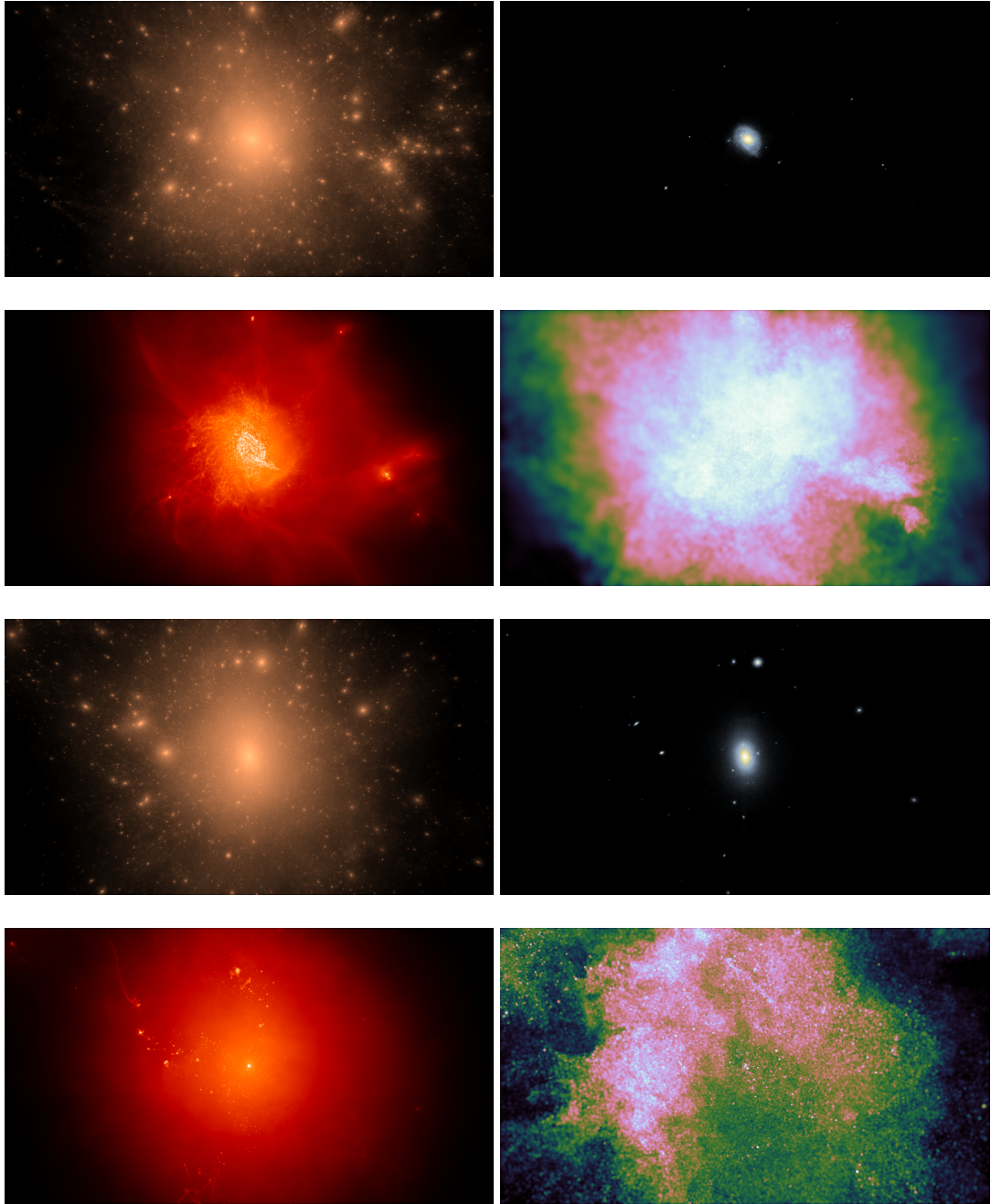
Figure A.3: Frames from the rendering movies of 2 halos from Oppenheimer et al. (2016). Upper 4 panels represent the spiral galaxy while the lower 4 panels represent the elliptical galaxy. In each set of 4 panels, the upper left is the dark matter component, the upper right is the star component, the lower left is the gas component and the lower right is the ionized oxygen VI component.

movie. However, since PY-SPHVIEWER does not support planetarium style projections, we had to implement it into the PYTHON package. To achieve this, we had to modify both `Scene` and `Render` object implementations and in particular their interfaced C-native routines. In detail, we mentioned that `Scene` prepares the scenery, using the `Camera` parameters, by isolating particles in the FoV and converting their 3D coordinates and smoothing lengths to projected ones. In this case, we needed to add an option for forking that computation to a different projection scheme: the azimuthal equidistant projection, considering the spherical cap centred on the camera position that the FoV projects onto. For customization, we also implemented a feature that would allow the `Camera` target position to be shifted, so that it translates into a shift in altitude onto the planetarium dome (as the target would be by default at the planetarium north pole). A particularity of this projection is that it distort circles, and as such, smoothing lengths projected on the spherical cap. To take into consideration those distortions, we also added a forking in the `Render` implementation to deal with those distortions based on the projected `Scene` properties. With this updated software we produced 4 square movies in extreme resolution (4096×4096) for dark matter, star, gas and hot gas components, which the Fiske planetarium production team edited to blend them together in a single video[7]. This work also leaded to the production of the movie mentioned in Figure 2.1, made as part of collaboration with the Lynx X-Ray Observatory[8].

A.3 Future implementation ideas

A.3.1 Refining orientation interpolation

Currently, the interpolation scheme between anchor point orientations of the camera is limited by its panning/tilting/rolling description. This is generally convenient, es-

---

[7]final production has been featured on this link `https://twitter.com/nonstopbenopp/status/1111007465770905600`

[8]featured on this link `https://twitter.com/astrogrant/status/1085744244411621378`

pecially for creating a contiguous rotational movement of the camera. However it limits versatility to particular cases such as orientate movies along edge-on or face-on views. On that note, because structure morphologies and, by extension, 3-axes basis descriptions (via the inertia tensor as in Section 3.3), evolve in time, and since the panning/tilting/rolling camera orientation description translates to a 3-axes basis, we need a scheme that can interpolate between bases. The Spherical Linear intERPolation (SLerp) appears to be such a scheme. Generally used in computer graphics, it enables the animation of 3D rotation via quaternion interpolations [9]. Exploring this technique would potentially enable us to adapt movies to the morphology of the evolving objects that are meant to be rendered.

A.3.2 Higher framerate resolution

Another limitation of our current software relates to the way the evolution framerate matches the timestep rate of the simulation. In other words, each successive frame cannot represent timesteps that are between 2 successive snapshot/snipshot. If the evolution that we want to observe is too fast despite each frame representing all snapshots/snipshots, the only option available is too slower down the movie artificially by interpolating between the final images. This has very limited efficacy and generally does not render a satisfying result. Such limitation could be overcome if instead of interpolating between final images, the software could interpolate the particle properties between snapshots/snipshots directly. While it would be straightforward for dark matter particles, baryonic particles, especially gas and star, are more elaborate. GADGET3 simulations convert on the fly gas particles into star ones, so interpolation schemes would require particular care for these. Nonetheless, such addition would improve greatly the software capability.

---

[9]the quaternion space is an extended 4D number system where the multiplication is down-compatible with the 2D number system of the complex numbers; an interesting feature in our case is that unit quaternion number translates to a rotation transformation of the 3D space.

A.3.3 Additional projection schemes

The implementation of the planetarium projection feature opened the way for the addition of other projection schemes to the PYTHON package PY-SPHVIEWER. Currently, three projections are available, namely the perspective projection (by default), the axonometric projection (virtually similar to the perspective one, but placing the camera at infinity) and the azimuthal equidistant projection. As virtual reality (commonly referred as VR) medias are becoming more and more popular, the equirectangular projection scheme would be an excellent addition to the package. By default this scheme projects an entire sphere onto a rectangle. Therefore, if considering the sphere centred on the camera projection as a projecting surface of the entire space, we can project via this scheme the entire space onto a 2D screen. This is done by considering a single camera, but 3-dimensional perception requires a pair of two cameras. While the calculation for a single camera is straightforward, particular care would need to be considered for implementing this pair of two cameras.

Bibliography

M. G. Abadi, J. F. Navarro, M. Steinmetz, and V. R. Eke. Simulations of Galaxy Formation in a Λ Cold Dark Matter Universe. II. The Fine Structure of Simulated Galactic Disks. *ApJ*, 597:21–34, November 2003. doi: 10.1086/378316.

R. G. Abraham, S. van den Bergh, and P. Nair. A New Approach to Galaxy Morphology. I. Analysis of the Sloan Digital Sky Survey Early Data Release. *ApJ*, 588: 218–229, May 2003. doi: 10.1086/373919.

O. Agertz, B. Moore, J. Stadel, D. Potter, F. Miniati, J. Read, L. Mayer, A. Gawryszczak, A. Kravtsov, Å. Nordlund, F. Pearce, V. Quilis, D. Rudd, V. Springel, J. Stone, E. Tasker, R. Teyssier, J. Wadsley, and R. Walder. Fundamental differences between SPH and grid methods. *MNRAS*, 380:963–978, September 2007. doi: 10.1111/j.1365-2966.2007.12183.x.

O. Agertz, R. Teyssier, and B. Moore. The formation of disc galaxies in a ΛCDM universe. *MNRAS*, 410:1391–1408, January 2011. doi: 10.1111/j.1365-2966.2010. 17530.x.

A. Albrecht and P. J. Steinhardt. Cosmology for grand unified theories with radiatively induced symmetry breaking. *Physical Review Letters*, 48:1220–1223, April 1982. doi: 10.1103/PhysRevLett.48.1220.

D. G. Algorry, J. F. Navarro, M. G. Abadi, L. V. Sales, R. G. Bower, R. A. Crain, C. Dalla Vecchia, C. S. Frenk, M. Schaller, J. Schaye, and T. Theuns. Barred galaxies in the EAGLE cosmological hydrodynamical simulation. *MNRAS*, 469:1054–1064, July 2017. doi: 10.1093/mnras/stx1008.

B. Allgood, R. A. Flores, J. R. Primack, A. V. Kravtsov, R. H. Wechsler, A. Faltenbacher, and J. S. Bullock. The shape of dark matter haloes: dependence on mass, redshift, radius and formation. *MNRAS*, 367:1781–1796, April 2006. doi: 10.1111/j.1365-2966.2006.10094.x.

R. A. Alpher, H. Bethe, and G. Gamow. The Origin of Chemical Elements. *Physical Review*, 73:803–804, April 1948. doi: 10.1103/PhysRev.73.803.

J. A. Arnold, A. J. Romanowsky, J. P. Brodie, L. Chomiuk, L. R. Spitler, J. Strader, A. J. Benson, and D. A. Forbes. The Fossil Record of Two-phase Galaxy Assembly: Kinematics and Metallicities in the Nearest S0 Galaxy. *ApJl*, 736:L26, August 2011. doi: 10.1088/2041-8205/736/2/L26.

K. M. Ashman and S. E. Zepf. The formation of globular clusters in merging and interacting galaxies. *ApJ*, 384:50–61, January 1992. doi: 10.1086/170850.

Y. M. Bahé, D. J. Barnes, C. Dalla Vecchia, S. T. Kay, S. D. M. White, I. G. McCarthy, J. Schaye, R. G. Bower, R. A. Crain, T. Theuns, A. Jenkins, S. L. McGee, M. Schaller, P. A. Thomas, and J. W. Trayford. The Hydrangea simulations: galaxy formation in and around massive clusters. *MNRAS*, 470:4186–4208, October 2017. doi: 10.1093/mnras/stx1403.

I. K. Baldry, K. Glazebrook, J. Brinkmann, Ž. Ivezić, R. H. Lupton, R. C. Nichol, and A. S. Szalay. Quantifying the Bimodal Color-Magnitude Distribution of Galaxies. *ApJ*, 600:681–694, January 2004. doi: 10.1086/380092.

I. K. Baldry, M. L. Balogh, R. G. Bower, K. Glazebrook, R. C. Nichol, S. P. Bamford, and T. Budavari. Galaxy bimodality versus stellar mass and environment. *MNRAS*, 373:469–483, December 2006. doi: 10.1111/j.1365-2966.2006.11081.x.

I. K. Baldry, K. Glazebrook, and S. P. Driver. On the galaxy stellar mass function, the mass-metallicity relation and the implied baryonic mass function. *MNRAS*, 388: 945–959, August 2008. doi: 10.1111/j.1365-2966.2008.13348.x.

I. K. Baldry, S. P. Driver, J. Loveday, E. N. Taylor, L. S. Kelvin, J. Liske, P. Norberg, A. S. G. Robotham, S. Brough, A. M. Hopkins, S. P. Bamford, J. A. Peacock,

J. Bland-Hawthorn, C. J. Conselice, S. M. Croom, D. H. Jones, H. R. Parkinson, C. C. Popescu, M. Prescott, R. G. Sharp, and R. J. Tuffs. Galaxy And Mass Assembly (GAMA): the galaxy stellar mass function at z < 0.06. *MNRAS*, 421:621–634, March 2012. doi: 10.1111/j.1365-2966.2012.20340.x.

D. J. Barnes, S. T. Kay, Y. M. Bahé, C. Dalla Vecchia, I. G. McCarthy, J. Schaye, R. G. Bower, A. Jenkins, P. A. Thomas, M. Schaller, R. A. Crain, T. Theuns, and S. D. M. White. The Cluster-EAGLE project: global properties of simulated clusters with resolved galaxies. *MNRAS*, 471:1088–1106, October 2017. doi: 10.1093/mnras/ stx1647.

L. P. Bassino, T. Richtler, and B. Dirsch. Globular cluster systems in low-luminosity early-type galaxies near the Fornax cluster centre. *MNRAS*, 367:156–168, March 2006. doi: 10.1111/j.1365-2966.2005.09919.x.

A. Bauer and V. Springel. Subsonic turbulence in smoothed particle hydrodynamics and moving-mesh simulations. *MNRAS*, 423:2558–2578, July 2012. doi: 10.1111/ j.1365-2966.2012.21058.x.

M. A. Beasley, R. M. Sharples, T. J. Bridges, D. A. Hanes, S. E. Zepf, K. M. Ashman, and D. Geisler. Ages and metallicities of globular clusters in NGC 4472. *MNRAS*, 318:1249–1263, November 2000. doi: 10.1046/j.1365-8711.2000.03885.x.

M. A. Beasley, C. M. Baugh, D. A. Forbes, R. M. Sharples, and C. S. Frenk. On the formation of globular cluster systems in a hierarchical Universe. *MNRAS*, 333: 383–399, June 2002. doi: 10.1046/j.1365-8711.2002.05402.x.

M. A. Beasley, D. A. Forbes, J. P. Brodie, and M. Kissler-Patig. Keck spectroscopy and imaging of globular clusters in the lenticular galaxy NGC 524. *MNRAS*, 347: 1150–1163, February 2004. doi: 10.1111/j.1365-2966.2004.07289.x.

P. Behroozi, R. Wechsler, A. Hearin, and C. Conroy. UniverseMachine: The Correlation between Galaxy Growth and Dark Matter Halo Assembly from z=0-10. *arXiv e-prints*, June 2018.

E. F. Bell, D. H. McIntosh, N. Katz, and M. D. Weinberg. The Optical and Near-Infrared Properties of Galaxies. I. Luminosity and Stellar Mass Functions. *ApJS*, 149:289–312, December 2003. doi: 10.1086/378847.

R. Bender, R. P. Saglia, and O. E. Gerhard. Line-of-Sight Velocity Distributions of Elliptical Galaxies. *MNRAS*, 269:785, August 1994. doi: 10.1093/mnras/269.3.785.

A. Benítez-Llambay. py-sphviewer: Py-sphviewer v1.0.0, July 2015. URL `http://dx.doi.org/10.5281/zenodo.21703`.

A. Benítez-Llambay, J. F. Navarro, C. S. Frenk, and A. D. Ludlow. The vertical structure of gaseous galaxy discs in cold dark matter haloes. *MNRAS*, 473:1019–1037, January 2018. doi: 10.1093/mnras/stx2420.

P. Bett. Halo shapes from weak lensing: the impact of galaxy-halo misalignment. *MNRAS*, 420:3303–3323, March 2012. doi: 10.1111/j.1365-2966.2011.20258.x.

P. Bett, V. Eke, C. S. Frenk, A. Jenkins, J. Helly, and J. Navarro. The spin and shape of dark matter haloes in the Millennium simulation of a Λ cold dark matter universe. *MNRAS*, 376:215–232, March 2007. doi: 10.1111/j.1365-2966.2007.11432.x.

J. Binney. Is the flattening of elliptical galaxies necessarily due to rotation. *MNRAS*, 177:19–29, October 1976. doi: 10.1093/mnras/177.1.19.

J. Binney. On the rotation of elliptical galaxies. *MNRAS*, 183:501–514, May 1978. doi: 10.1093/mnras/183.3.501.

J. Binney and S. Tremaine. *Galactic dynamics*. 1987.

J. P. Blakeslee, M. Cantiello, and E. W. Peng. The Mass-Metallicity Relation of Globular Clusters in the Context of Nonlinear Color-Metallicty Relations. *ApJ*, 710: 51–63, February 2010. doi: 10.1088/0004-637X/710/1/51.

M. R. Blanton, D. W. Hogg, N. A. Bahcall, I. K. Baldry, J. Brinkmann, I. Csabai, D. Eisenstein, M. Fukugita, J. E. Gunn, Ž. Ivezić, D. Q. Lamb, R. H. Lupton, J. Loveday, J. A. Munn, R. C. Nichol, S. Okamura, D. J. Schlegel, K. Shimasaku,

M. A. Strauss, M. S. Vogeley, and D. H. Weinberg. The Broadband Optical Properties of Galaxies with Redshifts 0.02<z<0.22. *ApJ*, 594:186–207, September 2003. doi: 10.1086/375528.

G. R. Blumenthal, H. Pagels, and J. R. Primack. Galaxy formation by dissipationless particles heavier than neutrinos. *Nature*, 299:37, September 1982. doi: 10.1038/299037a0.

G. R. Blumenthal, S. M. Faber, J. R. Primack, and M. J. Rees. Formation of galaxies and large-scale structure with cold dark matter. *Nature*, 311:517–525, October 1984. doi: 10.1038/311517a0.

J. R. Bond and A. S. Szalay. The collisionless damping of density fluctuations in an expanding universe. *ApJ*, 274:443–468, November 1983. doi: 10.1086/161460.

J. R. Bond, G. Efstathiou, and J. Silk. Massive neutrinos and the large-scale structure of the universe. *Physical Review Letters*, 45:1980–1984, December 1980. doi: 10.1103/PhysRevLett.45.1980.

J. R. Bond, A. S. Szalay, and M. S. Turner. Formation of galaxies in a gravitino-dominated universe. *Physical Review Letters*, 48:1636–1639, June 1982. doi: 10.1103/PhysRevLett.48.1636.

C. M. Booth and J. Schaye. Cosmological simulations of the growth of supermassive black holes and feedback from active galactic nuclei: method and tests. *MNRAS*, 398:53–74, September 2009. doi: 10.1111/j.1365-2966.2009.15043.x.

R. G. Bower, A. J. Benson, R. Malbon, J. C. Helly, C. S. Frenk, C. M. Baugh, S. Cole, and C. G. Lacey. Breaking the hierarchy of galaxy formation. *MNRAS*, 370:645–655, August 2006. doi: 10.1111/j.1365-2966.2006.10519.x.

S. Bridle and L. King. Dark energy constraints from cosmic shear power spectra: impact of intrinsic alignments on photometric redshift requirements. *New Journal of Physics*, 9:444, December 2007. doi: 10.1088/1367-2630/9/12/444.

J. P. Brodie and S. S. Larsen. New Members of the Cluster Family in Nearby Lenticular Galaxies. *AJ*, 124:1410–1417, September 2002. doi: 10.1086/341824.

J. P. Brodie and J. Strader. Extragalactic Globular Clusters and Galaxy Formation. *ARA&A*, 44:193–267, September 2006. doi: 10.1146/annurev.astro.44.051905. 092441.

J. P. Brodie, C. Usher, C. Conroy, J. Strader, J. A. Arnold, D. A. Forbes, and A. J. Romanowsky. The SLUGGS Survey: NGC 3115, A Critical Test Case for Metallicity Bimodality in Globular Cluster Systems. *ApJl*, 759:L33, November 2012. doi: 10.1088/2041-8205/759/2/L33.

J. P. Brodie, A. J. Romanowsky, J. Strader, D. A. Forbes, C. Foster, Z. G. Jennings, N. Pastorello, V. Pota, C. Usher, C. Blom, J. Kader, J. C. Roediger, L. R. Spitler, A. Villaume, J. A. Arnold, S. S. Kartha, and K. A. Woodley. The SAGES Legacy Unifying Globulars and GalaxieS Survey (SLUGGS): Sample Definition, Methods, and Initial Results. *ApJ*, 796:52, November 2014. doi: 10.1088/0004-637X/796/1/ 52.

C. B. Brook, F. Governato, R. Roškar, G. Stinson, A. M. Brooks, J. Wadsley, T. Quinn, B. K. Gibson, O. Snaith, K. Pilkington, E. House, and A. Pontzen. Hierarchical formation of bulgeless galaxies: why outflows have low angular momentum. *MNRAS*, 415:1051–1060, August 2011. doi: 10.1111/j.1365-2966.2011.18545.x.

S. E. Bryan, S. Mao, S. T. Kay, J. Schaye, C. Dalla Vecchia, and C. M. Booth. Influence of baryons on the orbital structure of dark matter haloes. *MNRAS*, 422:1863–1879, May 2012. doi: 10.1111/j.1365-2966.2011.20298.x.

S. E. Bryan, S. T. Kay, A. R. Duffy, J. Schaye, C. Dalla Vecchia, and C. M. Booth. The impact of baryons on the spins and shapes of dark matter haloes. *MNRAS*, 429: 3316–3329, March 2013. doi: 10.1093/mnras/sts587.

J. S. Bullock, A. V. Kravtsov, and D. H. Weinberg. Reionization and the Abundance of Galactic Satellites. *ApJ*, 539:517–521, August 2000. doi: 10.1086/309279.

J. S. Bullock, A. Dekel, T. S. Kolatt, A. V. Kravtsov, A. A. Klypin, C. Porciani, and J. R. Primack. A Universal Angular Momentum Profile for Galactic Halos. *ApJ*, 555:240–257, July 2001. doi: 10.1086/321477.

K. Bundy, M. A. Bershady, D. R. Law, R. Yan, N. Drory, N. MacDonald, D. A. Wake, B. Cherinka, J. R. Sánchez-Gallego, A.-M. Weijmans, D. Thomas, C. Tremonti, K. Masters, L. Coccato, A. M. Diamond-Stanic, A. Aragón-Salamanca, V. Avila-Reese, C. Badenes, J. Falcón-Barroso, F. Belfiore, D. Bizyaev, G. A. Blanc, J. Bland-Hawthorn, M. R. Blanton, J. R. Brownstein, N. Byler, M. Cappellari, C. Conroy, A. A. Dutton, E. Emsellem, J. Etherington, P. M. Frinchaboy, H. Fu, J. E. Gunn, P. Harding, E. J. Johnston, G. Kauffmann, K. Kinemuchi, M. A. Klaene, J. H. Knapen, A. Leauthaud, C. Li, L. Lin, R. Maiolino, V. Malanushenko, E. Malanushenko, S. Mao, C. Maraston, R. M. McDermid, M. R. Merrifield, R. C. Nichol, D. Oravetz, K. Pan, J. K. Parejko, S. F. Sanchez, D. Schlegel, A. Simmons, O. Steele, M. Steinmetz, K. Thanjavur, B. A. Thompson, J. L. Tinker, R. C. E. van den Bosch, K. B. Westfall, D. Wilkinson, S. Wright, T. Xiao, and K. Zhang. Overview of the SDSS-IV MaNGA Survey: Mapping nearby Galaxies at Apache Point Observatory. *ApJ*, 798:7, January 2015. doi: 10.1088/0004-637X/798/1/7.

S. Butterworth. On the Theory of Filter Amplifiers. *Wireless Engineer*, 7, 1930.

M. Cappellari. Structure and Kinematics of Early-Type Galaxies from Integral Field Spectroscopy. *ARA&A*, 54:597–665, September 2016. doi: 10.1146/annurev-astro-082214-122432.

M. Cappellari, E. Emsellem, D. Krajnović, R. M. McDermid, N. Scott, G. A. Verdoes Kleijn, L. M. Young, K. Alatalo, R. Bacon, L. Blitz, M. Bois, F. Bournaud, M. Bureau, R. L. Davies, T. A. Davis, P. T. de Zeeuw, P.-A. Duc, S. Khochfar, H. Kuntschner, P.-Y. Lablanche, R. Morganti, T. Naab, T. Oosterloo, M. Sarzi, P. Serra, and A.-M. Weijmans. The ATLAS^{3D} project - I. A volume-limited sample of 260 nearby early-type galaxies: science goals and selection criteria. *MNRAS*, 413:813–836, May 2011. doi: 10.1111/j.1365-2966.2010.18174.x.

G. Chabrier. Galactic Stellar and Substellar Initial Mass Function. *PASP*, 115:763–795, July 2003. doi: 10.1086/376392.

B. Clauwens, J. Schaye, M. Franx, and R. G. Bower. The three phases of galaxy formation. *MNRAS*, 478:3994–4009, August 2018. doi: 10.1093/mnras/sty1229.

W. S. Cleveland. Robust Locally Weighted Regression and Smoothing Scatterplots. *Journal of the American Statistical Association*, 74(368):829–836, 1979. doi: 10.1080/01621459.1979.10481038. URL https://www.tandfonline.com/doi/abs/10.1080/01621459.1979.10481038.

W. S. Cleveland. LOWESS: A Program for Smoothing Scatterplots by Robust Locally Weighted Regression. *The American Statistician*, 35(1):54–54, 1981. ISSN 00031305. doi: 10.2307/2683591. URL http://www.jstor.org/stable/2683591.

W. S. Cleveland and S. J. Devlin. Locally Weighted Regression: An Approach to Regression Analysis by Local Fitting. *Journal of the American Statistical Association*, 83(403):596–610, 1988. doi: 10.1080/01621459.1988.10478639. URL https://www.tandfonline.com/doi/abs/10.1080/01621459.1988.10478639.

D. Clowe, M. Bradač, A. H. Gonzalez, M. Markevitch, S. W. Randall, C. Jones, and D. Zaritsky. A Direct Empirical Proof of the Existence of Dark Matter. *ApJl*, 648:L109–L113, September 2006. doi: 10.1086/508162.

L. Coccato, O. Gerhard, M. Arnaboldi, P. Das, N. G. Douglas, K. Kuijken, M. R. Merrifield, N. R. Napolitano, E. Noordermeer, A. J. Romanowsky, M. Capaccioli, A. Cortesi, F. De Lorenzi, and K. C. Freeman. Kinematic properties of early-type galaxy haloes using planetary nebulae*. *MNRAS*, 394:1249–1283, April 2009. doi: 10.1111/j.1365-2966.2009.14417.x.

J. G. Cohen, J. P. Blakeslee, and A. Ryzhov. The Ages and Abundances of a Large Sample of M87 Globular Clusters. *ApJ*, 496:808–826, March 1998. doi: 10.1086/305429.

S. Cole and C. Lacey. The structure of dark matter haloes in hierarchical clustering models. *MNRAS*, 281:716, July 1996. doi: 10.1093/mnras/281.2.716.

S. Cole, P. Norberg, C. M. Baugh, C. S. Frenk, J. Bland-Hawthorn, T. Bridges, R. Cannon, M. Colless, C. Collins, W. Couch, N. Cross, G. Dalton, R. De Propris, S. P. Driver, G. Efstathiou, R. S. Ellis, K. Glazebrook, C. Jackson, O. Lahav, I. Lewis, S. Lumsden, S. Maddox, D. Madgwick, J. A. Peacock, B. A. Peterson, W. Sutherland, and K. Taylor. The 2dF galaxy redshift survey: near-infrared galaxy luminosity functions. *MNRAS*, 326:255–273, September 2001. doi: 10.1046/j.1365-8711.2001.04591.x.

C. A. Correa, J. Schaye, B. Clauwens, R. G. Bower, R. A. Crain, M. Schaller, T. Theuns, and A. C. R. Thob. The relation between galaxy morphology and colour in the EAGLE simulation. *MNRAS*, 472:L45–L49, November 2017. doi: 10.1093/mnrasl/slx133.

L. Cortese, L. M. R. Fogarty, K. Bekki, J. van de Sande, W. Couch, B. Catinella, M. Colless, D. Obreschkow, D. Taranu, E. Tescari, D. Barat, J. Bland-Hawthorn, J. Bloom, J. J. Bryant, M. Cluver, S. M. Croom, M. J. Drinkwater, F. d'Eugenio, I. S. Konstantopoulos, A. Lopez-Sanchez, S. Mahajan, N. Scott, C. Tonini, O. I. Wong, J. T. Allen, S. Brough, M. Goodwin, A. W. Green, I.-T. Ho, L. S. Kelvin, J. S. Lawrence, N. P. F. Lorente, A. M. Medling, M. S. Owers, S. Richards, R. Sharp, and S. M. Sweet. The SAMI Galaxy Survey: the link between angular momentum and optical morphology. *MNRAS*, 463:170–184, November 2016. doi: 10.1093/mnras/stw1891.

P. Côté, R. O. Marzke, and M. J. West. The Formation of Giant Elliptical Galaxies and Their Globular Cluster Systems. *ApJ*, 501:554–570, July 1998. doi: 10.1086/305838.

R. A. Crain, T. Theuns, C. Dalla Vecchia, V. R. Eke, C. S. Frenk, A. Jenkins, S. T. Kay, J. A. Peacock, F. R. Pearce, J. Schaye, V. Springel, P. A. Thomas, S. D. M. White, and R. P. C. Wiersma. Galaxies-intergalactic medium interaction calculation

- I. Galaxy formation as a function of large-scale environment. *MNRAS*, 399:1773–1794, November 2009. doi: 10.1111/j.1365-2966.2009.15402.x.

R. A. Crain, I. G. McCarthy, C. S. Frenk, T. Theuns, and J. Schaye. X-ray coronae in simulations of disc galaxy formation. *MNRAS*, 407:1403–1422, September 2010. doi: 10.1111/j.1365-2966.2010.16985.x.

R. A. Crain, J. Schaye, R. G. Bower, M. Furlong, M. Schaller, T. Theuns, C. Dalla Vecchia, C. S. Frenk, I. G. McCarthy, J. C. Helly, A. Jenkins, Y. M. Rosas-Guevara, S. D. M. White, and J. W. Trayford. The EAGLE simulations of galaxy formation: calibration of subgrid physics and model variations. *MNRAS*, 450:1937–1961, June 2015. doi: 10.1093/mnras/stv725.

S. M. Croom, J. S. Lawrence, J. Bland-Hawthorn, J. J. Bryant, L. Fogarty, S. Richards, M. Goodwin, T. Farrell, S. Miziarski, R. Heald, D. H. Jones, S. Lee, M. Colless, S. Brough, A. M. Hopkins, A. E. Bauer, M. N. Birchall, S. Ellis, A. Horton, S. Leon-Saval, G. Lewis, Á. R. López-Sánchez, S.-S. Min, C. Trinh, and H. Trowland. The Sydney-AAO Multi-object Integral field spectrograph. *MNRAS*, 421:872–893, March 2012. doi: 10.1111/j.1365-2966.2011.20365.x.

D. J. Croton, V. Springel, S. D. M. White, G. De Lucia, C. S. Frenk, L. Gao, A. Jenkins, G. Kauffmann, J. F. Navarro, and N. Yoshida. The many lives of active galactic nuclei: cooling flows, black holes and the luminosities and colours of galaxies. *MNRAS*, 365:11–28, January 2006. doi: 10.1111/j.1365-2966.2005.09675.x.

L. Cullen and W. Dehnen. Inviscid smoothed particle hydrodynamics. *MNRAS*, 408:669–683, October 2010. doi: 10.1111/j.1365-2966.2010.17158.x.

H. D. Curtis. Novae in the Spiral Nebulae and the Island Universe Theory. *PASP*, 29:206–207, October 1917. doi: 10.1086/122632.

C. Dalla Vecchia and J. Schaye. Simulating galactic outflows with thermal supernova feedback. *MNRAS*, 426:140–158, October 2012. doi: 10.1111/j.1365-2966.2012.21704.x.

J. J. Davies, R. A. Crain, I. G. McCarthy, B. D. Oppenheimer, J. Schaye, M. Schaller, and S. McAlpine. The gas fractions of dark matter haloes hosting simulated L galaxies are governed by the feedback history of their black holes. *MNRAS*, March 2019. doi: 10.1093/mnras/stz635.

M. Davis, G. Efstathiou, C. S. Frenk, and S. D. M. White. The evolution of large-scale structure in a universe dominated by cold dark matter. *ApJ*, 292:371–394, May 1985. doi: 10.1086/163168.

M. E. De Rossi, R. G. Bower, A. S. Font, J. Schaye, and T. Theuns. Galaxy metallicity scaling relations in the EAGLE simulations. *MNRAS*, 472:3354–3377, December 2017. doi: 10.1093/mnras/stx2158.

W. de Sitter. On the relativity of inertia. Remarks concerning Einstein's latest hypothesis. *Koninklijke Nederlandse Akademie van Wetenschappen Proceedings Series B Physical Sciences*, 19:1217–1225, March 1917a.

W. de Sitter. Einstein's theory of gravitation and its astronomical consequences. Third paper. *MNRAS*, 78:3–28, November 1917b. doi: 10.1093/mnras/78.1.3.

G. de Vaucouleurs. Classification and Morphology of External Galaxies. *Handbuch der Physik*, 53:275, 1959.

P. T. de Zeeuw, M. Bureau, E. Emsellem, R. Bacon, C. M. Carollo, Y. Copin, R. L. Davies, H. Kuntschner, B. W. Miller, G. Monnet, R. F. Peletier, and E. K. Verolme. The SAURON project - II. Sample and early results. *MNRAS*, 329:513–530, January 2002. doi: 10.1046/j.1365-8711.2002.05059.x.

A. J. Deason, I. G. McCarthy, A. S. Font, N. W. Evans, C. S. Frenk, V. Belokurov, N. I. Libeskind, R. A. Crain, and T. Theuns. Mismatch and misalignment: dark haloes and satellites of disc galaxies. *MNRAS*, 415:2607–2625, August 2011. doi: 10.1111/j.1365-2966.2011.18884.x.

A. Dekel and J. Silk. The origin of dwarf galaxies, cold dark matter, and biased galaxy formation. *ApJ*, 303:39–55, April 1986. doi: 10.1086/164050.

T. Di Matteo, V. Springel, and L. Hernquist. Energy input from quasars regulates the growth and activity of black holes and their host galaxies. *Nature*, 433:604–607, February 2005. doi: 10.1038/nature03335.

G. A. Dilts. Moving-least-squares-particle hydrodynamics - I. Consistency and stability. *International Journal for Numerical Methods in Engineering*, 44: 1115–1155, March 1999. doi: 10.1002/(SICI)1097-0207(19990320)44:8<1115:: AID-NME547>3.0.CO;2-L.

K. Dolag, S. Borgani, G. Murante, and V. Springel. Substructures in hydrodynamical cluster simulations. *MNRAS*, 399:497–514, October 2009. doi: 10.1111/j. 1365-2966.2009.15034.x.

K. Dolag, B. M. Gaensler, A. M. Beck, and M. C. Beck. Constraints on the distribution and energetics of fast radio bursts using cosmological hydrodynamic simulations. *MNRAS*, 451:4277–4289, August 2015. doi: 10.1093/mnras/stv1190.

A. G. Doroshkevich, Y. B. Zel'dovich, and R. A. Syunyaev. Fluctuations of the microwave background radiation in the adiabatic and entropic theories of galaxy formation. *Soviet Ast.*, 22:523–528, October 1978.

A. G. Doroshkevich, M. I. Khlopov, R. A. Sunyaev, A. S. Szalay, and I. B. Zeldovich. Cosmological impact of the neutrino rest mass. *Annals of the New York Academy of Sciences*, 375:32–42, December 1981. doi: 10.1111/j.1749-6632.1981.tb33688.x.

A. Dressler. Galaxy morphology in rich clusters - Implications for the formation and evolution of galaxies. *ApJ*, 236:351–365, March 1980. doi: 10.1086/157753.

S. P. Driver, P. D. Allen, A. W. Graham, E. Cameron, J. Liske, S. C. Ellis, N. J. G. Cross, R. De Propris, S. Phillipps, and W. J. Couch. The Millennium Galaxy Catalogue: morphological classification and bimodality in the colour-concentration plane. *MNRAS*, 368:414–434, May 2006. doi: 10.1111/j.1365-2966.2006.10126.x.

J. Dubinski. The effect of dissipation on the shapes of dark halos. *ApJ*, 431:617–624, August 1994. doi: 10.1086/174512.

J. Dubinski and R. G. Carlberg. The structure of cold dark matter halos. *ApJ*, 378: 496–503, September 1991. doi: 10.1086/170451.

Y. Dubois, C. Pichon, C. Welker, D. Le Borgne, J. Devriendt, C. Laigle, S. Codis, D. Pogosyan, S. Arnouts, K. Benabed, E. Bertin, J. Blaizot, F. Bouchet, J.-F. Cardoso, S. Colombi, V. de Lapparent, V. Desjacques, R. Gavazzi, S. Kassin, T. Kimm, H. McCracken, B. Milliard, S. Peirani, S. Prunet, S. Rouberol, J. Silk, A. Slyz, T. Sousbie, R. Teyssier, L. Tresse, M. Treyer, D. Vibert, and M. Volonteri. Dancing in the dark: galactic properties trace spin swings along the cosmic web. *MNRAS*, 444:1453–1468, October 2014. doi: 10.1093/mnras/stu1227.

F. Durier and C. Dalla Vecchia. Implementation of feedback in smoothed particle hydrodynamics: towards concordance of methods. *MNRAS*, 419:465–478, January 2012. doi: 10.1111/j.1365-2966.2011.19712.x.

G. Efstathiou, W. J. Sutherland, and S. J. Maddox. The cosmological constant and cold dark matter. *Nature*, 348:705–707, December 1990. doi: 10.1038/348705a0.

G. Efstathiou, J. R. Bond, and S. D. M. White. COBE background radiation anisotropies and large-scale structure in the universe. *MNRAS*, 258:1P–6P, September 1992. doi: 10.1093/mnras/258.1.1P.

J. Einasto, A. Kaasik, and E. Saar. Dynamic evidence on massive coronas of galaxies. *Nature*, 250:309–310, July 1974. doi: 10.1038/250309a0.

A. Einstein. Die Grundlage der allgemeinen Relativitätstheorie. *Annalen der Physik*, 354:769–822, 1916. doi: 10.1002/andp.19163540702.

A. Einstein. Kosmologische Betrachtungen zur allgemeinen Relativitätstheorie. *Sitzungsberichte der Königlich Preußischen Akademie der Wissenschaften (Berlin), Seite 142-152.*, 1917.

E. Emsellem, M. Cappellari, D. Krajnović, G. van de Ven, R. Bacon, M. Bureau, R. L. Davies, P. T. de Zeeuw, J. Falcón-Barroso, H. Kuntschner, R. McDermid, R. F. Peletier, and M. Sarzi. The SAURON project - IX. A kinematic

classification for early-type galaxies. *MNRAS*, 379:401–417, August 2007. doi: 10.1111/j.1365-2966.2007.11752.x.

E. Emsellem, M. Cappellari, D. Krajnović, K. Alatalo, L. Blitz, M. Bois, F. Bournaud, M. Bureau, R. L. Davies, T. A. Davis, P. T. de Zeeuw, S. Khochfar, H. Kuntschner, P.-Y. Lablanche, R. M. McDermid, R. Morganti, T. Naab, T. Oosterloo, M. Sarzi, N. Scott, P. Serra, G. van de Ven, A.-M. Weijmans, and L. M. Young. The ATLAS^{3D} project - III. A census of the stellar angular momentum within the effective radius of early-type galaxies: unveiling the distribution of fast and slow rotators. *MNRAS*, 414:888–912, June 2011. doi: 10.1111/j.1365-2966.2011.18496.x.

A. E. Evrard, F. J. Summers, and M. Davis. Two-fluid simulations of galaxy formation. *ApJ*, 422:11–36, February 1994. doi: 10.1086/173700.

S. M. Faber and J. S. Gallagher. Masses and mass-to-light ratios of galaxies. *ARA&A*, 17:135–187, 1979. doi: 10.1146/annurev.aa.17.090179.001031.

A. C. Fabian. Observational Evidence of Active Galactic Nuclei Feedback. *ARA&A*, 50:455–489, September 2012. doi: 10.1146/annurev-astro-081811-125521.

F. R. Faifer, J. C. Forte, M. A. Norris, T. Bridges, D. A. Forbes, S. E. Zepf, M. Beasley, K. Gebhardt, D. A. Hanes, and R. M. Sharples. Gemini/GMOS imaging of globular cluster systems in five early-type galaxies*. *MNRAS*, 416:155–177, September 2011. doi: 10.1111/j.1365-2966.2011.19018.x.

S. M. Fall and G. Efstathiou. Formation and rotation of disc galaxies with haloes. *MNRAS*, 193:189–206, October 1980. doi: 10.1093/mnras/193.2.189.

S. M. Fall and C. S. Frenk. The true shapes of globular clusters. *AJ*, 88:1626–1632, November 1983. doi: 10.1086/113452.

S. M. Fall and A. J. Romanowsky. Angular Momentum and Galaxy Formation Revisited: Scaling Relations for Disks and Bulges. *ApJ*, 868:133, December 2018. doi: 10.3847/1538-4357/aaeb27.

A. Fattahi, J. F. Navarro, T. Sawala, C. S. Frenk, K. A. Oman, R. A. Crain, M. Furlong, M. Schaller, J. Schaye, T. Theuns, and A. Jenkins. The APOSTLE project: Local Group kinematic mass constraints and simulation candidate selection. *MNRAS*, 457: 844–856, March 2016. doi: 10.1093/mnras/stv2970.

L. M. R. Fogarty, N. Scott, M. S. Owers, S. Brough, S. M. Croom, M. B. Pracy, R. C. W. Houghton, J. Bland-Hawthorn, M. Colless, R. L. Davies, D. H. Jones, J. T. Allen, J. J. Bryant, M. Goodwin, A. W. Green, I. S. Konstantopoulos, J. S. Lawrence, S. Richards, L. Cortese, and R. Sharp. The SAMI Pilot Survey: the kinematic morphology-density relation in Abell 85, Abell 168 and Abell 2399. *MNRAS*, 443: 485–503, September 2014. doi: 10.1093/mnras/stu1165.

D. A. Forbes and T. Bridges. Accreted versus in situ Milky Way globular clusters. *MNRAS*, 404:1203–1214, May 2010. doi: 10.1111/j.1365-2966.2010.16373.x.

D. A. Forbes, M. A. Beasley, J. P. Brodie, and M. Kissler-Patig. Age Estimates for Globular Clusters in NGC 1399. *ApJl*, 563:L143–L146, December 2001. doi: 10. 1086/338593.

D. A. Forbes, T. Ponman, and E. O'Sullivan. The baryonic haloes of elliptical galaxies: radial distribution of globular clusters and diffuse hot gas. *MNRAS*, 425:66–73, September 2012. doi: 10.1111/j.1365-2966.2012.21368.x.

D. A. Forbes, N. Pastorello, A. J. Romanowsky, C. Usher, J. P. Brodie, and J. Strader. The SLUGGS survey: inferring the formation epochs of metal-poor and metal-rich globular clusters. *MNRAS*, 452:1045–1051, September 2015. doi: 10.1093/mnras/ stv1312.

A. D. Forestell and K. Gebhardt. Hobby-Eberly Telescope Observations of the Dark Halo in NGC 821. *ApJ*, 716:370–383, June 2010. doi: 10.1088/0004-637X/716/1/ 370.

C. Foster, L. R. Spitler, A. J. Romanowsky, D. A. Forbes, V. Pota, K. Bekki, J. Strader, R. N. Proctor, J. A. Arnold, and J. P. Brodie. Global properties of 'ordinary' early-type galaxies: photometry and spectroscopy of stars and globular clusters in NGC

4494. *MNRAS*, 415:3393–3416, August 2011. doi: 10.1111/j.1365-2966.2011.
18965.x.

C. Foster, J. van de Sande, F. D'Eugenio, L. Cortese, R. M. McDermid, J. Bland-
Hawthorn, S. Brough, J. Bryant, S. M. Croom, M. Goodwin, I. S. Konstantopoulos,
J. Lawrence, Á. R. López-Sánchez, A. M. Medling, M. S. Owers, S. N. Richards,
N. Scott, D. S. Taranu, C. Tonini, and T. Zafar. The SAMI Galaxy Survey: the
intrinsic shape of kinematically selected galaxies. *MNRAS*, 472:966–978, November
2017. doi: 10.1093/mnras/stx1869.

C. S. Frenk, S. D. M. White, G. Efstathiou, and M. Davis. Galaxy clusters and the
amplitude of primordial fluctuations. *ApJ*, 351:10–21, March 1990. doi: 10.1086/
168439.

J. W. Fried and G. D. Illingworth. Kinematics of 12 elliptical galaxies. *AJ*, 107:992–
1002, March 1994. doi: 10.1086/116912.

A. Friedmann. Über die Krümmung des Raumes. *Zeitschrift fur Physik*, 10:377–386,
1922. doi: 10.1007/BF01332580.

M. Furlong, R. G. Bower, T. Theuns, J. Schaye, R. A. Crain, M. Schaller, C. Dalla Vec-
chia, C. S. Frenk, I. G. McCarthy, J. Helly, A. Jenkins, and Y. M. Rosas-Guevara.
Evolution of galaxy stellar masses and star formation rates in the EAGLE simula-
tions. *MNRAS*, 450:4486–4504, July 2015. doi: 10.1093/mnras/stv852.

M. Furlong, R. G. Bower, R. A. Crain, J. Schaye, T. Theuns, J. W. Trayford, Y. Qu,
M. Schaller, M. Berthet, and J. C. Helly. Size evolution of normal and compact
galaxies in the EAGLE simulation. *MNRAS*, 465:722–738, February 2017. doi:
10.1093/mnras/stw2740.

K. Gebhardt and M. Kissler-Patig. Globular Cluster Systems. I. V-I Color Distribu-
tions. *AJ*, 118:1526–1541, October 1999. doi: 10.1086/301059.

D. Geisler, M. G. Lee, and E. Kim. Washington Photometry of the Globular Cluster
System of NGC 4472.I.Analysis of the Metallicities. *AJ*, 111:1529, April 1996. doi:
10.1086/117894.

C. Gini. *Variabilità e mutabilità*. 1912.

P. Goudfrooij, F. Schweizer, D. Gilmore, and B. C. Whitmore. Dynamical Evolution of Globular Cluster Systems Formed in Galaxy Mergers: Deep Hubble Space Telescope Advanced Camera for Surveys Imaging of Old and Intermediate-Age Globular Clusters in NGC 3610. *AJ*, 133:2737–2751, June 2007. doi: 10.1086/516634.

F. Governato, C. B. Brook, A. M. Brooks, L. Mayer, B. Willman, P. Jonsson, A. M. Stilp, L. Pope, C. Christensen, J. Wadsley, and T. Quinn. Forming a large disc galaxy from a z < 1 major merger. *MNRAS*, 398:312–320, September 2009. doi: 10.1111/j.1365-2966.2009.15143.x.

A. W. Graham and S. P. Driver. A Concise Reference to (Projected) Sérsic $R^{1/n}$ Quantities, Including Concentration, Profile Slopes, Petrosian Indices, and Kron Magnitudes. *PASA*, 22:118–127, 2005. doi: 10.1071/AS05001.

M. T. Graham, M. Cappellari, H. Li, S. Mao, M. A. Bershady, D. Bizyaev, J. Brinkmann, J. R. Brownstein, K. Bundy, N. Drory, D. R. Law, K. Pan, D. Thomas, D. A. Wake, A.-M. Weijmans, K. B. Westfall, and R. Yan. SDSS-IV MaNGA: stellar angular momentum of about 2300 galaxies: unveiling the bimodality of massive galaxy properties. *MNRAS*, 477:4711–4737, July 2018. doi: 10.1093/mnras/sty504.

A. H. Guth. Inflationary universe: A possible solution to the horizon and flatness problems. *Phys. Rev. D*, 23:347–356, January 1981. doi: 10.1103/PhysRevD.23.347.

F. Haardt and P. Madau. Modelling the UV/X-ray cosmic background with CUBA. In D. M. Neumann and J. T. V. Tran, editors, *Clusters of Galaxies and the High Redshift Universe Observed in X-rays*, page 64, 2001.

B. M. S. Hansen, J. S. Kalirai, J. Anderson, A. Dotter, H. B. Richer, R. M. Rich, M. M. Shara, G. G. Fahlman, J. R. Hurley, I. R. King, D. Reitzel, and P. B. Stetson. An age difference of two billion years between a metal-rich and a metal-poor globular cluster. *Nature*, 500:51–53, August 2013. doi: 10.1038/nature12334.

C. M. Hirata and U. Seljak. Intrinsic alignment-lensing interference as a contaminant of cosmic shear. *Phys. Rev. D*, 70(6):063526, September 2004. doi: 10.1103/PhysRevD.70.063526.

P. F. Hopkins. A general class of Lagrangian smoothed particle hydrodynamics methods and implications for fluid mixing problems. *MNRAS*, 428:2840–2856, February 2013. doi: 10.1093/mnras/sts210.

P. F. Hopkins, D. Kereš, J. Oñorbe, C.-A. Faucher-Giguère, E. Quataert, N. Murray, and J. S. Bullock. Galaxies on FIRE (Feedback In Realistic Environments): stellar feedback explains cosmologically inefficient star formation. *MNRAS*, 445:581–603, November 2014. doi: 10.1093/mnras/stu1738.

P. F. Hopkins, A. Wetzel, D. Kereš, C.-A. Faucher-Giguère, E. Quataert, M. Boylan-Kolchin, N. Murray, C. C. Hayward, S. Garrison-Kimmel, C. Hummels, R. Feldmann, P. Torrey, X. Ma, D. Anglés-Alcázar, K.-Y. Su, M. Orr, D. Schmitz, I. Escala, R. Sanderson, M. Y. Grudić, Z. Hafen, J.-H. Kim, A. Fitts, J. S. Bullock, C. Wheeler, T. K. Chan, O. D. Elbert, and D. Narayanan. FIRE-2 simulations: physics versus numerics in galaxy formation. *MNRAS*, 480:800–863, October 2018. doi: 10.1093/mnras/sty1690.

E. Hubble. A Relation between Distance and Radial Velocity among Extra-Galactic Nebulae. *Proceedings of the National Academy of Science*, 15:168–173, March 1929a. doi: 10.1073/pnas.15.3.168.

E. P. Hubble. NGC 6822, a remote stellar system. *ApJ*, 62, December 1925. doi: 10.1086/142943.

E. P. Hubble. A spiral nebula as a stellar system: Messier 33. *ApJ*, 63, May 1926a. doi: 10.1086/142976.

E. P. Hubble. Extragalactic nebulae. *ApJ*, 64, December 1926b. doi: 10.1086/143018.

E. P. Hubble. A spiral nebula as a stellar system, Messier 31. *ApJ*, 69, March 1929b. doi: 10.1086/143167.

O. Ilbert, M. Salvato, E. Le Floc'h, H. Aussel, P. Capak, H. J. McCracken, B. Mobasher, J. Kartaltepe, N. Scoville, D. B. Sanders, S. Arnouts, K. Bundy, P. Cassata, J.-P. Kneib, A. Koekemoer, O. Le Fèvre, S. Lilly, J. Surace, Y. Taniguchi, L. Tasca, D. Thompson, L. Tresse, M. Zamojski, G. Zamorani, and E. Zucca. Galaxy Stellar Mass Assembly Between $0.2 < z < 2$ from the S-COSMOS Survey. *ApJ*, 709: 644–663, February 2010. doi: 10.1088/0004-637X/709/2/644.

A. Jeeson-Daniel, C. Dalla Vecchia, M. R. Haas, and J. Schaye. The correlation structure of dark matter halo properties. *MNRAS*, 415:L69–L73, July 2011. doi: 10.1111/j.1745-3933.2011.01081.x.

A. Jenkins, C. S. Frenk, S. D. M. White, J. M. Colberg, S. Cole, A. E. Evrard, H. M. P. Couchman, and N. Yoshida. The mass function of dark matter haloes. *MNRAS*, 321: 372–384, February 2001.

A. Jordán, P. Côté, J. P. Blakeslee, L. Ferrarese, D. E. McLaughlin, S. Mei, E. W. Peng, J. L. Tonry, D. Merritt, M. Milosavljević, C. L. Sarazin, G. R. Sivakoff, and M. J. West. The ACS Virgo Cluster Survey. X. Half-Light Radii of Globular Clusters in Early-Type Galaxies: Environmental Dependencies and a Standard Ruler for Distance Estimation. *ApJ*, 634:1002–1019, December 2005. doi: 10.1086/497092.

I. Kant. *Allgemeine Naturgeschichte und Theorie des Himmels*. 1755.

J. C. Kapteyn. First Attempt at a Theory of the Arrangement and Motion of the Sidereal System. *ApJ*, 55:302, May 1922. doi: 10.1086/142670.

N. Kardashev. LEMAÎTRE'S Universe and Observations. *ApJl*, 150:L135, December 1967. doi: 10.1086/180110.

N. Katz and J. E. Gunn. Dissipational galaxy formation. I - Effects of gasdynamics. *ApJ*, 377:365–381, August 1991. doi: 10.1086/170367.

N. Katz, D. H. Weinberg, and L. Hernquist. Cosmological Simulations with TreeSPH. *ApJS*, 105:19–+, July 1996. doi: 10.1086/192305.

G. Kauffmann and M. Haehnelt. A unified model for the evolution of galaxies and quasars. *MNRAS*, 311:576–588, January 2000. doi: 10.1046/j.1365-8711.2000.03077.x.

G. Kauffmann, S. D. M. White, and B. Guiderdoni. The Formation and Evolution of Galaxies Within Merging Dark Matter Haloes. *MNRAS*, 264:201–+, September 1993.

S. Kaviraj, C. Laigle, T. Kimm, J. E. G. Devriendt, Y. Dubois, C. Pichon, A. Slyz, E. Chisari, and S. Peirani. The Horizon-AGN simulation: evolution of galaxy properties over cosmic time. *MNRAS*, 467:4739–4752, June 2017. doi: 10.1093/mnras/stx126.

D. Kazanas. Dynamics of the universe and spontaneous symmetry breaking. *ApJl*, 241:L59–L63, October 1980. doi: 10.1086/183361.

S. Kazantzidis, A. V. Kravtsov, A. R. Zentner, B. Allgood, D. Nagai, and B. Moore. The Effect of Gas Cooling on the Shapes of Dark Matter Halos. *ApJl*, 611:L73–L76, August 2004. doi: 10.1086/423992.

L. S. Kelvin, S. P. Driver, A. S. G. Robotham, E. N. Taylor, A. W. Graham, M. Alpaslan, I. Baldry, S. P. Bamford, A. E. Bauer, J. Bland-Hawthorn, M. J. I. Brown, M. Colless, C. J. Conselice, B. W. Holwerda, A. M. Hopkins, M. A. Lara-López, J. Liske, Á. R. López-Sánchez, J. Loveday, P. Norberg, S. Phillipps, C. C. Popescu, M. Prescott, A. E. Sansom, and R. J. Tuffs. Galaxy And Mass Assembly (GAMA): stellar mass functions by Hubble type. *MNRAS*, 444:1647–1659, October 2014. doi: 10.1093/mnras/stu1507.

R. C. Kennicutt, Jr. The rate of star formation in normal disk galaxies. *ApJ*, 272:54–67, September 1983. doi: 10.1086/161261.

N. Khandai, T. Di Matteo, R. Croft, S. Wilkins, Y. Feng, E. Tucker, C. DeGraf, and M.-S. Liu. The MassiveBlack-II simulation: the evolution of haloes and galaxies to $z \sim 0$. *MNRAS*, 450:1349–1374, June 2015. doi: 10.1093/mnras/stv627.

M. Kissler-Patig, J. P. Brodie, L. L. Schroder, D. A. Forbes, C. J. Grillmair, and J. P. Huchra. Keck spectroscopy of globular clusters around NGC 1399. *AJ*, 115:105, January 1998. doi: 10.1086/300186.

S. Kitsionas, C. Federrath, R. S. Klessen, W. Schmidt, D. J. Price, L. J. Dursi, M. Gritschneder, S. Walch, R. Piontek, J. Kim, A.-K. Jappsen, P. Ciecielag, and M.-M. Mac Low. Algorithmic comparisons of decaying, isothermal, supersonic turbulence. *A&A*, 508:541–560, December 2009. doi: 10.1051/0004-6361/200811170.

L. A. Kofman, N. Y. Gnedin, and N. A. Bahcall. Cosmological constant, COBE cosmic microwave background anisotropy, and large-scale clustering. *ApJ*, 413:1–9, August 1993. doi: 10.1086/172970.

D. Krajnović, K. Alatalo, L. Blitz, M. Bois, F. Bournaud, M. Bureau, M. Cappellari, R. L. Davies, T. A. Davis, P. T. de Zeeuw, P.-A. Duc, E. Emsellem, S. Khochfar, H. Kuntschner, R. M. McDermid, R. Morganti, T. Naab, T. Oosterloo, M. Sarzi, N. Scott, P. Serra, A.-M. Weijmans, and L. M. Young. The ATLAS^{3D} project - XVII. Linking photometric and kinematic signatures of stellar discs in early-type galaxies. *MNRAS*, 432:1768–1795, July 2013. doi: 10.1093/mnras/sts315.

D. Krajnović, E. Emsellem, M. den Brok, R. A. Marino, K. B. Schmidt, M. Steinmetz, and P. M. Weilbacher. Climbing to the top of the galactic mass ladder: evidence for frequent prolate-like rotation among the most massive galaxies. *MNRAS*, 477: 5327–5337, July 2018. doi: 10.1093/mnras/sty1031.

A. Kronawitter, R. P. Saglia, O. Gerhard, and R. Bender. Orbital structure and mass distribution in elliptical galaxies. *A&AS*, 144:53–84, May 2000. doi: 10.1051/aas: 2000199.

J. M. D. Kruijssen, F. I. Pelupessy, H. J. G. L. M. Lamers, S. F. Portegies Zwart, and V. Icke. Modelling the formation and evolution of star cluster populations in galaxy simulations. *MNRAS*, 414:1339–1364, June 2011. doi: 10.1111/j.1365-2966.2011. 18467.x.

J. M. D. Kruijssen, J. L. Pfeffer, R. A. Crain, and N. Bastian. The E-MOSAICS project: tracing galaxy formation and assembly with the age-metallicity distribution of globular clusters. *arXiv e-prints*, April 2019.

A. Kundu and B. C. Whitmore. New Insights from Hubble Space Telescope Studies of Globular Cluster Systems. II. Analysis of 29 S0 Systems. *AJ*, 122:1251–1270, September 2001. doi: 10.1086/322095.

C. d. P. Lagos, J. Schaye, Y. Bahé, J. Van de Sande, S. T. Kay, D. Barnes, T. A. Davis, and C. Dalla Vecchia. The connection between mass, environment, and slow rotation in simulated galaxies. *MNRAS*, 476:4327–4345, June 2018. doi: 10.1093/mnras/sty489.

S. S. Larsen, J. P. Brodie, J. P. Huchra, D. A. Forbes, and C. J. Grillmair. Properties of Globular Cluster Systems in Nearby Early-Type Galaxies. *AJ*, 121:2974–2998, June 2001. doi: 10.1086/321081.

R. Leaman, D. A. VandenBerg, and J. T. Mendel. The bifurcated age-metallicity relation of Milky Way globular clusters and its implications for the accretion history of the galaxy. *MNRAS*, 436:122–135, November 2013. doi: 10.1093/mnras/stt1540.

M. G. Lee, H. S. Park, H. S. Hwang, N. Arimoto, N. Tamura, and M. Onodera. The Globular Cluster System of the Virgo Giant Elliptical Galaxy NGC 4636. II. Kinematics of the Globular Cluster System. *ApJ*, 709:1083–1099, February 2010. doi: 10.1088/0004-637X/709/2/1083.

G. Lemaître. Note on de Sitter's Universe. *Journal of Mathematical Physics*, 4(3): 188–192, January 1925. doi: 10.1002/sapm192541188.

G. Lemaître. Un Univers homogène de masse constante et de rayon croissant rendant compte de la vitesse radiale des nébuleuses extra-galactiques. *Annales de la Société Scientifique de Bruxelles*, 47:49–59, 1927.

G. Lemaître. The Beginning of the World from the Point of View of Quantum Theory. *Nature*, 127:706, May 1931. doi: 10.1038/127706b0.

C. Li and S. D. M. White. The distribution of stellar mass in the low-redshift Universe. *ArXiv e-prints*, January 2009.

H. Li, S. Mao, E. Emsellem, D. Xu, V. Springel, and D. Krajnović. The origin and properties of massive prolate galaxies in the Illustris simulation. *MNRAS*, 473:1489–1511, January 2018. doi: 10.1093/mnras/stx2374.

A. D. Linde. A new inflationary universe scenario: A possible solution of the horizon, flatness, homogeneity, isotropy and primordial monopole problems. *Physics Letters B*, 108:389–393, February 1982. doi: 10.1016/0370-2693(82)91219-9.

A. D. Linde. Chaotic inflation. *Physics Letters B*, 129:177–181, September 1983. doi: 10.1016/0370-2693(83)90837-7.

J. M. Lotz, J. Primack, and P. Madau. A New Nonparametric Approach to Galaxy Morphological Classification. *AJ*, 128:163–182, July 2004. doi: 10.1086/421849.

C.-P. Ma and E. Bertschinger. Cosmological Perturbation Theory in the Synchronous and Conformal Newtonian Gauges. *ApJ*, 455:7, December 1995. doi: 10.1086/176550.

C.-P. Ma, J. E. Greene, N. McConnell, R. Janish, J. P. Blakeslee, J. Thomas, and J. D. Murphy. The MASSIVE Survey. I. A Volume-limited Integral-field Spectroscopic Study of the Most Massive Early-type Galaxies within 108 Mpc. *ApJ*, 795:158, November 2014. doi: 10.1088/0004-637X/795/2/158.

P. Marigo. Chemical yields from low- and intermediate-mass stars: Model predictions and basic observational constraints. *A&A*, 370:194–217, April 2001. doi: 10.1051/0004-6361:20000247.

A. Marín-Franch, A. Aparicio, G. Piotto, A. Rosenberg, B. Chaboyer, A. Sarajedini, M. Siegel, J. Anderson, L. R. Bedin, A. Dotter, M. Hempel, I. King, S. Majewski, A. P. Milone, N. Paust, and I. N. Reid. The ACS Survey of Galactic Globular Clusters. VII. Relative Ages. *ApJ*, 694:1498–1516, April 2009. doi: 10.1088/0004-637X/694/2/1498.

S. Marri and S. D. M. White. Smoothed particle hydrodynamics for galaxy-formation simulations: improved treatments of multiphase gas, of star formation and of supernovae feedback. *MNRAS*, 345:561–574, October 2003. doi: 10.1046/j.1365-8711. 2003.06984.x.

C. E. Masters and K. M. Ashman. The Accretion of Dwarf Galaxies and Their Globular Cluster Systems. *ApJ*, 725:868–874, December 2010. doi: 10.1088/0004-637X/ 725/1/868.

K. L. Masters, A. Jordán, P. Côté, L. Ferrarese, J. P. Blakeslee, L. Infante, E. W. Peng, S. Mei, and M. J. West. The Advanced Camera for Surveys Fornax Cluster Survey. VII. Half-light Radii of Globular Clusters in Early-type Galaxies. *ApJ*, 715:1419– 1437, June 2010. doi: 10.1088/0004-637X/715/2/1419.

W. G. Mathews. The enormous mass of the elliptical galaxy M87 - A model for the extended X-ray source. *ApJ*, 219:413–423, January 1978. doi: 10.1086/155794.

S. McAlpine, J. C. Helly, M. Schaller, J. W. Trayford, Y. Qu, M. Furlong, R. G. Bower, R. A. Crain, J. Schaye, T. Theuns, C. Dalla Vecchia, C. S. Frenk, I. G. McCarthy, A. Jenkins, Y. Rosas-Guevara, S. D. M. White, M. Baes, P. Camps, and G. Lemson. The EAGLE simulations of galaxy formation: Public release of halo and galaxy catalogues. *Astronomy and Computing*, 15:72–89, April 2016. doi: 10.1016/j.ascom.2016.02.004.

I. G. McCarthy, A. S. Font, R. A. Crain, A. J. Deason, J. Schaye, and T. Theuns. Global structure and kinematics of stellar haloes in cosmological hydrodynamic simulations. *MNRAS*, 420:2245–2262, March 2012. doi: 10.1111/j.1365-2966.2011. 20189.x.

J. C. Mihos and L. Hernquist. Gasdynamics and Starbursts in Major Mergers. *ApJ*, 464:641, June 1996. doi: 10.1086/177353.

M. Milgrom. A modification of the Newtonian dynamics as a possible alternative to the hidden mass hypothesis. *ApJ*, 270:365–370, July 1983. doi: 10.1086/161130.

H. J. Mo, S. Mao, and S. D. M. White. The formation of galactic discs. *MNRAS*, 295: 319–336, April 1998. doi: 10.1046/j.1365-8711.1998.01227.x.

J. P. Morris. A study of the stability properties of smooth particle hydrodynamics. *PASA*, 13:97–102, January 1996.

J. F. Navarro and M. Steinmetz. The Effects of a Photoionizing Ultraviolet Background on the Formation of Disk Galaxies. *ApJ*, 478:13–28, March 1997. doi: 10.1086/303763.

P. Norberg, S. Cole, C. M. Baugh, C. S. Frenk, I. Baldry, J. Bland-Hawthorn, T. Bridges, R. Cannon, M. Colless, C. Collins, W. Couch, N. J. G. Cross, G. Dalton, R. De Propris, S. P. Driver, G. Efstathiou, R. S. Ellis, K. Glazebrook, C. Jackson, O. Lahav, I. Lewis, S. Lumsden, S. Maddox, D. Madgwick, J. A. Peacock, B. A. Peterson, W. Sutherland, K. Taylor, and 2DFGRS Team. The 2dF Galaxy Redshift Survey: the b_J-band galaxy luminosity function and survey selection function. *MNRAS*, 336:907–931, November 2002. doi: 10.1046/j.1365-8711.2002.05831.x.

T. Okamoto, A. Jenkins, V. R. Eke, V. Quilis, and C. S. Frenk. Momentum transfer across shear flows in smoothed particle hydrodynamic simulations of galaxy formation. *MNRAS*, 345:429–446, October 2003. doi: 10.1046/j.1365-8711.2003.06948.x.

T. Okamoto, V. R. Eke, C. S. Frenk, and A. Jenkins. Effects of feedback on the morphology of galaxy discs. *MNRAS*, 363:1299–1314, November 2005. doi: 10.1111/j.1365-2966.2005.09525.x.

E. Opik. An estimate of the distance of the Andromeda Nebula. *ApJ*, 55, June 1922. doi: 10.1086/142680.

B. D. Oppenheimer, R. A. Crain, J. Schaye, A. Rahmati, A. J. Richings, J. W. Trayford, J. Tumlinson, R. G. Bower, M. Schaller, and T. Theuns. Bimodality of low-redshift circumgalactic O VI in non-equilibrium EAGLE zoom simulations. *MNRAS*, 460: 2157–2179, August 2016. doi: 10.1093/mnras/stw1066.

J. P. Ostriker and P. J. E. Peebles. A Numerical Study of the Stability of Flattened Galaxies: or, can Cold Galaxies Survive? *ApJ*, 186:467–480, December 1973. doi: 10.1086/152513.

J. P. Ostriker and P. J. Steinhardt. The observational case for a low-density Universe with a non-zero cosmological constant. *Nature*, 377:600–602, October 1995. doi: 10.1038/377600a0.

J. P. Ostriker, P. J. E. Peebles, and A. Yahil. The size and mass of galaxies, and the mass of the universe. *ApJl*, 193:L1–L4, October 1974. doi: 10.1086/181617.

H. S. Park and M. G. Lee. Dual Halos and Formation of Early-type Galaxies. *ApJl*, 773:L27, August 2013. doi: 10.1088/2041-8205/773/2/L27.

P. J. E. Peebles. Large-scale background temperature and mass fluctuations due to scale-invariant primeval perturbations. *ApJl*, 263:L1–L5, December 1982. doi: 10.1086/183911.

P. J. E. Peebles and J. T. Yu. Primeval Adiabatic Perturbation in an Expanding Universe. *ApJ*, 162:815, December 1970. doi: 10.1086/150713.

C. Y. Peng, L. C. Ho, C. D. Impey, and H.-W. Rix. Detailed Structural Decomposition of Galaxy Images. *AJ*, 124:266–293, July 2002. doi: 10.1086/340952.

E. W. Peng, A. Jordán, P. Côté, J. P. Blakeslee, L. Ferrarese, S. Mei, M. J. West, D. Merritt, M. Milosavljević, and J. L. Tonry. The ACS Virgo Cluster Survey. IX. The Color Distributions of Globular Cluster Systems in Early-Type Galaxies. *ApJ*, 639:95–119, March 2006. doi: 10.1086/498210.

A. A. Penzias and R. W. Wilson. A Measurement of Excess Antenna Temperature at 4080 Mc/s. *ApJ*, 142:419–421, July 1965. doi: 10.1086/148307.

S. Perlmutter, G. Aldering, G. Goldhaber, R. A. Knop, P. Nugent, P. G. Castro, S. Deustua, S. Fabbro, A. Goobar, D. E. Groom, I. M. Hook, A. G. Kim, M. Y. Kim, J. C. Lee, N. J. Nunes, R. Pain, C. R. Pennypacker, R. Quimby, C. Lidman, R. S. Ellis, M. Irwin, R. G. McMahon, P. Ruiz-Lapuente, N. Walton, B. Schaefer,

B. J. Boyle, A. V. Filippenko, T. Matheson, A. S. Fruchter, N. Panagia, H. J. M. Newberg, W. J. Couch, and T. S. C. Project. Measurements of Ω and Λ from 42 High-Redshift Supernovae. *ApJ*, 517:565–586, June 1999. doi: 10.1086/307221.

V. Petrosian, E. Salpeter, and P. Szekeres. Quasi-Stellar Objects in Universes with Non-Zero Cosmological Constant. *ApJ*, 147:1222–1226, March 1967. doi: 10.1086/149122.

J. Pfeffer, J. M. D. Kruijssen, R. A. Crain, and N. Bastian. The E-MOSAICS project: simulating the formation and co-evolution of galaxies and their star cluster populations. *MNRAS*, 475:4309–4346, April 2018. doi: 10.1093/mnras/stx3124.

A. Pillepich, V. Springel, D. Nelson, S. Genel, J. Naiman, R. Pakmor, L. Hernquist, P. Torrey, M. Vogelsberger, R. Weinberger, and F. Marinacci. Simulating galaxy formation with the IllustrisTNG model. *MNRAS*, 473:4077–4106, January 2018. doi: 10.1093/mnras/stx2656.

Planck Collaboration. Planck 2013 results. I. Overview of products and scientific results. *A&A*, 571:A1, November 2014. doi: 10.1051/0004-6361/201321529.

Planck Collaboration. *arXiv e-prints*, July 2018.

Planck Collaboration, P. A. R. Ade, N. Aghanim, M. I. R. Alves, C. Armitage-Caplan, M. Arnaud, M. Ashdown, F. Atrio-Barandela, J. Aumont, H. Aussel, and et al. Planck 2013 results. I. Overview of products and scientific results. *A&A*, 571:A1, November 2014. doi: 10.1051/0004-6361/201321529.

H. Poincaré. The Milky Way and the Theory of Gases. *Popular Astronomy*, 14:475–488, October 1906.

S. F. Portegies Zwart, S. L. W. McMillan, and M. Gieles. Young Massive Star Clusters. *ARA&A*, 48:431–493, September 2010. doi: 10.1146/annurev-astro-081309-130834.

L. Portinari, C. Chiosi, and A. Bressan. Galactic chemical enrichment with new metallicity dependent stellar yields. *A&A*, 334:505–539, June 1998.

V. Pota, D. A. Forbes, A. J. Romanowsky, J. P. Brodie, L. R. Spitler, J. Strader, C. Foster, J. A. Arnold, A. Benson, C. Blom, J. R. Hargis, K. L. Rhode, and C. Usher. The SLUGGS Survey: kinematics for over 2500 globular clusters in 12 early-type galaxies. *MNRAS*, 428:389–420, January 2013. doi: 10.1093/mnras/sts029.

W. H. Press and P. Schechter. Formation of Galaxies and Clusters of Galaxies by Self-Similar Gravitational Condensation. *ApJ*, 187:425–438, February 1974. doi: 10.1086/152650.

D. J. Price. Modelling discontinuities and Kelvin Helmholtz instabilities in SPH. *Journal of Computational Physics*, 227:10040–10057, December 2008. doi: 10.1016/j.jcp.2008.08.011.

D. J. Price and C. Federrath. A comparison between grid and particle methods on the statistics of driven, supersonic, isothermal turbulence. *MNRAS*, 406:1659–1674, August 2010. doi: 10.1111/j.1365-2966.2010.16810.x.

R. N. Proctor, D. A. Forbes, A. J. Romanowsky, J. P. Brodie, J. Strader, M. Spolaor, J. T. Mendel, and L. Spitler. Probing the 2D kinematic structure of early-type galaxies out to three effective radii. *MNRAS*, 398:91–108, September 2009. doi: 10.1111/j.1365-2966.2009.15137.x.

T. H. Puzia, M. Kissler-Patig, D. Thomas, C. Maraston, R. P. Saglia, R. Bender, P. Goudfrooij, and M. Hempel. VLT spectroscopy of globular cluster systems. II. Spectroscopic ages, metallicities, and [α/Fe] ratios of globular clusters in early-type galaxies. *A&A*, 439:997–1011, September 2005. doi: 10.1051/0004-6361: 20047012.

Y. Qu, J. C. Helly, R. G. Bower, T. Theuns, R. A. Crain, C. S. Frenk, M. Furlong, S. McAlpine, M. Schaller, J. Schaye, and S. D. M. White. A chronicle of galaxy mass assembly in the EAGLE simulation. *ArXiv e-prints*, September 2016.

K. U. Ratnatunga, R. E. Griffiths, and E. J. Ostrander. Disk and Bulge Morphology of WFPC2 Galaxies: The HUBBLE SPACE TELESCOPE Medium Deep Survey. *AJ*, 118:86–107, July 1999. doi: 10.1086/300931.

A. G. Riess, A. V. Filippenko, P. Challis, A. Clocchiatti, A. Diercks, P. M. Garnavich, R. L. Gilliland, C. J. Hogan, S. Jha, R. P. Kirshner, B. Leibundgut, M. M. Phillips, D. Reiss, B. P. Schmidt, R. A. Schommer, R. C. Smith, J. Spyromilio, C. Stubbs, N. B. Suntzeff, and J. Tonry. Observational Evidence from Supernovae for an Accelerating Universe and a Cosmological Constant. *AJ*, 116:1009–1038, September 1998. doi: 10.1086/300499.

B. W. Ritchie and P. A. Thomas. Multiphase smoothed-particle hydrodynamics. *MNRAS*, 323:743–756, May 2001. doi: 10.1046/j.1365-8711.2001.04268.x.

P. H. Roberts. On the Superpotential and Supermatrix of a Heterogeneous Ellipsoid. *ApJ*, 136:1108, November 1962. doi: 10.1086/147461.

B. Robertson, T. J. Cox, L. Hernquist, M. Franx, P. F. Hopkins, P. Martini, and V. Springel. The Fundamental Scaling Relations of Elliptical Galaxies. *ApJ*, 641: 21–40, April 2006. doi: 10.1086/500360.

A. S. G. Robotham, D. S. Taranu, R. Tobar, A. Moffett, and S. P. Driver. PROFIT: Bayesian profile fitting of galaxy images. *MNRAS*, 466:1513–1541, April 2017. doi: 10.1093/mnras/stw3039.

A. J. Romanowsky and S. M. Fall. Angular Momentum and Galaxy Formation Revisited. *ApJS*, 203:17, December 2012. doi: 10.1088/0067-0049/203/2/17.

Y. M. Rosas-Guevara, R. G. Bower, J. Schaye, M. Furlong, C. S. Frenk, C. M. Booth, R. A. Crain, C. Dalla Vecchia, M. Schaller, and T. Theuns. The impact of angular momentum on black hole accretion rates in simulations of galaxy formation. *MNRAS*, 454:1038–1057, November 2015. doi: 10.1093/mnras/stv2056.

A. Rosenberg, I. Saviane, G. Piotto, and A. Aparicio. Galactic Globular Cluster Relative Ages. *AJ*, 118:2306–2320, November 1999. doi: 10.1086/301089.

V. C. Rubin and W. K. Ford, Jr. Rotation of the Andromeda Nebula from a Spectroscopic Survey of Emission Regions. *ApJ*, 159:379, February 1970. doi: 10.1086/150317.

V. C. Rubin, W. K. Ford, Jr., and N. Thonnard. Rotational properties of 21 SC galaxies with a large range of luminosities and radii, from NGC 4605 /R = 4kpc/ to UGC 2885 /R = 122 kpc/. *ApJ*, 238:471–487, June 1980. doi: 10.1086/158003.

R. K. Sachs and A. M. Wolfe. Perturbations of a Cosmological Model and Angular Variations of the Microwave Background. *ApJ*, 147:73, January 1967. doi: 10.1086/148982.

L. V. Sales, J. F. Navarro, J. Schaye, C. Dalla Vecchia, V. Springel, and C. M. Booth. Feedback and the structure of simulated galaxies at redshift z= 2. *MNRAS*, 409: 1541–1556, December 2010. doi: 10.1111/j.1365-2966.2010.17391.x.

L. V. Sales, J. F. Navarro, T. Theuns, J. Schaye, S. D. M. White, C. S. Frenk, R. A. Crain, and C. Dalla Vecchia. The origin of discs and spheroids in simulated galaxies. *MNRAS*, 423:1544–1555, June 2012. doi: 10.1111/j.1365-2966.2012.20975.x.

S. Salim, R. M. Rich, S. Charlot, J. Brinchmann, B. D. Johnson, D. Schiminovich, M. Seibert, R. Mallery, T. M. Heckman, K. Forster, P. G. Friedman, D. C. Martin, P. Morrissey, S. G. Neff, T. Small, T. K. Wyder, L. Bianchi, J. Donas, Y.-W. Lee, B. F. Madore, B. Milliard, A. S. Szalay, B. Y. Welsh, and S. K. Yi. UV Star Formation Rates in the Local Universe. *ApJS*, 173:267–292, December 2007. doi: 10.1086/519218.

S. F. Sánchez, R. C. Kennicutt, A. Gil de Paz, G. van de Ven, J. M. Vílchez, L. Wisotzki, C. J. Walcher, D. Mast, J. A. L. Aguerri, S. Albiol-Pérez, A. Alonso-Herrero, J. Alves, J. Bakos, T. Bartáková, J. Bland-Hawthorn, A. Boselli, D. J. Bomans, A. Castillo-Morales, C. Cortijo-Ferrero, A. de Lorenzo-Cáceres, A. Del Olmo, R.-J. Dettmar, A. Díaz, S. Ellis, J. Falcón-Barroso, H. Flores, A. Gallazzi, B. García-Lorenzo, R. González Delgado, N. Gruel, T. Haines, C. Hao, B. Husemann, J. Iglésias-Páramo, K. Jahnke, B. Johnson, B. Jungwiert, V. Kalinova, C. Kehrig, D. Kupko, Á. R. López-Sánchez, M. Lyubenova, R. A. Marino, E. Mármol-Queraltó, I. Márquez, J. Masegosa, S. Meidt, J. Mendez-Abreu, A. Monreal-Ibero, C. Montijo, A. M. Mourão, G. Palacios-Navarro, P. Papaderos,

A. Pasquali, R. Peletier, E. Pérez, I. Pérez, A. Quirrenbach, M. Relaño, F. F. Rosales-Ortega, M. M. Roth, T. Ruiz-Lara, P. Sánchez-Blázquez, C. Sengupta, R. Singh, V. Stanishev, S. C. Trager, A. Vazdekis, K. Viironen, V. Wild, S. Zibetti, and B. Ziegler. CALIFA, the Calar Alto Legacy Integral Field Area survey. I. Survey presentation. *A&A*, 538:A8, February 2012. doi: 10.1051/0004-6361/201117353.

R. Sancisi, F. Fraternali, T. Oosterloo, and T. van der Hulst. Cold gas accretion in galaxies. *A&A Rev.*, 15:189–223, June 2008. doi: 10.1007/s00159-008-0010-0.

K. Sato. First-order phase transition of a vacuum and the expansion of the Universe. *MNRAS*, 195:467–479, May 1981. doi: 10.1093/mnras/195.3.467.

T. Sawala, C. S. Frenk, A. Fattahi, J. F. Navarro, R. G. Bower, R. A. Crain, C. Dalla Vecchia, M. Furlong, A. Jenkins, I. G. McCarthy, Y. Qu, M. Schaller, J. Schaye, and T. Theuns. Bent by baryons: the low-mass galaxy-halo relation. *MNRAS*, 448: 2941–2947, April 2015. doi: 10.1093/mnras/stu2753.

T. Sawala, C. S. Frenk, A. Fattahi, J. F. Navarro, R. G. Bower, R. A. Crain, C. Dalla Vecchia, M. Furlong, J. C. Helly, A. Jenkins, K. A. Oman, M. Schaller, J. Schaye, T. Theuns, J. Trayford, and S. D. M. White. The APOSTLE simulations: solutions to the Local Group's cosmic puzzles. *MNRAS*, 457:1931–1943, April 2016. doi: 10.1093/mnras/stw145.

C. Scannapieco, P. B. Tissera, S. D. M. White, and V. Springel. Effects of supernova feedback on the formation of galaxy discs. *MNRAS*, 389:1137–1149, September 2008. doi: 10.1111/j.1365-2966.2008.13678.x.

C. Scannapieco, M. Wadepuhl, O. H. Parry, J. F. Navarro, A. Jenkins, V. Springel, R. Teyssier, E. Carlson, H. M. P. Couchman, R. A. Crain, C. Dalla Vecchia, C. S. Frenk, C. Kobayashi, P. Monaco, G. Murante, T. Okamoto, T. Quinn, J. Schaye, G. S. Stinson, T. Theuns, J. Wadsley, S. D. M. White, and R. Woods. The Aquila comparison project: the effects of feedback and numerical methods on simulations of galaxy formation. *MNRAS*, 423:1726–1749, June 2012. doi: 10.1111/j.1365-2966.2012.20993.x.

D. Schade, S. J. Lilly, D. Crampton, F. Hammer, O. Le Fevre, and L. Tresse. Canada-France Redshift Survey: Hubble Space Telescope Imaging of High-Redshift Field Galaxies. *ApJl*, 451:L1, September 1995. doi: 10.1086/309677.

D. Schade, S. J. Lilly, O. Le Fevre, F. Hammer, and D. Crampton. Canada-France Redshift Survey. XI. Morphology of High-Redshift Field Galaxies from High-Resolution Ground-based Imaging. *ApJ*, 464:79, June 1996. doi: 10.1086/177301.

M. Schaller, C. S. Frenk, R. G. Bower, T. Theuns, A. Jenkins, J. Schaye, R. A. Crain, M. Furlong, C. Dalla Vecchia, and I. G. McCarthy. Baryon effects on the internal structure of ΛCDM haloes in the EAGLE simulations. *MNRAS*, 451:1247–1267, August 2015a. doi: 10.1093/mnras/stv1067.

M. Schaller et al. The EAGLE simulations of galaxy formation: the importance of the hydrodynamics scheme. *MNRAS*, 454:2277–2291, December 2015b. doi: 10.1093/mnras/stv2169.

K. Schawinski, C. M. Urry, B. D. Simmons, L. Fortson, S. Kaviraj, W. C. Keel, C. J. Lintott, K. L. Masters, R. C. Nichol, M. Sarzi, R. Skibba, E. Treister, K. W. Willett, O. I. Wong, and S. K. Yi. The green valley is a red herring: Galaxy Zoo reveals two evolutionary pathways towards quenching of star formation in early- and late-type galaxies. *MNRAS*, 440:889–907, May 2014. doi: 10.1093/mnras/stu327.

J. Schaye. Star Formation Thresholds and Galaxy Edges: Why and Where. *ApJ*, 609:667–682, July 2004. doi: 10.1086/421232.

J. Schaye and C. Dalla Vecchia. On the relation between the Schmidt and Kennicutt-Schmidt star formation laws and its implications for numerical simulations. *MNRAS*, 383:1210–1222, January 2008. doi: 10.1111/j.1365-2966.2007.12639.x.

J. Schaye, R. A. Crain, R. G. Bower, M. Furlong, M. Schaller, T. Theuns, C. Dalla Vecchia, C. S. Frenk, I. G. McCarthy, J. C. Helly, A. Jenkins, Y. M. Rosas-Guevara, S. D. M. White, M. Baes, C. M. Booth, P. Camps, J. F. Navarro, Y. Qu, A. Rahmati, T. Sawala, P. A. Thomas, and J. Trayford. The EAGLE project: simulating the

evolution and assembly of galaxies and their environments. *MNRAS*, 446:521–554, January 2015. doi: 10.1093/mnras/stu2058.

P. Schechter. An analytic expression for the luminosity function for galaxies. *ApJ*, 203:297–306, January 1976. doi: 10.1086/154079.

M. D. Schneider, C. S. Frenk, and S. Cole. The shapes and alignments of dark matter halos. *J. Cosmology Astropart. Phys.*, 5:030, May 2012. doi: 10.1088/1475-7516/2012/05/030.

L. L. Schroder, J. P. Brodie, M. Kissler-Patig, J. P. Huchra, and A. C. Phillips. Spectroscopy of Globular Clusters in M81. *AJ*, 123:2473–2489, May 2002. doi: 10.1086/322994.

J. L. Sérsic. Influence of the atmospheric and instrumental dispersion on the brightness distribution in a galaxy. *Boletin de la Asociacion Argentina de Astronomia La Plata Argentina*, 6:41, 1963.

J. L. Sérsic. *Atlas de galaxias australes*. 1968.

H. Shapley. On the Existence of External Galaxies. *PASP*, 31:261, October 1919. doi: 10.1086/122870.

H. Shapley and H. D. Curtis. The Scale of the Universe. *Bulletin of the National Research Council, Vol. 2, Part 3, No. 11, p. 171-217*, 2:171–217, May 1921.

J. Shklovsky. On the Nature of "standard" Absorption Spectrum of the Quasi-Stellar Objects. *ApJl*, 150:L1, October 1967. doi: 10.1086/180079.

D. Sijacki, M. Vogelsberger, D. Kereš, V. Springel, and L. Hernquist. Moving mesh cosmology: the hydrodynamics of galaxy formation. *MNRAS*, 424:2999–3027, August 2012. doi: 10.1111/j.1365-2966.2012.21466.x.

J. Silk. Fluctuations in the Primordial Fireball. *Nature*, 215:1155–1156, September 1967. doi: 10.1038/2151155a0.

J. Silk. Cosmic Black-Body Radiation and Galaxy Formation. *ApJ*, 151:459, February 1968. doi: 10.1086/149449.

J. Silk and M. J. Rees. Quasars and galaxy formation. *A&A*, 331:L1–L4, March 1998.

L. Simard. GIM2D: an IRAF package for the Quantitative Morphology Analysis of Distant Galaxies. In R. Albrecht, R. N. Hook, and H. A. Bushouse, editors, *Astronomical Data Analysis Software and Systems VII*, volume 145 of *Astronomical Society of the Pacific Conference Series*, page 108, 1998.

L. Simard, C. N. A. Willmer, N. P. Vogt, V. L. Sarajedini, A. C. Phillips, B. J. Weiner, D. C. Koo, M. Im, G. D. Illingworth, and S. M. Faber. The DEEP Groth Strip Survey. II. Hubble Space Telescope Structural Parameters of Galaxies in the Groth Strip. *ApJS*, 142:1–33, September 2002. doi: 10.1086/341399.

F. Simien and P. Prugniel. Kinematical data on early-type galaxies. V. *A&AS*, 145: 263–267, August 2000. doi: 10.1051/aas:2000241.

B. Sinnott, A. Hou, R. Anderson, W. E. Harris, and K. A. Woodley. New g'r'i'z' Photometry of the NGC 5128 Globular Cluster System. *AJ*, 140:2101–2108, December 2010. doi: 10.1088/0004-6256/140/6/2101.

V. M. Slipher. The radial velocity of the Andromeda Nebula. *Lowell Observatory Bulletin*, 2:56–57, 1913.

V. M. Slipher. Spectrographic Observations of Nebulae. *Popular Astronomy*, 23:21–24, January 1915.

V. M. Slipher. Nebulae. *Proceedings of the American Philosophical Society*, 56:403–409, 1917.

G. F. Smoot, C. L. Bennett, A. Kogut, E. L. Wright, J. Aymon, N. W. Boggess, E. S. Cheng, G. de Amici, S. Gulkis, M. G. Hauser, G. Hinshaw, P. D. Jackson, M. Janssen, E. Kaita, T. Kelsall, P. Keegstra, C. Lineweaver, K. Loewenstein, P. Lubin, J. Mather, S. S. Meyer, S. H. Moseley, T. Murdock, L. Rokke, R. F. Silverberg, L. Tenorio, R. Weiss, and D. T. Wilkinson. Structure in the COBE differential

microwave radiometer first-year maps. *ApJl*, 396:L1–L5, September 1992. doi: 10.1086/186504.

J. Sommer-Larsen and M. Limousin. Moderate steepening of galaxy cluster dark matter profiles by baryonic pinching. *MNRAS*, 408:1998–2007, November 2010. doi: 10.1111/j.1365-2966.2010.17260.x.

D. N. Spergel, L. Verde, H. V. Peiris, E. Komatsu, M. R. Nolta, C. L. Bennett, M. Halpern, G. Hinshaw, N. Jarosik, A. Kogut, M. Limon, S. S. Meyer, L. Page, G. S. Tucker, J. L. Weiland, E. Wollack, and E. L. Wright. First-Year Wilkinson Microwave Anisotropy Probe (WMAP) Observations: Determination of Cosmological Parameters. *ApJS*, 148:175–194, September 2003. doi: 10.1086/377226.

D. N. Spergel, R. Bean, O. Doré, M. R. Nolta, C. L. Bennett, J. Dunkley, G. Hinshaw, N. Jarosik, E. Komatsu, L. Page, H. V. Peiris, L. Verde, M. Halpern, R. S. Hill, A. Kogut, M. Limon, S. S. Meyer, N. Odegard, G. S. Tucker, J. L. Weiland, E. Wollack, and E. L. Wright. Three-Year Wilkinson Microwave Anisotropy Probe (WMAP) Observations: Implications for Cosmology. *ApJS*, 170:377–408, June 2007. doi: 10.1086/513700.

V. Springel. The cosmological simulation code GADGET-2. *MNRAS*, 364:1105–1134, December 2005. doi: 10.1111/j.1365-2966.2005.09655.x.

V. Springel and L. Hernquist. The history of star formation in a Λ cold dark matter universe. *MNRAS*, 339:312–334, February 2003. doi: 10.1046/j.1365-8711.2003.06207.x.

V. Springel, S. D. M. White, G. Tormen, and G. Kauffmann. Populating a cluster of galaxies - I. Results at $z = 0$. *MNRAS*, 328:726–750, December 2001. doi: 10.1046/j.1365-8711.2001.04912.x.

V. Springel, S. D. M. White, and L. Hernquist. The shapes of simulated dark matter halos. In S. Ryder, D. Pisano, M. Walker, and K. Freeman, editors, *Dark Matter in Galaxies*, volume 220 of *IAU Symposium*, page 421, July 2004.

V. Springel, T. Di Matteo, and L. Hernquist. Modelling feedback from stars and black holes in galaxy mergers. *MNRAS*, 361:776–794, August 2005. doi: 10.1111/j. 1365-2966.2005.09238.x.

V. Springel, R. Pakmor, A. Pillepich, R. Weinberger, D. Nelson, L. Hernquist, M. Vogelsberger, S. Genel, P. Torrey, F. Marinacci, and J. Naiman. First results from the IllustrisTNG simulations: matter and galaxy clustering. *MNRAS*, 475:676–698, March 2018. doi: 10.1093/mnras/stx3304.

A. A. Starobinsky. A new type of isotropic cosmological models without singularity. *Physics Letters B*, 91:99–102, March 1980. doi: 10.1016/0370-2693(80)90670-X.

J. P. Stott, A. M. Swinbank, H. L. Johnson, A. Tiley, G. Magdis, R. Bower, A. J. Bunker, M. Bureau, C. M. Harrison, M. J. Jarvis, R. Sharples, I. Smail, D. Sobral, P. Best, and M. Cirasuolo. The KMOS Redshift One Spectroscopic Survey (KROSS): dynamical properties, gas and dark matter fractions of typical z   1 star-forming galaxies. *MNRAS*, 457:1888–1904, April 2016. doi: 10.1093/mnras/ stw129.

J. Strader, J. P. Brodie, A. J. Cenarro, M. A. Beasley, and D. A. Forbes. Extragalactic Globular Clusters: Old Spectroscopic Ages and New Views on Their Formation. *AJ*, 130:1315–1323, October 2005. doi: 10.1086/432717.

J. Strader, A. J. Romanowsky, J. P. Brodie, L. R. Spitler, M. A. Beasley, J. A. Arnold, N. Tamura, R. M. Sharples, and N. Arimoto. Wide-field Precision Kinematics of the M87 Globular Cluster System. *ApJS*, 197:33, December 2011. doi: 10.1088/ 0067-0049/197/2/33.

I. Strateva, Ž. Ivezić, G. R. Knapp, V. K. Narayanan, M. A. Strauss, J. E. Gunn, R. H. Lupton, D. Schlegel, N. A. Bahcall, J. Brinkmann, R. J. Brunner, T. Budavári, I. Csabai, F. J. Castander, M. Doi, M. Fukugita, Z. Győry, M. Hamabe, G. Hennessy, T. Ichikawa, P. Z. Kunszt, D. Q. Lamb, T. A. McKay, S. Okamura, J. Racusin, M. Sekiguchi, D. P. Schneider, K. Shimasaku, and D. York. Color Sep-

aration of Galaxy Types in the Sloan Digital Sky Survey Imaging Data. *AJ*, 122:
1861–1874, October 2001. doi: 10.1086/323301.

A. M. Swinbank, C. M. Harrison, J. Trayford, M. Schaller, I. Smail, J. Schaye, T. Theuns, R. Smit, D. M. Alexander, R. Bacon, R. G. Bower, T. Contini, R. A. Crain, C. de Breuck, R. Decarli, B. Epinat, M. Fumagalli, M. Furlong, A. Galametz, H. L. Johnson, C. Lagos, J. Richard, J. Vernet, R. M. Sharples, D. Sobral, and J. P. Stott. Angular momentum evolution of galaxies over the past 10 Gyr: a MUSE and KMOS dynamical survey of 400 star-forming galaxies from z = 0.3 to 1.7. *MNRAS*, 467: 3140–3159, May 2017. doi: 10.1093/mnras/stx201.

A. R. Tomczak, R. F. Quadri, K.-V. H. Tran, I. Labbé, C. M. S. Straatman, C. Papovich, K. Glazebrook, R. Allen, G. B. Brammer, G. G. Kacprzak, L. Kawinwanichakij, D. D. Kelson, P. J. McCarthy, N. Mehrtens, A. J. Monson, S. E. Persson, L. R. Spitler, V. Tilvi, and P. van Dokkum. Galaxy Stellar Mass Functions from ZFOURGE/CANDELS: An Excess of Low-mass Galaxies since z = 2 and the Rapid Buildup of Quiescent Galaxies. *ApJ*, 783:85, March 2014. doi: 10.1088/0004-637X/783/2/85.

J. W. Trayford, T. Theuns, R. G. Bower, J. Schaye, M. Furlong, M. Schaller, C. S. Frenk, R. A. Crain, C. Dalla Vecchia, and I. G. McCarthy. Colours and luminosities of z = 0.1 galaxies in the EAGLE simulation. *MNRAS*, 452:2879–2896, September 2015. doi: 10.1093/mnras/stv1461.

J. W. Trayford, T. Theuns, R. G. Bower, R. A. Crain, C. d. P. Lagos, M. Schaller, and J. Schaye. It is not easy being green: the evolution of galaxy colour in the EAGLE simulation. *MNRAS*, 460:3925–3939, August 2016. doi: 10.1093/mnras/stw1230.

J. W. Trayford, P. Camps, T. Theuns, M. Baes, R. G. Bower, R. A. Crain, M. L. P. Gunawardhana, M. Schaller, J. Schaye, and C. S. Frenk. Optical colours and spectral indices of z = 0.1 eagle galaxies with the 3D dust radiative transfer code skirt. *MNRAS*, 470:771–799, September 2017. doi: 10.1093/mnras/stx1051.

J. W. Trayford, C. S. Frenk, T. Theuns, J. Schaye, and C. Correa. The star formation

rate and stellar content contributions of morphological components in the EAGLE simulations. *MNRAS*, 483:744–766, February 2019. doi: 10.1093/mnras/sty2860.

A. Tsatsi, M. Lyubenova, G. van de Ven, J. Chang, J. A. L. Aguerri, J. Falcón-Barroso, and A. V. Macciò. CALIFA reveals prolate rotation in massive early-type galaxies: A polar galaxy merger origin? *A&A*, 606:A62, October 2017. doi: 10.1051/0004-6361/201630218.

M. S. Turner, G. Steigman, and L. M. Krauss. Flatness of the universe - Reconciling theoretical prejudices with observational data. *Physical Review Letters*, 52:2090–2093, June 1984. doi: 10.1103/PhysRevLett.52.2090.

J. A. Tyson, F. Valdes, and R. A. Wenk. Detection of systematic gravitational lens galaxy image alignments - Mapping dark matter in galaxy clusters. *ApJl*, 349:L1–L4, January 1990. doi: 10.1086/185636.

J. M. Uson and D. T. Wilkinson. New limits on small-scale anisotropy in the microwave background. *ApJl*, 277:L1–L3, February 1984. doi: 10.1086/184188.

J. van de Sande, J. Bland-Hawthorn, S. Brough, S. M. Croom, L. Cortese, C. Foster, N. Scott, J. J. Bryant, F. d'Eugenio, C. Tonini, M. Goodwin, I. S. Konstantopoulos, J. S. Lawrence, A. M. Medling, M. S. Owers, S. N. Richards, A. L. Schaefer, and S. K. Yi. The SAMI Galaxy Survey: revising the fraction of slow rotators in IFS galaxy surveys. *MNRAS*, 472:1272–1285, December 2017. doi: 10.1093/mnras/stx1751.

J. van de Sande, C. D. P. Lagos, C. Welker, J. Bland-Hawthorn, F. Schulze, R.-S. Remus, Y. Bahé, S. Brough, J. J. Bryant, L. Cortese, S. M. Croom, J. Devriendt, Y. Dubois, M. Goodwin, I. S. Konstantopoulos, J. S. Lawrence, A. M. Medling, C. Pichon, S. N. Richards, S. F. Sanchez, N. Scott, and S. M. Sweet. The SAMI Galaxy Survey: comparing 3D spectroscopic observations with galaxies from cosmological hydrodynamical simulations. *MNRAS*, December 2018a. doi: 10.1093/mnras/sty3506.

J. van de Sande, N. Scott, J. Bland-Hawthorn, S. Brough, J. J. Bryant, M. Colless, L. Cortese, S. M. Croom, F. d'Eugenio, C. Foster, M. Goodwin, I. S. Konstantopoulos, J. S. Lawrence, R. M. McDermid, A. M. Medling, M. S. Owers, S. N. Richards, and R. Sharp. A relation between the characteristic stellar ages of galaxies and their intrinsic shapes. *Nature Astronomy*, 2:483–488, June 2018b. doi: 10.1038/s41550-018-0436-x.

R. P. van der Marel and M. Franx. A new method for the identification of non-Gaussian line profiles in elliptical galaxies. *ApJ*, 407:525–539, April 1993. doi: 10.1086/ 172534.

P. van Dokkum, S. Danieli, Y. Cohen, A. Merritt, A. J. Romanowsky, R. Abraham, J. Brodie, C. Conroy, D. Lokhorst, L. Mowla, E. O'Sullivan, and J. Zhang. A galaxy lacking dark matter. *Nature*, 555:629–632, March 2018. doi: 10.1038/nature25767.

D. A. VandenBerg, K. Brogaard, R. Leaman, and L. Casagrande. The Ages of 55 Globular Clusters as Determined Using an Improved \Delta V^HB_TO Method along with Color-Magnitude Diagram Constraints, and Their Implications for Broader Issues. *ApJ*, 775:134, October 2013. doi: 10.1088/0004-637X/775/2/134.

M. Velliscig, M. Cacciato, J. Schaye, R. A. Crain, R. G. Bower, M. P. van Daalen, C. Dalla Vecchia, C. S. Frenk, M. Furlong, I. G. McCarthy, M. Schaller, and T. Theuns. The alignment and shape of dark matter, stellar, and hot gas distributions in the EAGLE and cosmo-OWLS simulations. *MNRAS*, 453:721–738, October 2015a. doi: 10.1093/mnras/stv1690.

M. Velliscig, M. Cacciato, J. Schaye, H. Hoekstra, R. G. Bower, R. A. Crain, M. P. van Daalen, M. Furlong, I. G. McCarthy, M. Schaller, and T. Theuns. Intrinsic alignments of galaxies in the EAGLE and cosmo-OWLS simulations. *MNRAS*, 454: 3328–3340, December 2015b. doi: 10.1093/mnras/stv2198.

M. Vogelsberger, S. Genel, V. Springel, P. Torrey, D. Sijacki, D. Xu, G. Snyder, D. Nelson, and L. Hernquist. Introducing the Illustris Project: simulating the coevolution

of dark and visible matter in the Universe. *MNRAS*, 444:1518–1547, October 2014. doi: 10.1093/mnras/stu1536.

R. H. Wechsler and J. L. Tinker. The Connection Between Galaxies and Their Dark Matter Halos. *ARA&A*, 56:435–487, September 2018. doi: 10.1146/ annurev-astro-081817-051756.

A.-M. Weijmans, M. Cappellari, R. Bacon, P. T. de Zeeuw, E. Emsellem, J. Falcón-Barroso, H. Kuntschner, R. M. McDermid, R. C. E. van den Bosch, and G. van de Ven. Stellar velocity profiles and line strengths out to four effective radii in the early-type galaxies NGC3379 and 821. *MNRAS*, 398:561–574, September 2009. doi: 10.1111/j.1365-2966.2009.15134.x.

C. Welker, C. Power, C. Pichon, Y. Dubois, J. Devriendt, and S. Codis. Caught in the rhythm II: Competitive alignments of satellites with their inner halo and central galaxy. *ArXiv e-prints*, December 2017.

C. Welker, Y. Dubois, C. Pichon, J. Devriendt, and N. E. Chisari. Caught in the rhythm. I. How satellites settle into a plane around their central galaxy. *A&A*, 613:A4, May 2018. doi: 10.1051/0004-6361/201629007.

H. Wendland. Piecewise polynomial, positive definite and compactly supported radial functions of minimal degree. *Advances in Computational Mathematics*, 04:389–396, May 1995. ISSN 1572-9044. doi: 10.1007/BF02123482.

S. D. M. White and M. J. Rees. Core condensation in heavy halos - A two-stage theory for galaxy formation and clustering. *MNRAS*, 183:341–358, May 1978. doi: 10.1093/mnras/183.3.341.

S. D. M. White, C. S. Frenk, and M. Davis. Clustering in a neutrino-dominated universe. *ApJl*, 274:L1–L5, November 1983. doi: 10.1086/184139.

B. C. Whitmore, W. B. Sparks, R. A. Lucas, F. D. Macchetto, and J. A. Biretta. Hubble Space Telescope Observations of Globular Clusters in M87 and an Estimate of H 0. *ApJl*, 454:L73, December 1995. doi: 10.1086/309788.

M. Whittle. The observed galaxy mass function. URL `http://people.virginia.edu/~dmw8f/astr5630/Topic04/t4_LF_origin_B.html`.

R. P. C. Wiersma, J. Schaye, and B. D. Smith. The effect of photoionization on the cooling rates of enriched, astrophysical plasmas. *MNRAS*, 393:99–107, February 2009a. doi: 10.1111/j.1365-2966.2008.14191.x.

R. P. C. Wiersma, J. Schaye, T. Theuns, C. Dalla Vecchia, and L. Tornatore. Chemical enrichment in cosmological, smoothed particle hydrodynamics simulations. *MNRAS*, 399:574–600, October 2009b. doi: 10.1111/j.1365-2966.2009.15331.x.

Wikimedia Commons. The hubble sequence: classification of galaxies. URL `https://commons.wikimedia.org/wiki/File:Hubble_sequence_photo.png`. File:Hubble sequence photo.png.

M. L. Wilson and J. Silk. On the anisotropy of the cosmological background matter and radiation distribution. I - The radiation anisotropy in a spatially flat universe. *ApJ*, 243:14–25, January 1981. doi: 10.1086/158561.

E. Wisnioski, N. M. Förster Schreiber, S. Wuyts, E. Wuyts, K. Bandara, D. Wilman, R. Genzel, R. Bender, R. Davies, M. Fossati, P. Lang, J. T. Mendel, A. Beifiori, G. Brammer, J. Chan, M. Fabricius, Y. Fudamoto, S. Kulkarni, J. Kurk, D. Lutz, E. J. Nelson, I. Momcheva, D. Rosario, R. Saglia, S. Seitz, L. J. Tacconi, and P. G. van Dokkum. The KMOS^{3D} Survey: Design, First Results, and the Evolution of Galaxy Kinematics from $0.7 < z < 2.7$. *ApJ*, 799:209, February 2015. doi: 10.1088/0004-637X/799/2/209.

E. L. Wright, S. S. Meyer, C. L. Bennett, N. W. Boggess, E. S. Cheng, M. G. Hauser, A. Kogut, C. Lineweaver, J. C. Mather, G. F. Smoot, R. Weiss, S. Gulkis, G. Hinshaw, M. Janssen, T. Kelsall, P. M. Lubin, S. H. Moseley, Jr., T. L. Murdock, R. A. Shafer, R. F. Silverberg, and D. T. Wilkinson. Interpretation of the cosmic microwave background radiation anisotropy detected by the COBE Differential Microwave Radiometer. *ApJl*, 396:L13–L18, September 1992. doi: 10.1086/186506.

T. Wright. *An original theory or new hypothesis of the universe : founded upon general phaenomena of the visible creation; and particularly the Via the laws of nature, and solving by mathematical principles : the Lactea ...compris'd in nine familiar letters from the author to his friendand : illustrated with upward of thirty graven and mezzotinto plates ...* 1750. doi: 10.3931/e-rara-28672.

X. Yang, H. J. Mo, and F. C. van den Bosch. Constraining galaxy formation and cosmology with the conditional luminosity function of galaxies. *MNRAS*, 339:1057–1080, March 2003. doi: 10.1046/j.1365-8711.2003.06254.x.

S.-J. Yoon, S. K. Yi, and Y.-W. Lee. Explaining the Color Distributions of Globular Cluster Systems in Elliptical Galaxies. *Science*, 311:1129–1132, February 2006. doi: 10.1126/science.1122294.

J. Zavala, C. S. Frenk, R. Bower, J. Schaye, T. Theuns, R. A. Crain, J. W. Trayford, M. Schaller, and M. Furlong. The link between the assembly of the inner dark matter halo and the angular momentum evolution of galaxies in the EAGLE simulation. *MNRAS*, 460:4466–4482, August 2016. doi: 10.1093/mnras/stw1286.

I. B. Zeldovich, J. Einasto, and S. F. Shandarin. Giant voids in the universe. *Nature*, 300:407–413, December 1982. doi: 10.1038/300407a0.

Y. B. Zel'dovich. Special Issue: the Cosmological Constant and the Theory of Elementary Particles. *Soviet Physics Uspekhi*, 11:381–393, March 1968. doi: 10.1070/PU1968v011n03ABEH003927.

Y. B. Zel'dovich. Gravitational instability: An approximate theory for large density perturbations. *A&A*, 5:84–89, March 1970.

S. E. Zepf and K. M. Ashman. Globular Cluster Systems Formed in Galaxy Mergers. *MNRAS*, 264:611, October 1993. doi: 10.1093/mnras/264.3.611.

F. Zwicky. Die Rotverschiebung von extragalaktischen Nebeln. *Helvetica Physica Acta*, 6:110–127, 1933.

F. Zwicky. On the Masses of Nebulae and of Clusters of Nebulae. *ApJ*, 86:217, October 1937. doi: 10.1086/143864.